VOLUME 9 NUMBER 1 2018 ISSN 2218-7987
eISSN 2409-5508

International Journal of Mathematics and Physics

Al-Farabi Kazakh National University

The International Journal of Mathematics and Physics is a peer-reviewed international journal covering all branches of mathematics and physics. The Journal welcomes papers on modern problems of mathematics and physics, in particular, Applied Mathematics, Algebra, Mathematical Analysis, Differential Equations, Mechanics, Informatics, Mathematical Modeling, Applied Physics, Radio Physics, Thermophysics, Nuclear Physics, Nanotechnology, and etc.

International Journal of Mathematics and Physics is published twice a year by al-Farabi Kazakh National University, 71 al-Farabi ave., 050040, Almaty, Kazakhstan
website: http://ijmph.kaznu.kz/

Any inquiry for subscriptions should be send to:
Prof. Tlekkabul Ramazanov, al-Farabi Kazakh National University
71 al-Farabi ave., 050040, Almaty, Kazakhstan
e-mail: Tlekkabul.Ramazanov@kaznu.kz

 Printed in Kazakhstan

EDITORIAL

The most significant scientific achievements are attained through joint efforts of different sciences, mathematics and physics are among them. Therefore publication of the Journal, which shows results of current investigations in the field of mathematics and physics, will allow wider exhibition of scientific problems, tasks and discoveries.

One of the basic goals of the Journal is to promote extensive exchange of information between scientists from all over the world. We propose publishing service for original papers and materials of Mathematical and Physical Conferences (by selection) held in different countries and in the Republic of Kazakhstan.

Creation of the special International Journal of Mathematics and Physics is of great importance because a vast amount of scientists are willing to publish their articles and it will help to widen the geography of future dissemination. We will also be glad to publish papers of scientists from all the continents.

The Journal will publish experimental and theoretical investigations on Mathematics, Physical Technology and Physics. Among the subject emphasized are modern problems of Applied Mathematics, Algebra, Mathematical Analysis, Differential Equations, Mechanics, Informatics, Mathematical Modeling, Astronomy, Space Research, Theoretical Physics, Plasma Physics, Chemical Physics, Radio Physics, Thermophysics, Nuclear Physics, Nanotechnology, and etc.

The Journal is issued on the base of al-Farabi Kazakh National University. Leading scientists from different countries of the world agreed to join the Editorial Board of the Journal.

The Journal is published twice a year by al-Farabi Kazakh National University. We hope to receive papers from many laboratories which are interested in applications of the scientific principles of mathematics and physics and are carrying out researches on such subjects as production of new materials or technological problems.

IRSTI 28.17.23; 29.15.35

[1]F.F. Komarov, [2]A.I. Kupchishin, [3*]T.A.Shmygaleva,
[3]S.T. Janybekova, [4]A.A. Kuatbayeva, [3]A.B. Bekaydar

[1]Belarusian State University, Minsk, Belarus
[2]Abay Kazakh national pedagogical University, Almaty, Kazakhstan
[3]al-Farabi Kazakh National University, Almaty, Kazakhstan
[4]Sh. Ualikhanov Kokshetau State University, Kokshetau, Kazakhstan
[*]e-mail: shmyg1953@mail.ru

Computer modeling of processes of radiation defection formation in aluminum irradiated by ions

Abstract. The article considers the process of interaction of ions with aluminum and the formation of the radiation defects. The selection of an approximate expression for the interaction cross section is found and the approximation coefficients are found. Algorithms of calculation of a cascade probability function, range of the primary beaten-out atoms, concentration of radiation defects are given. Calculations of cascade probability functions depending on number of interactions and a depth of penetration of particles, ranges of the primary beaten-out atoms (PKA), concentration of radiation defects are made. Regularities of behavior and finding of area of result when calculating cascade probability functions depending on number of interactions and a depth of penetration of particles , concentration of radiation defects for the aluminum irradiated with ions are received. It is necessary to consider various factors: types of flying particles (charged and uncharged, light and Heavy), a real "physical" picture; i.e. processes occurring at interaction of particles with a substance.
Key words: ion, aluminium, approximation, algorithm, calculation, cascade-probabilistic function, the concentration of radiation defects.

Introduction

Modern development of science and technology requires the creation of fundamentally new materials that meet the requirements of various fields of energy. These materials should possess qualitatively new physical and chemical properties that assumes a detail study of structure of materials under the influence of the ionizing radiation and obtaining the defect information in structure of materials. A consequence of the action of ionizing radiation is a sharp change in their properties. Predicting the behavior of materials under harsh operating conditions requires the creation of quantitative models explaining radiation defect formation [1-8].

It is necessary to consider various factors: types of flying particles (charged and uncharged, light and Heavy), a real "physical" picture; i.e. processes occurring at interaction of particles with a substance. Aluminium is taken in the work. Aluminium and its alloys are increasingly used in shipbuilding Aluminum alloys are used for manufacturing ship hulls, deck superstructures, communication and various types of ship equipment. The main characteristics of aluminum and its alloys, revealing the expediency of their application in railway transport, high specific strength, small force of inertia, corrosion resistance. The introduction of aluminum alloys in the manufacture of welded tanks increases their durability in the transportation of a number of products of the chemical and petrochemical industry. One of the main requirements for materials used in road transport is low weight and relatively high strength. The corrosion resistance and good decorative surface of the material are also taken into consideration. The high specific strength of aluminum alloys increases the carrying capacity and reduces the operating costs of mobile transport. High corrosion resistance of the material extends

service life, expands the range of transported goods, including liquids and gases with high aggressive concentration.

The work is performed within the framework of a cascade-probabilistic method, the essence of which is to obtain and further use of cascade-probability functions (CPF) having the sense of the probability of reaching a particle of a certain depth h after the n-th number of collisions [9-11].

Main results

The cascade probability function for ions has the following form [11]:

$$\psi_n(h',h,E_0)=\frac{1}{n!\lambda_0^{\,n}}\left(\frac{E_0-kh'}{E_0-kh}\right)^{-l}\exp\left(\frac{h-h'}{\lambda_0}\right)*\left[\frac{\ln\left(\frac{E_0-kh'}{E_0-kh}\right)}{ak}-(h-h')\right]^n. \quad (1)$$

where h',h – depth of generation and registration of the particle, respectively, n – number of interactions, E_0- the initial energy of the primary particle, σ_0, a, E_0, k – approximation coefficients, $\lambda_0=1/\sigma_0$, $l=1/(\lambda_0 ak)$. Calculation of CPF is performed according to the formula:

$$\psi_n(h',h,E_0)=\exp\left[-\ln(n!)-n*\ln(\lambda_0)-\frac{1}{\lambda_0 ak}\ln\left(\frac{E_0-kh'}{E_0-kh}\right)+\frac{h-h'}{\lambda_0}+\right.$$
$$\left.+n*\ln\left(\frac{\ln\left(\frac{E_0-kh'}{E_0-kh}\right)}{ak}-(h-h')\right)\right], \quad (2)$$

In order to calculate the KPF by formula (2), it is necessary to find coefficients of approximation σ_0, a, E_0, k included in this expression. For this purpose, the interaction cross section is calculated by the Rutherford formula [12] there are depths of penetration from the tables of parameters of spatial distribution of ion-implanted impurities of Kumakhov-Komarov [13], the calculated section values are approximated with the following expression:

$$\sigma(h)=\sigma_0\left(\frac{1}{a(E_0-kh)}-1\right) \quad (3)$$

Then the approximation coefficients for the various ions in the aluminium have been found. Table 1 shows the approximation parameters for indium in aluminium. The results of the approximation selection are shown in figure 1.

Table 1 – Approximation values for indium in aluminum

E_0	$\sigma_0\times10^9$	α	$E_0^{'}$	K	η
1000	165.94806	2.07165	0.00184	0.13615	0.99285
800	176.93226	0.96197	0.00427	0.20159	0.99359
500	226.59381	0.75709	0.00928	1.2488	0.99282
200	290.18127	0.2588	0.03555	60.56595	0.99698
100	408.7585	0.1165	0.10402	440.66742	0.99852

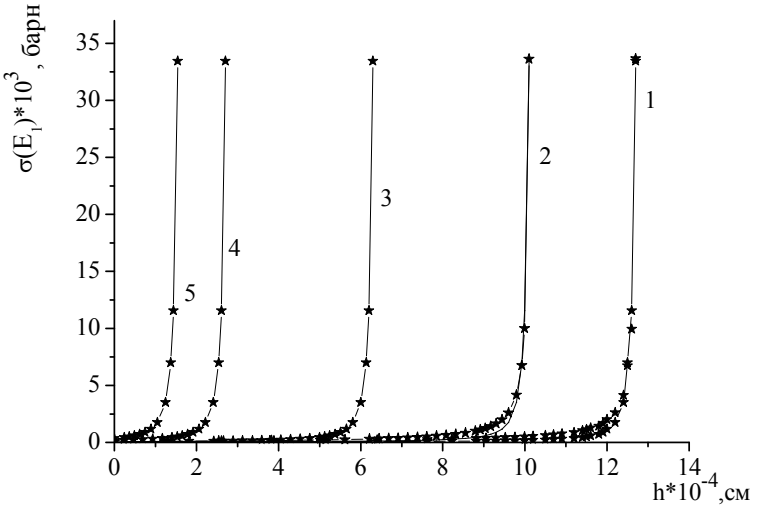

Figure 1 – Approximation of the modified section of the cascade-probability function for indium in aluminum
E_0= 1000(1), 800(2), 500(3), 200(4), 100(5) keV.
Points – calculated data of the dependence of the cross section on depth, solid line – approximation

Further calculations of the CPF have been performed as a function of the number of interactions (Table 2) and the penetration depth of the particles (Table 3).

The regularities in the behavior of the result area and the step for calculation for the CPF, calculated as a function of the number of interactions during irradiation of aluminum by ions, are revealed.

1. At a small atomic weight of the incident particle and small depths, the maximum value of the CVF is reached approximately at h/λ. With increasing depth observation area of the result begins to shift in the area of small depths of the respective h/λ. and narrow.

2. When the initial energy decreases (the particle and the target are the same) at the same depth the area of the result is also narrowed and shifted to the area of small depths.

3. As the atomic weight of the incident particle increases, the range of the result shifts to a region of shallow depths with respect to h/λ and narrows.

4. At a large atomic weight of the incident particle, the maximum value of the CPF shifts to a region of shallow depths relative to h/λ already at shallow depths, and at large depths the result is in a narrow region (less than 1%, silver, gold).

5. The narrowest area of the result is obtained with a large atomic weight of the incident particle and a small target at the end of the run and reaches hundredths of a percent. At the same time the account is growing strongly.

Since h/λ can be very large (tens of millions), then the values of the CPF, calculated in steps of 1, will not practically differ from each other and the counting time will be very long (more than two hours). The step takes some value N_n, that is added to the current n and KVF is calculated at n, $n+N_n$, $n+2N_n$ ... Thus for calculating the CPF, it is necessary to find not only the area for determining the result, and also to choose a step. When choosing the step, the following regularities take place.

1. For a small atomic weight of the incident particle and small depths, the step is small (about 10-20), with increasing depth of observation it begins to increase.

2. With increasing atomic weight of the incident particle, the step accordingly increases, reaching several hundred and even thousands.

3. When the atomic weight of the flying particle increases, the step increases accordingly, reaching several hundred and even thousands.

4. The pitch greatly increases with a large atomic weight of the incident particle and a small target.

Table 2 – Dependence of the percentage of displacement of the left and right boundaries of the result area on the number of interactions for nitrogen in aluminum: a) E_0=1000 keV; b) E_0=800 keV; c) E_0=500 keV; d) E_0=200 keV; e) E_0=100 keV

$h*10^4$, cm	B_1,%	B_2,%	N_n	B_3,%
10	38	8	40	46
15	39	-8	35	3,1
20	43,5	-22	40	21,5
25	49	-33	45	16
30	55	-43	57	12
35	62,4	-53,85	65	8,55
40	71,66	-66,6	75	5,06
45	84,88	-82,86	95	2,06

a)

$h*10^4$, cm	B_1,%	B_2,%	N_n	B_3,%
10	37	1	35	38
15	40,5	-15	35	25,2
20	46,5	-28	47	18,5
25	53,5	-40,7	63	12,8
30	62	-53,85	75	8,15
35	73,54	-68,9	95	4,64

b)

$h*10^4$, cm	B_1,%	B_2,%	N_n	B_3,%
1	58	68	13	126
4	35,3	20	25	55,3
7	34	2	30	36
10	37	-11	38	26
13	41,5	-22,23	48	19,27
16	47,5	-33	54	14,5
19	54,3	-44,4	67	9,9
22	62	-55,75	75	6,25
25	73,3	-69	97	44,3

c)

$h*10^4$, cm	B_1,%	B_2,%	N_n	B_3,%
1	38,6	38	15	76,6
3	30,2	6	24	36,2
5	34	-10	37	24
7	40,5	-24	45	16,5
9	5	-39,8	50	34,8
11	62,23	-65,5	75	3,27
12	69,87	-65,3	85	4,57

d)

$h*10^4$, cm	B_1,%	B_2,%	N_n	B_3,%
1	30,5	21,5	25	52
2	29,4	0,6	35	30
3	33,8	-12	43	21,8
4	40,6	-25	50	15,6
5	49,2	-39	60	10,2
6	60,71	-54	75	6,71

e)

Table 3 – Dependence of percentage of displacement of the left and right boundaries of the result area from the penetration depth for silver in aluminum: a) E_0=1000 keV; b) E_0=800 keV; c) E_0=500 keV; d) E_0=200 keV; e) E_0=100 keV

$h*10^4$, cm	h/λ	C_1,%	C_2,%	N_h	C_3,%
1	13164	-1,37	12	110	10,63
3	52312	-15,4	20,2	270	4,8
5	119152	-25,3	28,1	480	2,8
7	241088	-31,192	32,56	993	1,368
9	499490	-30,415	30,9	2800	0,485

a)

$h*10^4$, cm	h/λ	C_1,%	C_2,%	N_h	C_3,%
1	24110	-1,752	9,5	150	7,748
2	54588	-8,7	14	240	5,3
3	94062	-15,046	18,8	360	3,754
4	146836	-20,91	23,5	480	2,59
5	220484	-25,942	27,8	780	1,858
6	329673	-29,293	30,45	1280	1,157
7	507016	-29,507	30,1	2480	0,593
8	842620	-24,575	24,745	8000	0,17

b)

$h*10^4$, cm	h/λ	C_1,%	C_2,%	N_h	C_3,%
1	42461	-6,52	12,2	210	5,68
2	106987	-17,073	20,42	405	3,347
3	213796	-25,93	27,88	755	1,95
4	418665	-30,226	31.071	1800	0,845
5	952474	-23,23	23,342	11500	0,112

c)

$h*10^5$, cm	h/λ	C_1,%	C_2,%	N_h	C_3,%
1	9200	3,5	9,6	85	13,1
4	43505	-7,57	13,4	210	5,83
7	91527	-15,84	19,52	350	3,68
10	160878	-22,93	25,3	520	2,37
13	266084	-28,37	30	860	1,63
16	438730	-30,934	31,82	1650	0,886
19	762930	-28,45	28,78	4600	0,33

d)

$h*10^5$, cm	h/λ	C_1,%	C_2,%	N_h	C_3,%
1	20130	-0,6	9,5	133	8,9
3	74350	-11,82	16	305	4,24
5	156710	-20,79	23,5	525	2,71
7	288940	-27,77	29,5	900	1,73
9	522905	-31,107	31,86	1900	0,753
11	1020546	-27,316	27,54	6600	0,224

e)

Some regularities appearing when finding the real domain of determination for the CPF, calculated depending on the penetration depth, are noted.

1. Calculations show that for a small atomic weight of the incident particle and small depths, the region of the result of the CPF as a function of h is near h, which corresponds to h/λ. When the depth of observation is increased, the result area shifts to a region of greater depths and narrows.

2. When the initial energy of the particle decreases (the incident particle is the same) at the same depth of observation, the resultant region shifts to a region of large depths and narrows.

3. When the depth of observation is increased for any incident particle, the result area shifts to the right.

4. Depending on the atomic number of the incident particle at the same value of the depth h, the result area shifts to a region of large depths.

5. When a large value of the atomic number of the projectile is the area of the result is shifted to larger depths relative to h corresponding to h/λ already at shallow depths.

To calculate CPF in the found area, you must specify a step. In this case, a certain N_h value was taken as a step, which was added to the current h and the CPF was calculated at h, $h+N_h$, $h+2N_h$, . . . Let's note some regularities of behavior of a step.

1. For a small atomic weight of the flying particle the step is small, with increase in depth of observation it increases, and on the end of a run very strongly.

2. With decrease of tentative energy of a particle with the same depth of observation (the flying particle same) the step also increases.

3. With increasing atomic weight of the incident particle for one and the same depth of observation, the step increases first gradually, then very sharply.

Next, calculations of the concentration of radiation defects for various incident particles in aluminum have been made using the following formula:

$$C_k(E_0,h) = \int_{E_c}^{E_{2\max}} W(E_0,E_2,h)dE_2 , \qquad (4)$$

E_2 – primary knocked-out energy, E_{2max} the maximum kinetic energy that the atom will receive, E_c – threshold energy, $W(E_0,E_2,h)$ – the spectrum of primary knocked-out atoms. The results of the calculations are presented in Tables 4-6.

Table 4 – Limits of the region of determination of the concentration of radiation defects for germanium in aluminum at E_c=50 keV, E_0= 1000 keV

h*10 $^{-4}$, cm	$C_к$, cm	E_0, keV	n_0	n_1	τ
0,1	31452,9	1000	342	663	5″75
2	34640,8	900	10319	11772	1′26″
4	38790,1	800	22509	24628	4′10″
6	44060,6	700	36526	39213	7′ 25″
8,1	51426,5	600	53795	57102	12′57
10,1	61077,3	500	73611	77333	19′32″
12	74085,3	400	96941	101215	29′03″
13	83450	350	111802	116424	36′55″
14	95400,5	300	129231	134213	44′33
14,3	99134,5	280	135104	140152	47′20
14,7	105238	260	143505	148774	53′42″
15,1	112049	240	152665	158192	59′
15,5	119653	220	162734	168361	$1^0$03′
15,8	124508	200	171000	176816	$1^0$09′
16,2	133078	180	183184	189101	$1^0$14′
16,6	142065	160	197029	203203	$1^0$23′
16,9	144496	140	208809	215170	$1^0$30′
17,3	148840	120	226991	233671	$1^0$44′
17,6	135244	100	243135	250085	$1^0$55′
18	99265,8	80	269617	277085	$2^0$17′
18,1	48551,7	70	277471	284876	$2^0$22′
18,3	0	60	295266	302961	$2^0$33′

Table 5 – Limits of the region of determination of the concentration of radiation defects for germanium in aluminum at E_c=50 keV, E_0= 500 keV

h*10 ^{4}, sm	$C_к$, cm^{-1}	E_0, keV	n_0	n_1
0,1	55205,65	500	732	1177
2	68422,14	400	21344	23380
3	77960,77	350	34982	37597
3,9	88414,43	300	49461	52552
4,3	94041,72	280	56753	60141
4,7	100325,61	260	64696	68332
5	104745,65	240	71149	74955
5,4	112163,36	220	80531	84510
5,8	120392,95	200	90980	95309
6,1	125325,64	180	99669	105065
6,5	133914,22	160	112668	117351
6,9	142074,07	140	127742	132743
7,2	140336,23	120	140849	146091
7,6	134940,54	100	161665	167314
7,9	92994,21	80	180855	186858
8,1	49191,1	70	196123	202371
8,2	0	60	204751	211247

Table 6 – Limits of the region of determination of the concentration of radiation defects for germanium in aluminum at E_c=50 keV, E_0= 200 keV

h*10 ^{4}, cm	$C_к$, cm	E_0, keV	n_0	n_1
0,1	123843,73	200	2374	3113
0,4	130916,49	180	11019	12529
0,7	137135,12	160	20901	22972
1,1	147583,01	140	36251	38951
1,4	147032,15	120	49806	53019
1,8	142423,51	100	71572	75422
2,1	98253,23	80	91756	96218
2,3	51800,91	70	107808	112501
2,5	0	60	126727	131688

Finding the region of the result of the concentration of radiation defects during ion irradiation made it possible to reveal the following regularities:

1. During the reduction of the initial energy of the primary particle, the range of the result area shifts to a region of greater depths, the values of the concentration of radiation defects increase.

2. Counting time and reaches several hours increases greatly with a large atomic weight of the flying particle and a small target.

3. Depending on the penetration depth, the initial and final values of the number of interactions increase, the interval of the result area ((n_0 n_1) also increases and shifts to the greater depths.

4. The interval of the result area is significantly shifted to the right and increases, the value of the concentration at the maximum point and the concentration values themselves greatly increase with the atomic number of the incident particle.

Conclusion

Thus, the paper presents a mathematical model of a cascade-probability function with allowance for energy losses for ions, an algorithm for calculating CPF, an approximation of the interaction cross section, and approximation coefficients for indium in aluminum. Calculations of CPF for various incident particles in aluminum are performed, depending on the number of interactions and the penetration depth of the particles. The regularities in the behavior of the area of the CPF result and the step for calculation are revealed. A model for

calculating the concentration of radiation defects is presented, calculations are performed, regularities in the behavior of the result area are obtained depending on various factors.

References

1. Agranovich B.M., Kirsanov B.B. “Problemy modelirovaniya radiatsionnogo povrezhdeniya v kristallakh” (“Problems of Modeling Radiation Damage in Crystals”). *Successes of physical sciences* 1 (1976): 2-51. (in Russian).

2. “Modelirovanie na EHVM defektov v kristallah.” (“Computer simulation of defects in crystals”). *In Materials of the All-Union Seminars*, ed. by Orlov A.N., Trushina Yu.V. Leningrad: FTI named after AI. Ioffe AS of the USSR Publ., 1979. – 205 p. (in Russian).

3. Akkerman A.F., Nikitushev Yu.M., Botvin V.A. *Resheniye metodom Monte-Karlo zadach perenosa bystrykh elektronov v veshchestve.* (*Solution by the Monte Carlo method of problems of transfer of fast electrons in matter*). Alma-Ata: Nauka Publ., 1972. – 162 p. (in Russian).

4. Caro A. “Molecular dynamic approach to heavy ion impast.” *Radiation Effects and Defects in Solids* 126 (1993): 15-20.

5. Zou Y., Waya Y.A., Kambara T., Kanai Y., Oivra M. Ardo K., Hitashi A., Kravis S. “Foil target element and incident energy dependence of multiple inner shell vacancy production of projectile ar ions.” *Radiation Effects and Defects in Solids* 126 (1993): 87-90.

6. Audouard A., Balanzar E., Jousset J.C., Lesueur D., Thome L. “Anisotropy of the atomic movements induced in amorphous metallic alloys by swift heavy ion irradiation.” *Radiation Effects and Defects in Solids* 126 (1993): 93-96.

7. Fink D., Chadderton L.T., Cruz S.A., Fahrner W.R. Hnatowir V., E.H. te Kaat, Melnikov A.A., Varichenko V.S., Zaitsev A.M. “Ion Tracks in condensed carbonaceus matter.” *Radiation Effects and Defects in Solids* 126 (1993): 247-250.

8. Bjeoumikhov A., Buzanich G., Langhoff N., Soltau H., (...), Wedell R. “The SLcam: A full-field energy dispersive X-ray camera.” *Journal of Instrumentation* 7, no. 5 (2012): 248-252.

9. Bock M., Skibina J., Fischer D., (...), Beloglazov V., Steinmeyer G. “Nanostructured fibers for sub-10 fs optical pulse delivery.” *Laser and Photonics Reviews* 7, no. 3 (2013): 566-570.

10. Dubovichenko S., Burtebayev N., Dzhazairov-Kakhramanov A., (...), Kliczewski S., Sadykov T. “New measurements and phase shift analysis of p16O elastic scattering at astrophysical energies.” *Chinese Physics C* 41, no. 1 (2017): 485-495.

11. Conopleva R.F., Litvinov V.L., Uhin N.A. *Osobennosti radiatsionnogo povrezhdeniya poluprovodnikov vysokoenergeticheskimi chastitsami. (Features of radiation damage to semiconductors by high-energy particles)*. Moscow: Atomizdat Publ., 1971. – 175 p. (in Russian).

12. Boss E.G., Kupchishin A.I. *Solution of physical tasks by a cascade and probabilistic method*. Alma-Ata: Science, 1988. – 112 p.

13. Boss E.G., Kupchishin A.I. *Solution of physical tasks by a cascade and probabilistic method*. Alma-Ata: Science 1, 1998. – 144 p.

14. Boos E.G., Kupchishin A.A., Kupchishin A.I., Shmygalev E.V., Shmygaleva T.A. *Cascade and probabilistic method, solution of radiation and physical tasks, Boltzmann's equations. Communication with Markov's chains.* – Monograph. Almaty: KazNPU after Abay, Scientific Research Institute for New Chemical Technologies and Materials under al-Farabi KazNU. 2015. – 388 p.

15. Merkle K.L. Radiation-induced point defects clusters in copper and gold.” *Physica status solidi* 18, no. 1 (1966): 173-188.

16. Burenkov A.F., Komarov F.F., Kumakhov M.A., Temkin M.M. *Tables of parameters of the spatial distribution of ion implanted impurities*. Minsk: BSU named after Lenin Publ., 1980. – 352 p.

17. Czarnacka, K., Komarov, F.F., Romanov, I.A., Zukowski, P., Parkhomenko, I.N. “AC measurements and dielectric properties of nitrogen-rich silicon nitride thin films.” *Proceedings of the 2017 IEEE 7th International Conference on Nanomaterials: Applications and Properties*, *NAP 2017*, no. 5 (2017): 657-669.

18. Komarov, F.F., Milchanin, O.V., Parfimovich, I.D., Tkachev, A.G., Bychanok, D.S. “Absorption and Reflectance Spectra of Microwave Radiation by an Epoxy Resin Composite with Multi-Walled Carbon Nanotubes.” *Journal of Applied Spectroscopy* 84, no. 4 (2017): 570-577.

19. Komarov F.F. “Nano- and microstructuring of solids by swift heavy ions.” *Physics-Uspekhi* 187, no. 5 (2017): 465-504

IRSTI 30.17.51

[1*]Y. Yerdesh, [2]Y. Belyayev, [3]D. Baiseitov, [4]M. Murugesan

[1]al-Farabi Kazakh National University, Almaty, Kazakhstan
[2]Satbayev University, al-Farabi Kazakh National University, Almaty, Kazakhstan
[3]al-Farabi Kazakh National University, Almaty, Kazakhstan
[4]Department of Mechanical Engineering, Hindusthan College of Engineering and Technology Tamil Nadu, India
[*]e-mail: yelnaryerdesh@gmail.com

Modeling two-phase flow in pipe of the solar collector

Abstract. Solar collector is often used as evaporator in heat pump system. In the solar collector pipe, liquid is transferred from liquid phase to gas phase. The effective operation of heat pump depends on boiling point of the refrigerant and the process of phase change. Therefore, simulation of two-phase flow in the pipe is considered.

In two-phase flow, velocity field and pressure of the liquid phase are characterized by incompressible Navier-Stokes equation and compressible Navier-Stokes equation in the vapor phase. Dynamics of two-phase flow is described by Cahn-Hilliard equation to take into account the phase transition. Two-phase flow is solved using finite elements in COMSOL Multiphysics program using phase-field model based on Cahn-Hilliard phase variable equation. The higher the liquid density, the higher the Archimedes force on the vapor, which is the prerequisite for rapid and intense rise from the vapor bubbles. This also explains why the value of oscillation is bigger.

This article discusses the two-phase flow of solar collector coolant. Therefore, it is desirable to select the density value so that the liquid is rapidly steamed and fast, i.e., it has low oscillation. Based on these results, we can describe the effect of the liquid phase (density) on phase transitions.

Key words: two-phase flow, phase field, phase variable, refrigerant, heat pump.

Introduction

Heat pump is a device that converts low temperature heat to the consumer in a highly potentially heat state. The functioning of the heat pump is based on the phenomenon of fluid-gas exchange. In this process, liquid evaporation absorbs heat and, conversely, condensed heat is released. At present the solar collector is often used as the evaporator in the heat pump system.

From effect of the solar energy, in the pipe of the solar collector refrigerant switches from the liquid phase to the gas phase. The effective operation of the heat pump depends on the refrigerant boiling point and the phase transformation process. Therefore, let's consider fluid in the pipe, the two-phase flow, when heat flow influences to the pipe from outside.

The two phase phase is classified according to the distribution of the vapor phase. The same classification that occurs in the pipe is referred to as flow regimes (Figure 1). Depending on the flow regimes, the fluid properties (hydrodynamic conditions) around the heated pipe wall change. For example, during friction loss of pressure or change of boiling process and change of heat exchange [1].

 Printed in Kazakhstan

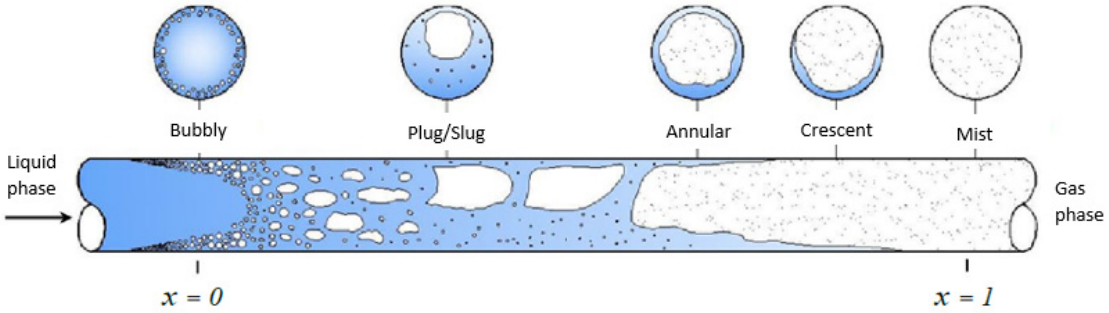

Figure 1 – Scheme of two-phase flow modes in horizontal pipe

One of the most important goals of two-phase flow research is to determine the characteristics of heat exchange and pressure loss. In general, calculation of two-phase flow with loss of heat is a difficult CFD (thermohydrodynamic) calculation. On the one hand, the heat exchange leads to phase transitions, and consequently leads to the phase distribution and the flow regime. On the other hand, changes in the fluid dynamics characteristics, such as the pressure loss on the flow path, affect the heat exchange. At the same time, a single-component two-phase flow in the vertical or horizontal pipe will never be completely adjusted [2].

Boiling regimes (nucleate, transition, film) change depending on the amount of excess temperature and heat which transfer from the solid surface (Fig. 2). Here, the excess temperature is the difference between the solid surface temperature and the liquid's saturation temperature.

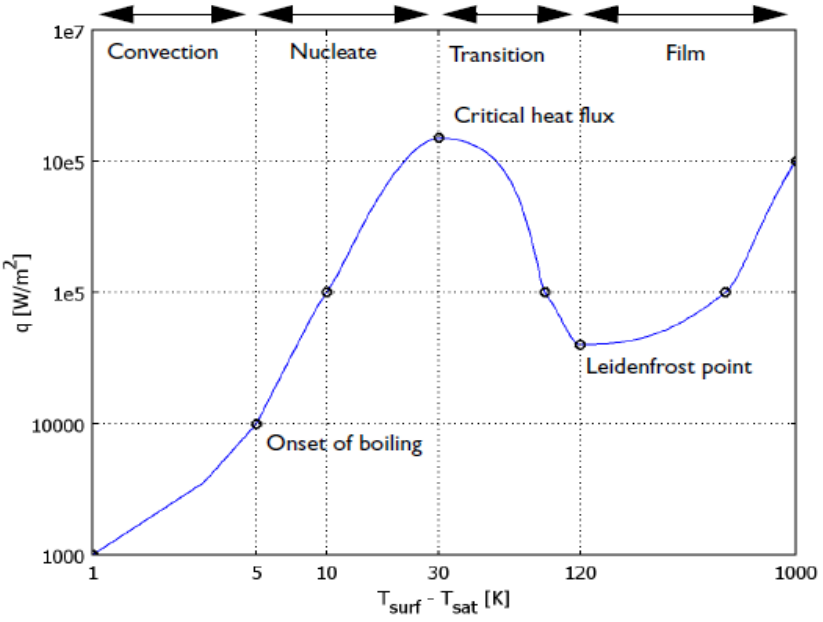

Figure 2 – Boiling point of water at atmospheric pressure (101325 Pa). Depending on the boiling point temperature and excess temperature

Theoretical part

2.1 Mathematical model

The physical phenomenon of the boiling fluid is determined by the interface dynamics. The boiling model uses the Navier-Stokes equation, the convection and the condensation equation. First, the boiling process is formulated by equations and boundary conditions. Then, to solve the problem, several approximations are made for characterize

interface, and solved by phase field equations [3]-[4].

In general, for the two-phase flow, the velocity field and pressure of the liquid phase are characterized by incompressible Navier-Stokes and continuity equation and the gas phase are characterized by compressible Navier-Stokes equation.

Since the liquid temperature is constant (saturation temperature) of all sizes, there is no need to solve the heat equation for liquid. The heat transfer equation is solved only for the gas phase.

It is difficult to set boundary conditions for the boiling process model.

The boundary condition for gas phase boundary:

$$\boldsymbol{n}\cdot\rho_V\boldsymbol{u_V}=\dot{m}\left(1-\frac{\rho_V}{\rho_L}\right)+(\boldsymbol{n}\cdot\rho_{\,V}\boldsymbol{u_L}), \quad (1)$$

here, $\dot{m}-$ evaporation rate (mass flow through the liquid-vapor boundary) (kg/m^2·c).

In (1) equation, when density of the liquid doesn't equal to the gas density, the first expression of the right side gives us flow velosity which directed perpendicularly to the border.

For fluid, effects 3 different forces on the boundary. Therefore, boundary condition for liquid is:

$$\boldsymbol{n}\cdot[-p_L\mathbf{I}+\mu_L(\nabla\boldsymbol{u_L}+(\nabla\boldsymbol{u_L})^T)]=\dot{m}(\boldsymbol{u_L}-\boldsymbol{u_V})+\sigma\kappa\boldsymbol{n}+$$
$$+\boldsymbol{n}\cdot\left[-p_V\mathbf{I}+\mu_V(\nabla\boldsymbol{u_V}+(\nabla\boldsymbol{u_V})^T)-\frac{2}{3}\mu_V(\nabla\cdot\boldsymbol{u}_{\mathbf{V}})\mathbf{I}\right]. \quad (2)$$

(2) is the balance of power that affects the interface. The second expression on the right describes the surface tension, and the last expression describes the total force of the pressure and viscous forces which influence from gas to liquid.

At the liquid-gas boundary (in energy equation), the temperature of the boiling point is taken as the temperature. Saturation temperature can be a function of pressure:

$$T=T_{\,sat}(p). \quad (3)$$

Thus, we can describe the mass flow in the phase boundary through the heat flow:

$$\dot{m}=-\left(\frac{M_w}{\Delta H_{Vl}}\right)\boldsymbol{n}\cdot\kappa_{\,V}\nabla T_V\,, \quad (4)$$

here:

M_w- molecular mass of the gas (kg/mole),

$\Delta H_{Vl}-$ evaporation enthalpy (J/mole),

$T_{sat}-$ saturation temperature of the liquid.

This approximation ignores the work of kinetic energy and viscous forces [3].

Navier-Stokes and continuty equation for the liquid phase, compressible Navier-Stokes and heat transfer equation for gas phase (1) - (3) can fully describe the boiling process with boundary conditions. Finally, these equations can be solved by the free Lagrange-Euler's equation in Comsol program. But in this case we can not see the topological changes [5]-[6]. By making several necessary assumptions, we can solve this problem in a fixed grid using Phase Field.

2.2 Phase Field model

When switching to a fixed grid you have to make some approximations.

The dynamics of the two-phase flow is characterized by the Cahn-Hilliard equation. As noting in [4], [7], in order to take into account phase transitions, the equation for the phase field variable is introduced:

$$\frac{\partial\varphi}{\partial t}+\boldsymbol{u}\cdot\nabla\varphi-\dot{m}\delta\left(\frac{V_{f,V}}{\rho_V}+\frac{V_{f,L}}{\rho_L}\right)=\nabla\cdot\frac{\gamma\lambda}{\varepsilon^2}\nabla\psi \quad (5)$$

here:

φ – dimensionless phase field variable (phase indecator), $|\varphi|\leq 1$,

$V_{f,V}-$ volume of the gas phase,

$V_{f,L}-$ volume of the liquid phase,

λ – mixing energy density (H) ,

ε – capillary width (in accordance with the thickness of the border) (m).

The parameters λ and ε have connection with the surface tension coefficient as follows:

$$\sigma=\frac{2\sqrt{2}}{3}\frac{\lambda}{\varepsilon}\,, \quad (6)$$

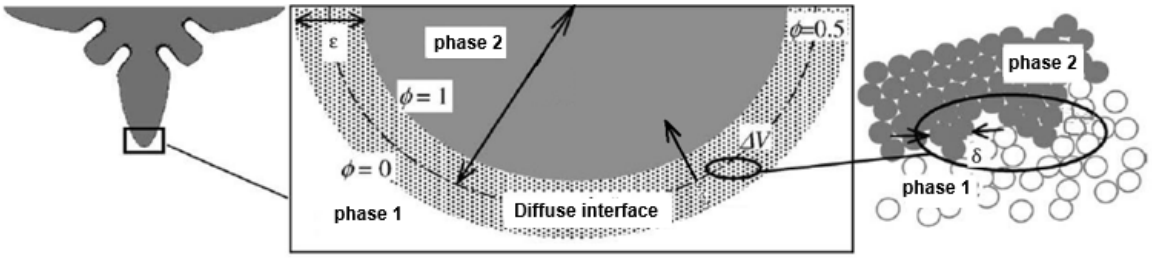

Figure 3 – Phase field model

γ – mobility, m^3·s/kg.

$\psi -$ auxiliary variable is determined by the equation:

$$\psi = -\nabla \cdot \varepsilon^2 \nabla\varphi + (\varphi^2 - 1)\varphi, \quad (7)$$

δ (1/m) – smoothness of the surface (curvature) between the two phases (Figure 3). This variable is defined in the phase field model as follows:

$$\delta = 6V_f(1 - V_f)\frac{|\nabla\varphi|}{2} \quad (8)$$

In the equation of motion the surface tension is taken into account along with volumetric forces (force of pressure, force of force and Archimedes force):

$$\rho\frac{\partial \boldsymbol{u}}{\partial t} + \rho(\boldsymbol{u}\cdot\nabla)\boldsymbol{u} = \\ = \nabla\cdot[-p\mathbf{I} + \mu(\nabla\boldsymbol{u} + (\nabla\boldsymbol{u})^T)] + \\ + \rho g + G\nabla\varphi \quad (9)$$

here, G – chemical potential (Pa):

$$G = \frac{\lambda}{\varepsilon^2} - \nabla\cdot\varepsilon^2\nabla\varphi + (\varphi^2 - 1)\varphi. \quad (10)$$

The density and viscosity of the medium are calculated as follows:

$$\rho = \rho_L + (\rho_V - \rho_L)\varphi, \quad (11a)$$

$$\mu = \mu_L + (\mu_V - \mu_L)\varphi. \quad (11b)$$

Indexes L, v is represent the corresponding properties of liquids and gases. $\rho_V -$ gas density is determined by the equation of perfect gas (Clapeyron - Mendeleyev).

The continuity equation, as the liquid phase changes to the gas phase, is as follows:

$$\nabla\cdot\boldsymbol{u} = \dot{m}\delta\left(\frac{1}{\rho_V} - \frac{1}{\rho_L}\right). \quad (12)$$

Now the question is to define an expression describing the rate of phase transformation. (4) can not be used because the threshold temperature gradient does not match the interface. In this case, the mass flow passing through the boundary surface is not estimated correctly. Instead, the following approximations are used to describe the mass flow:

$$\dot{m} = -\left(\frac{M_w}{\Delta H_{Vl}}\right)\boldsymbol{n}\cdot\kappa_V\nabla T_V \approx C\rho_L\frac{(T - T_{sat})}{T_{sat}} \quad (13)$$

here, C – constant value (m/s).

Mass flow includes to the energy equation:

$$\rho C_p\frac{\partial T}{\partial t} + \rho C_p(\boldsymbol{u}\cdot\nabla)T = \nabla\cdot\kappa\nabla T - \frac{\dot{m}\delta\Delta H_{Vl}}{M_w} \quad (14)$$

The connection of equations (12) and (13) give reacing the temperature of the interface to saturation temperature.

Coefficients of thermal conductivity and heat capacity are calculated as the volume function of the two phases:

$$\kappa = (\kappa_L - \kappa_V)V_{f,L} + \kappa_V, \quad (15a)$$

$$C_p = (C_{p,L} - C_{p,V})V_{f,L} + C_{p,V}. \quad (15b)$$

Modeling in COMSOL Multiphysics

It is convenient to use COMSOL Multiphysics software package to simulate the process. Figure 4 shows the geometry and initial conditions required for the process. The heat flow is transferred to the copper wall. The amount of heat flux was obtained in a single amount of heat from solar radiation (about 1000 W/m^2); Refrigerants of various density are considered as liquid (the main is R-407C).

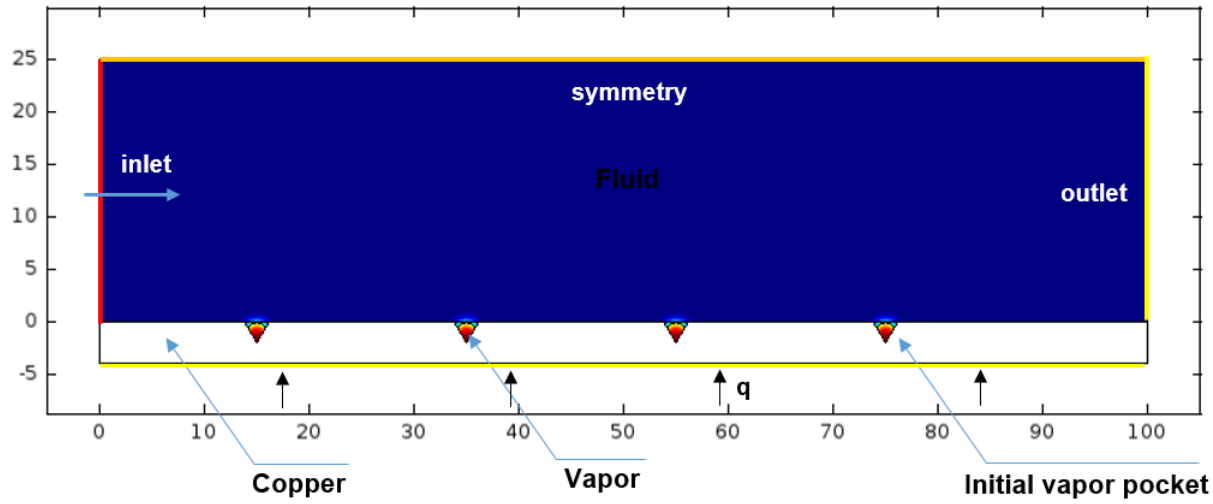

Figure 4 – Geometry and initial conditions

Saturation temperature (R407C) is 229.4 K, external medium pressure is 101325 Pa. Liquid viscosity $0{,}158 \cdot 10^{-3}$ Pa. The density of gas is given by the law of the ideal gas, vapor viscosity $1{,}25 \cdot 10^{-5}$ Pa. The surface tension ratio is 0.0069 N/m. The copper primary temperature is 238 K, the density is 8700 kg/m^3, the thermal capacity is 385 J/(kg), the thermal conductivity is 400 W/(m·K). In the model (Fig. 5), the heat transfer is accompanied by solid-copper phase (zone 3) with the liquid-vapor phase.

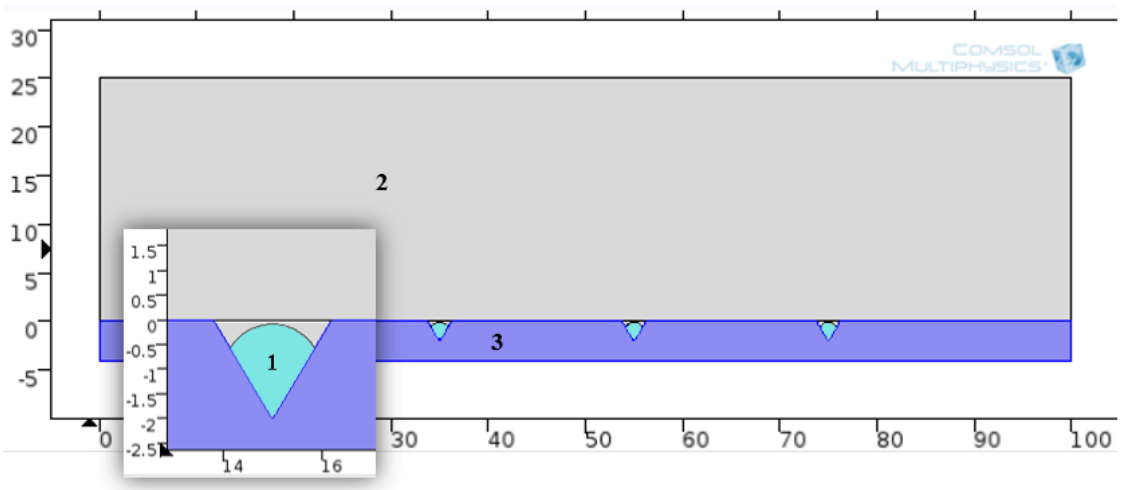

Figure 5 – Model of the problem

Zone 1 is a vapor phase, zone 2 is liquid, and zone 3 is solid. Phase Field (Laminar Two-Phase Flow, Phase Field) and Heat Transfer In Fluids in the zone 2 are selected. The zone 3 is a physics of Heat Transfer in Solids in solid state. (5) - (15), which describes two-phase flows, are covered by the physics of Laminar Two-Phase Flow, Phase Field and Heat Transfer in Fluids.

Results and Discussions

COMSOL Multiphysics program solved the numerical model of two-phase flow in the pipe. Figure 6 shows the two-phase flow model of pipe refrigerant (R-407C) on the basis of the problem's geometry. The given heat is supplied to the fluid and vapor through the copper-liquid or copper-

vapor boundary by heating the copper and passing through the heat material. Due to the temperature increase, two-phase flows are formed on the pipe. The liquid density is 1136 kg/m^3. Figure 6, e) and f) show that the pipe is a two-phase flow – annular regime (shown in Figure 1). The liquid phase is surrounded by a rim-like pipe wall, and most of the vapor phase is covered entirely by the pipe. And in a ring liquid layer, the vapor phase is found to be bubbles.

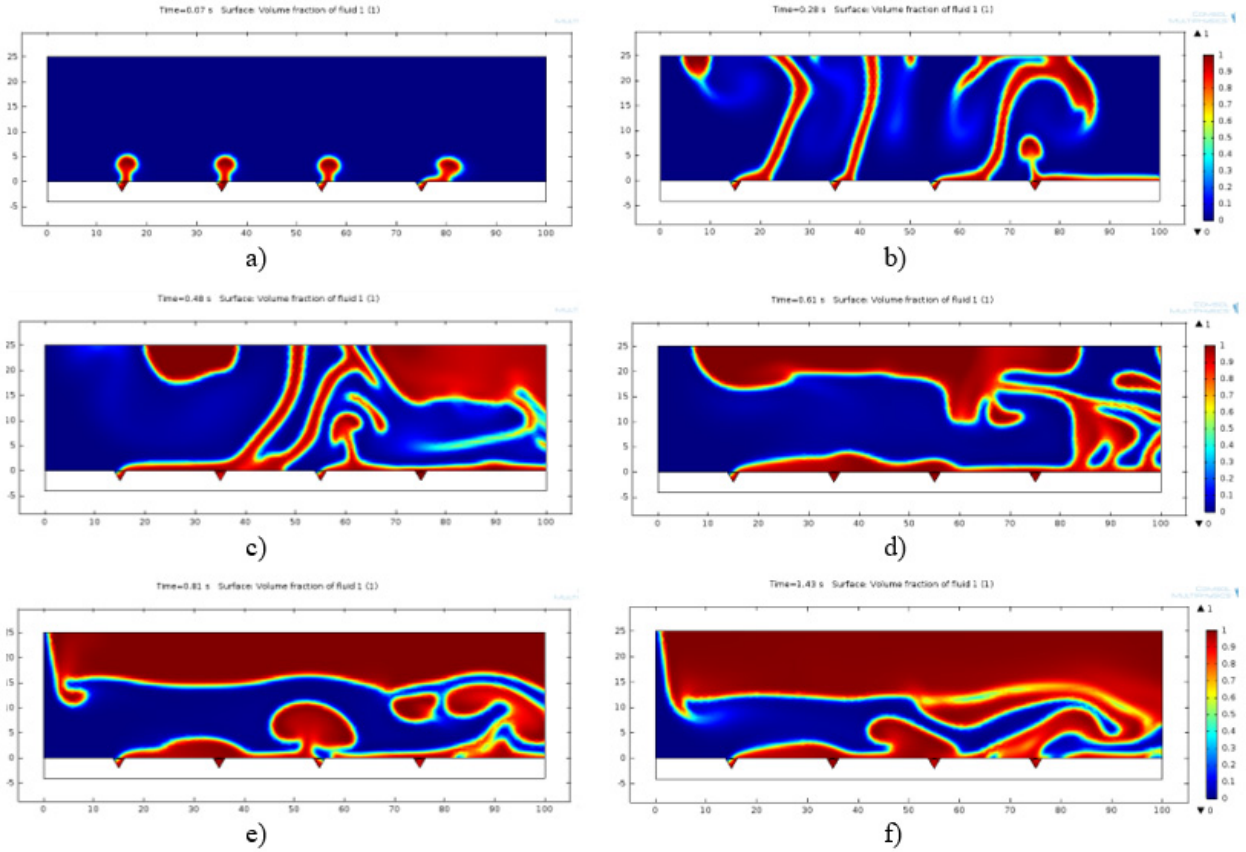

Figure 6 – Two-phase flow (refrigerant R-407C)

Figure 6 shows t = 0.07 (a); 0.28 (b); 0.48 (c); 0.61 (d); 0.81 (e); 1,43 (f) seconds are displayed. The following sequence of flows is repeated e) and f).

a) bubbles appear and begin to rise. The bubble growth is directly related to the saturated vapor pressure, which acts as a response to the atmospheric and fluid's hydrostatic pressure, due to increased temperature. And, in addition, the growth of the mass due to the evaporation of the liquid in the vapor bubbles. From the difference in liquid and vapor density, i.e., Archimedes force bubbles rise high. The mushroom shape of the bubble form is due to a decrease in the effect of the low density fluid and the increase in the amount of the surface tension coefficient between the liquid and the vapor bubbles [2].

b) because of the high heat transfer from the surface, the bubbles can be intensively formed, raised, coupled to one another, or controlled by columns.

c) and d), it is possible to notice that the boiling mode is under construction. And so much of the vapor phase began to flow into the center of the pipe.

In the case of e) and f), the annular mode of two-phase flow is formed.

The following steps have been taken to show cooling of the working fluid. Because of the two-phase time-dependent, unstable process, the mean space and the time value of the phase space variation (taking into account that the phase variables are fluid, where φ = 0 is a fluid, φ = 1). First, the vertical axis of the pipe outlet has not been

reached at least 1 mm (Figure 7). This ensures that the impact of the boundary condition is minimal. By this straight line, the φ - phase variable is derived from the averaged mean. Second, a graph between the average value and the time taken at each time space is constructed.

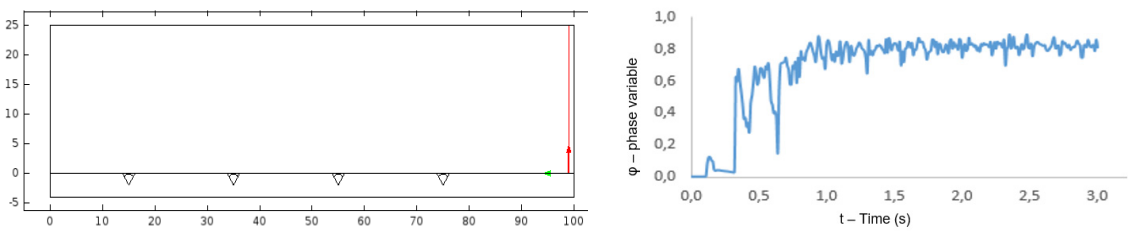

a) b)

Figure 7 – Space averaging
a) space averaging line; b) time dependence of φ – to the refrigerant R-407C.

As we can see from the Figure 7.b φ-t, where ρ = 1136 kg/m^3 (refrigerant R-407C), the value of φ-phase is relative to t = 1 second. This means that the circular flow mode has already been formed (Fig. 6, e), f)). Taking this into account, the third is averaged over time since the relative stability of the phase variable.

When the density ρ = 1136 kg/m^3, the mean of phase variables was φ = 0.812. Oscillation (difference between maximal and minimum deviations) is 0.24.

Fourth, the three steps mentioned above have been repeated without changing their refrigerant density (only by density change).

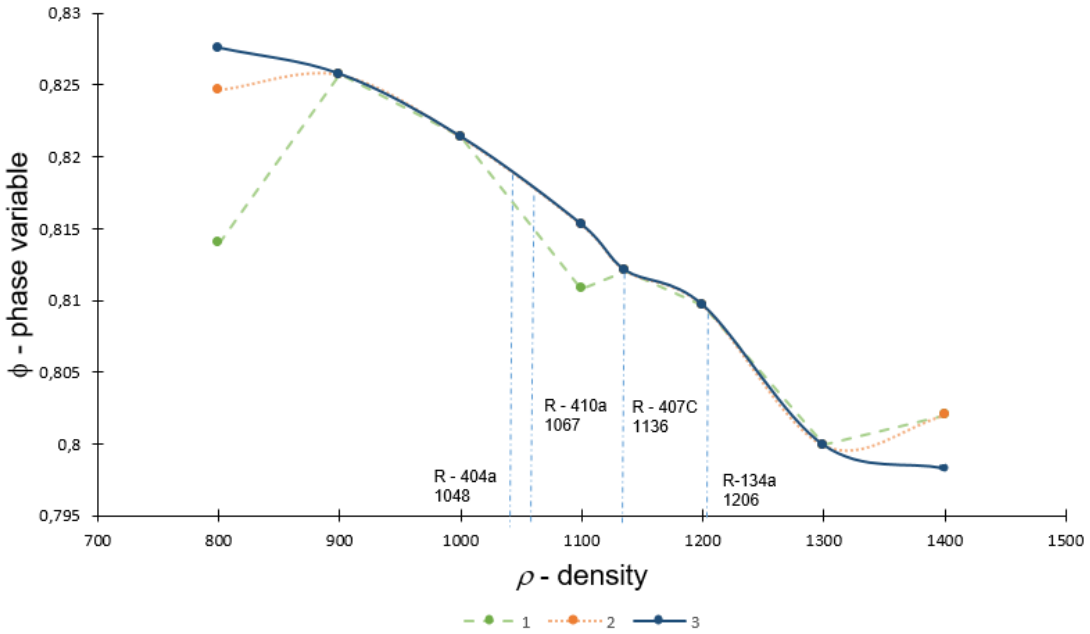

Figure 8 – Dependence of the φ – variable on density

The relationship between the given density and the mean value of the corresponding phase variables is plotted (Fig. 8).

The results show that at low density levels, the fluid gas phase is higher, the phase oscillation is 0.11-0.2. But the gas phase is slowly moving. At high density values, the fluid is rapidly converted to gas, but the mean value of the phase variable is relatively low and oscillation is about 0.24 to 0.27.

The higher the liquid density, the higher the Archimedes force on the vapor, which is the prerequisite for rapid and intense rise from the vapor bubbles. This also explains why the value of oscillation is bigger.

This article discusses the two-phase flow of solar collector coolant. Therefore, it is desirable to select the density value so that the liquid is rapidly steamed and fast, i.e., it has low oscillation. Based on these results, we can describe the effect of the liquid phase (density) on phase transitions.

Conclusion

The two-phase flow was solved by means of the finite elements in COMSOL Multiphysics computer program using a phase field model based on the equation of phase variable of Chan-Hilliard. According to the problem, the two-phase flow of refrigerants at different densities was reviewed and compared. The phase variable for the refrigerant R-407C is 0.812, the oscillation is 0.24. For refrigerants with a density of 800-900 kg/m^3, this value was about 0.825-0.827, the oscillation was 0.15-0.21. For refrigerants with a density of 1300-1400 kg/m^3, the above values were 0.798-0.799 and fluctuations of 0.24-0.26.

By examining the results, the higher the liquid density, the more rapid phase changes were observed, but the phase of the vapor phase was small. Conversely, if the density is small, the volume of the vapor is high, but the phase exchange is slow.

References

1. Tong L. *Teplootdacha pri kipenii i dvuhfaznoe techenie.* (*Heat transfer at boiling and two-phase flow).* Moscow: Mir, 1969. – 344 p. (in Russian).

2. Jamet D. “Diffuse interface models in fluid mechanics”,

http://pmc.polytechnique.fr/mp/GDR/docu/Jamet.pdf.

3. Sun Y., Beckermann C. “Diffuse interface modeling of two-phase flows based on averaging: mass and momentum equations.” *Physica D* 198 (2004): 281–308.

4. Grzybowski H., Mosdorf R. “Modelling of two-phase flow in a minichannel using level-set method.” *Journal of Physics: Conference Series* 530 (2014): 35-44.

5. Son G., Dhir V.K. “A Level Set Method for Analysis of Film Boiling on an Immersed Solid Surface.” *Numerical Heat Transfer, Part B* 52 (2007): 153–177.

6. Dongsun Lee, Joo-Youl Huh, Darae Jeong. “Physical, mathematical, and numerical derivations of the Cahn–Hilliard equation.” *Computational Materials Science* 81 (2014): 216–225.

7. Labuncov D.A., Yagov V.V. *Mehanika dvuhfaznyh system*. (*Mechanics of motion systems*). Moscow: MEI Publ., 2000. – 374 p. (in Russian).

8. Mohanraj M., Belyayev Ye., Jayaraj S., Kaltayev A. “Research and developments on solar assisted compression heat pump systems - A comprehensive review (Part A: Modeling and modifications).” *Renewable and Sustainable Energy Reviews* 83 (2018): 90-123, IF=9.52.

9. Mohanraj M., Belyayev Ye., Jayaraj S., Kaltayev A. “Research and developments on solar assisted compression heat pump systems - A comprehensive review (Part-B: Applications).” *Renewable and Sustainable Energy Reviews* 83 (2018): 124-155, IF=9.52.

10. Aliuly A., Mohanraj M., Belyayev Ye., Jayaraj S., Kaltayev A. “Numerical modelling of photovoltaic thermal evaporator for heat pumps.” *Special Issue E of Bulgarian Chemical Communications Journal* 48 (2016): 135-139, IF=0.349.

11. Sheng Wang, Xiaotao Bi, Shudong Wang. “Boiling heat transfer in small rectangular channels at low Reynolds number and mass flux.” *Experimental Thermal and Fluid Science* 77 (2016): 234-245.

12. Cristiano Bigonha Tibiriçá, Douglas Martins Rocha, Ilvandro Luiz Souza Sueth Jr., Gustavo Bochio Gerson, Koiti Kurosawa Shimizu, Marcel Cavallini Barbosa, Sabrina dos Santos Ferreira. “A complete set of simple and optimized correlations for microchannel flow boiling and two-phase flow applications.” *Applied Thermal Engineering* 126 (2017): 774-795.

13. Raffaele L. Amalfi, Farzad Vakili-Farahani, John R.Thome “Flow boiling and frictional pressure gradients in plate heat exchangers. Part 1: Review and experimental database.” *International Journal of Refrigeration* 61 (2016): 166-184.

14. Zacarías A., Ventas R., Venegas M., Lecuona A. “Boiling heat transfer and pressure drop of ammonia-lithium nitrate solution in a plate generator.” *International Journal of Heat and Mass Transfer* 53, no. 21–22 (2010): 4768-4779.

IRSTI 27.37.17

S.Ya. Serovajsky, *M.O. Kenzhebayeva

Faculty of Mechanics and Mathematics,
al-Farabi Kazakh National University, Almaty, Kazakhstan,
*e-mail: merey-mex-2017@mail.ru

Modeling of the potential of the gravitational field at the upper boundary of the region with the existence of a subterranean anomaly

Abstract. All of humanity's activities are tied to fuel. Previously, it was coal, now it is oil. In order to find oil or coal in the earth's interior, preliminary analysis and calculations are necessary to confirm their existence, their size, location, type of mineral and much more. The aim of the study is to improve existing models of calculations for the search for minerals. To date, there are many methods and approaches to solving the problem, but they are not yet accurate enough. We solve the inverse problem of gravimetry, based on measurements of the Earth's gravitational field. At this stage, we carefully investigate the direct problem, without affecting the inverse. In the course of the study, we found interesting facts. Namely, the gravitational field on the Earth's surface with a different location of the anomaly has a very unpredictable result. The results of this study showed that lateral boundaries should be 30-50 times farther from the anomaly, with respect to the diameter of the anomaly. In addition, it reveals that the anomaly should be located in the middle of the area. This gives us the most plausible result.
Key words: gravimetry, inverse problem, gravitational field, Poisson equation.

Introduction

One of the most important ways of intelligence and analysis of mineral deposits associated with the detection and identification of gravitational anomaly [1]. Thus based on gravimetric methods identifies various deviations of the gravitational potential, to indicate the presence of any heterogeneities in the considered crustal thickness. Interpretation of the obtained results implies the solution of any inverse problems of gravimetry (see, for example [2, 3, 4, 5, 6, 7, 8]. As is known, inverse problems of gravimetry are essentially incorrect. They not only lack the stability of the resulting solution to the input data, but often there is no uniqueness of the solution of the problem. One of the known optimization methods for their solution is assembling suggested by Strakhov [7, 9], recently from the statistical form this method has been modified to a mixed one with a deterministic approach [3]. In this paper, a gradient-type method is used to solve the problem under consideration, which is regularizing, i.e. conditionally stable. Many studies of methods of the Newton type for the solution of the restoration of the medium boundary in inverse problems of gravimetry were carried out in [5, 6, 7, 10]. The purpose of this paper is to find out exactly what information and with what degree of accuracy can be restored by measuring the potential of the gravitational and its gradient on the surface of the earth.

In this paper we consider the Poisson equation for the potential of the gravitational field in a certain region. The inverse problem is to determine the density of the medium on the basis of measuring the gravitational potential and its derivative on the surface of the earth. In this case, the remaining part of the boundary of the region under consideration is given the potential value, which would be observed in the same region in the absence of a gravitational anomaly.

 Printed in Kazakhstan

Statement of the problem

We will not complicate our task. We consider the structure of the earth in a certain section, i.e. in two-dimensional measurements. We will also consider at the initial stage that our investigated area has a homogeneous structure and the density is the same everywhere, and we know the significance of this density. We assume that there is only one anomaly in the given region. Let this anomaly also have the form of a rectangle. Let us know the location and its form of anomaly. We do not know its density.

It is necessary to determine the density of the anomaly. To find out what kind of material it is.

There are gravimetric values (values of the gravitational field) at the boundaries of the region.

Let Ω (a × b) be a rectangular domain of size a × b. The anomaly has the shape of a rectangle and it is located in the some interval $x_m \le x \le x_n$ (the length at the surface of the earth), $z_k \le z \le z_l$ (the depth of the considered earth cut, with the positive direction of the OZ axis pointing downwards, so that it is convenient to count with positive values of z). The basic gravitational field equation described by the following formula:

$$\Delta\, \varphi = -4\rho\pi G,$$

where φ is the field potential; G, π are constants; ρ is the density of matter; Δ is the Laplace operator.

We denote by $\Delta\, \varphi_0 = -4\rho_0\pi G$ the potential of a gravitational field without anomaly. Here ρ_0 is the density of the considered region without anomaly.

The size of the considered region must be much larger than the size of the anomaly, in order that the potential difference on the boundary of the region be zero. The potential of the anomaly surface has the form of a "cap", and completely covers the anomaly. Thus, the potential of the anomaly field extends beyond the boundary of the anomaly. If the potential difference is not zero at the boundary of the region under consideration, then we artificially expand the area under investigation, so that the dimensions are sufficiently large in relation to the anomaly under investigation. We can expand in depth and width. The upper part of the earth's boundary remains unchanged. We denote the extensible boundary by Γ.

Thus, we calculate the difference

$$-\begin{cases} \Delta\varphi(x,z) = -4\pi\rho(x,z)G, \\ \Delta\varphi_0(x,z) = -4\pi\rho_0(x,z)G. \end{cases}$$

We obtain

$$\Delta\eta(\mathrm{x},\mathrm{z}) = -4\pi\psi(x,z)G,$$

there

$$\begin{cases} \eta(\mathrm{x},\mathrm{z}) = \varphi(\mathrm{x},\mathrm{z}) - \varphi_0(\mathrm{x},\mathrm{z}), \\ \psi(x,z) = \rho(x,z) - \rho_0(x,z). \end{cases}$$

The value of the boundary conditions along the boundary Γ is zero

$$\eta(\mathrm{x},\mathrm{z})|\Gamma = 0.$$

Hence, we have obtained that

$$\psi(x,z) = \begin{cases} 0, & outside\ \Omega, \\ \psi_0, & in\ \ \Omega. \end{cases}$$

Thus, we reduced the original problem with nonzero boundary conditions to an equivalent problem with zero boundary conditions (this method of reducing the problem is called the perturbation method). This greatly facilitates the process of solving the problem.

Now the statement of the problem has the form:

$$\Delta\,\eta(\mathrm{x},\mathrm{z}) = -4\pi\psi(x,z)G, \tag{1}$$

$$\eta(\mathrm{x},\mathrm{z})|\Gamma = 0, \tag{2}$$

$$\eta(x,\mathrm{z}_0)|\mathrm{z}_0 = \eta_1 \neq 0, \tag{3}$$

$$\frac{\partial\eta(x,z)}{\partial z}|\mathrm{z}_0 = \eta_2 \neq 0, \tag{4}$$

$$\psi(x,z) = \begin{cases} 0, & outside\ \Omega, \\ \psi_0, & in\ \ \Omega. \end{cases} \tag{5}$$

The problem (1) – (3) is direct problem for the Poisson equation with boundary conditions. The function η (x, z) is the potential of the gravitational field is differentiated twice in x, and twice in z. Therefore, to solve this Poisson equation, we need four boundary conditions. The equations (2) and (3) provide us with four boundary conditions (along four boundaries). That is, we can solve a direct problem. Find the potential of the field at any point in the region under consideration, with given

conditions on the boundary, we know the value of ψ (x, z) is the difference in the densities of the inhomogeneity and the region under consideration. Unfortunately, we do not know the value of the density of the inhomogeneity! Therefore, it is necessary to insert into the equation (1) the value of ψ (x, z) from equation (5). If ψ (x, z) = 0 outside the Ω, then η (x, z) = 0 outside Ω.

We still have equation (4). The value of the gradient from the potential function of the gravitational field. To solve a direct problem this condition is superfluous, that is, we solve a direct problem without it. To solve the inverse problem, we need condition (4).

We reduce the inverse problem to the optimization problem. We add the functional. Since we do not know the value of ψ_0, we will select it artificially. It must be chosen in such a way that for the solutions of the direct problem the obtained answer η (x, z), when substituted into equation (4), turns it into an identity. Then the chosen ψ_0 is the solution of the inverse problem. Such a method is laborious, perhaps even not feasible, because we may never be able to pick up ψ_0 so as to accurately "get" into η_2. In such cases, the optimization one replaces the original task.

The optimization problem obtained as follows: Instead of checking condition (4), we will minimize the functional

$$I(\psi_0) = \int_0^L \left(\frac{\partial \eta(x,z)}{\partial z}\Big|_{z=0} - \eta_2 \right)^2 dx \to \min. \quad (6)$$

That is, we will select ψ_0 in such a way that the difference between the desired value of η (x, z) and η_2 is minimal.

We will solve the problem with the aid of the gradient method. A gradient method involves the use of a derived functional. It is necessary to calculate the derivative of the functional. We use the definition of the Gato derivative for the functional. The Gato derivative has a sufficient set of properties in order to use it in the gradient method when calculating the inverse gravimetric problem for the model statement.

The Gato derivative has the following form:

$$I'(\psi_0) = 4\pi G \iint_\Omega p dx dz.$$

Results and discussion

The formulation of the problem reduced to the solution of the direct and inverse problem. At the first stage, we must study the direct problem well, check for the presence of deviations and inaccuracies in the various locations of the anomaly within the investigated region. We analyze the change in density to the upper value of the gravitational field. All calculations made on the software product Comsol Multiphysics 5.2. This software product contains all the necessary numerical calculations. The obtained solutions based on the finite element method. This method is the most accurate and universal. The advantage of Comsol Multiphysics 5.2 is in the speed of solving and providing a visual solution of the problem. Unfortunately, it is difficult to solve the inverse problem on Comsol Multiphysics 5.2, but it is quite suitable for solving a direct problem.

The figures below show the last upper layer of the location of the anomaly. In Figure 1 a) you can see a graphic representation of the location of the anomaly, b) a graph of the distribution of the potential of the gravitational field on the earth's surface, c) the distribution of the derivative of the gravitational potential for a given location of the anomaly. Since the graphs are symmetrical about the central location of the anomaly, we will consider only three variants of the location of the anomaly (the anomaly shift occurs from left to right to the central location). Since we need to give three figures for one arrangement, we decided to design them as Figure1 (under one number).

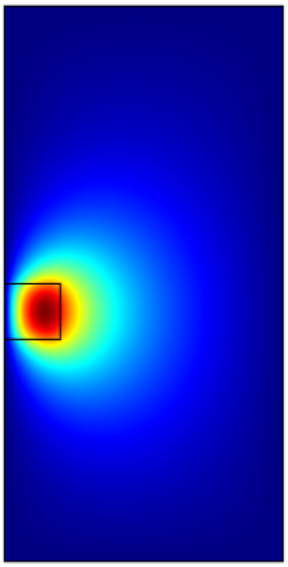

a) The location of the anomaly

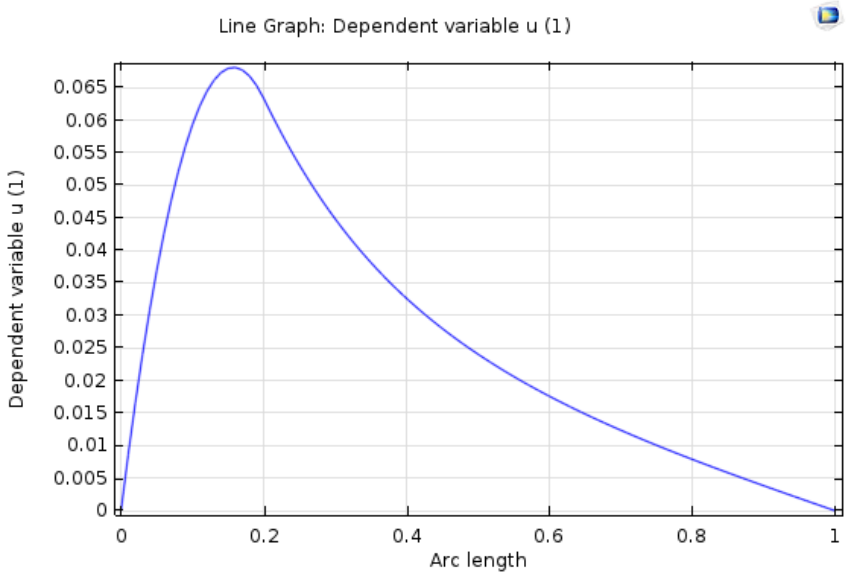

b) The potential of the gravitational field

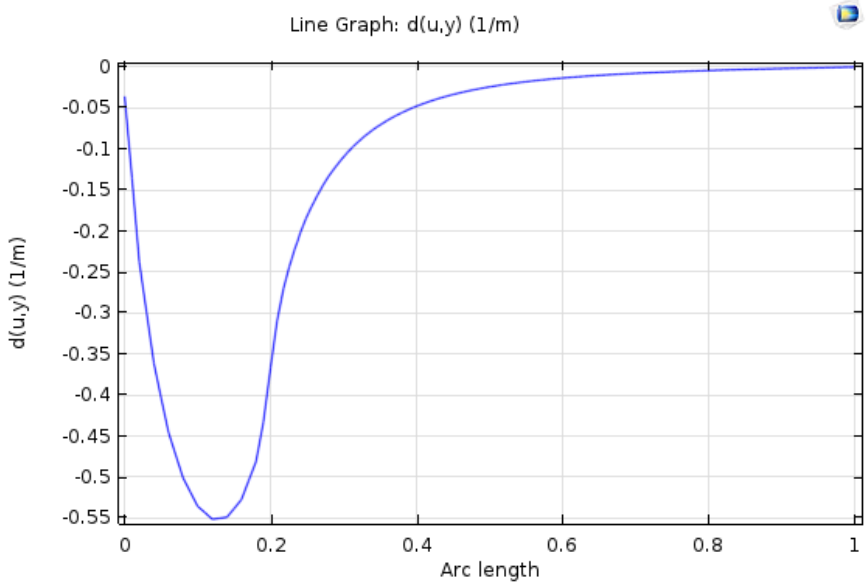

c) The gradient of the potential of the gravitational field on the earth's surface

Figure 1 – Last upper layer of the location of the anomaly

The results of solving a direct problem showed the following. With a different location of the anomaly in the study area, the upper boundary of the gravitational field did not change as expected. Namely, if the anomaly was located closer to the lateral boundaries, then the symmetry of the resulting parabola was greatly changed, even arched. In addition, the peak of the parabola did not lie exactly above the center of the anomaly, but shifted. Thus, introducing distortion and complexity for the reverse restoration of the location of the anomaly. It is connected with the zero boundary conditions, which we asked beforehand, expanding the region. Thus, the compiled mathematical model does not fully describe the process. That is, initially we did not expect an anomaly to be located near the border. The anomaly should be located strictly in the center of the region. The greatest curvature obtained closer to the surface of the earth. The deeper the anomaly, the less the curvature.

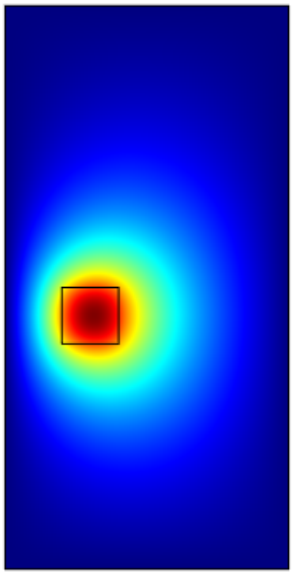

a) The location of the anomaly

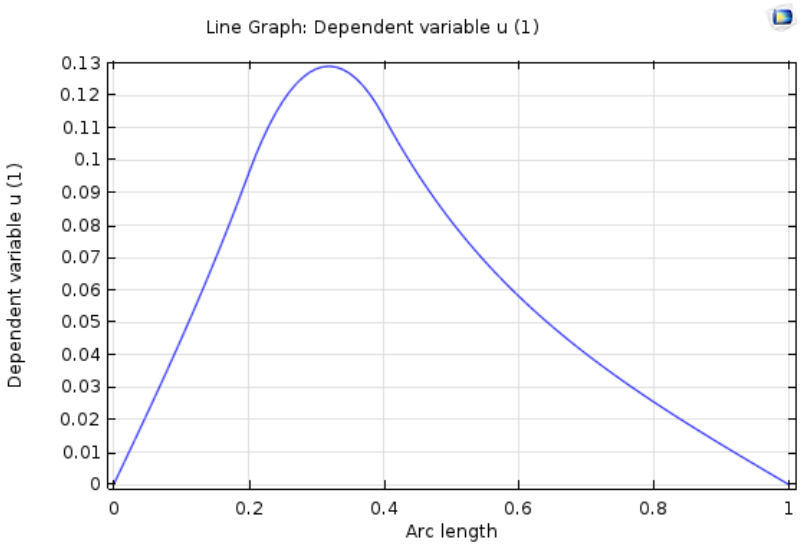

b) The potential of the gravitational field

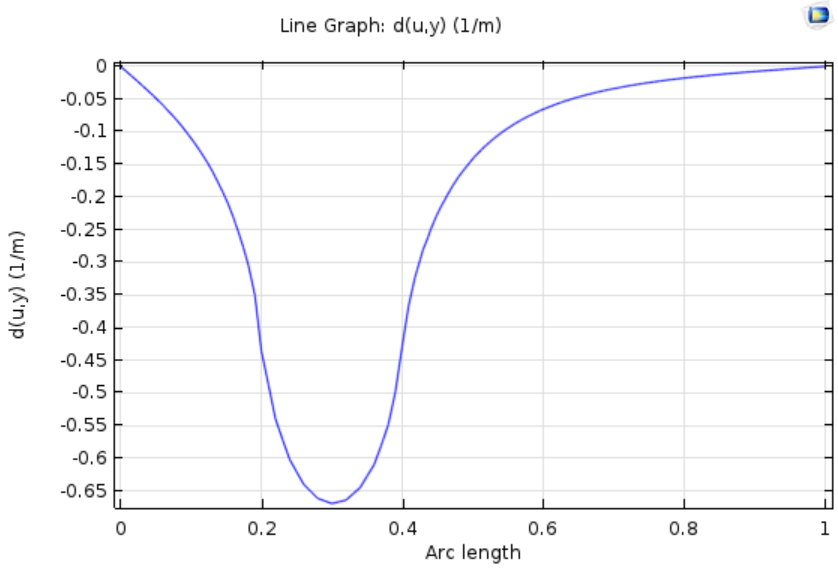

c) The gradient of the potential of the gravitational field on the earth's surface.

Figure 2

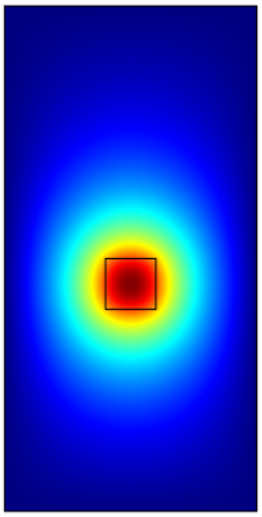

a) The location of the anomaly

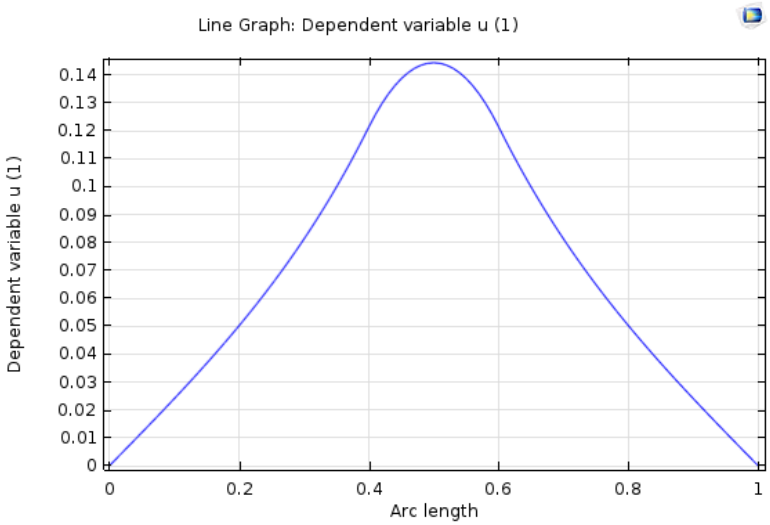

b) The potential of the gravitational field

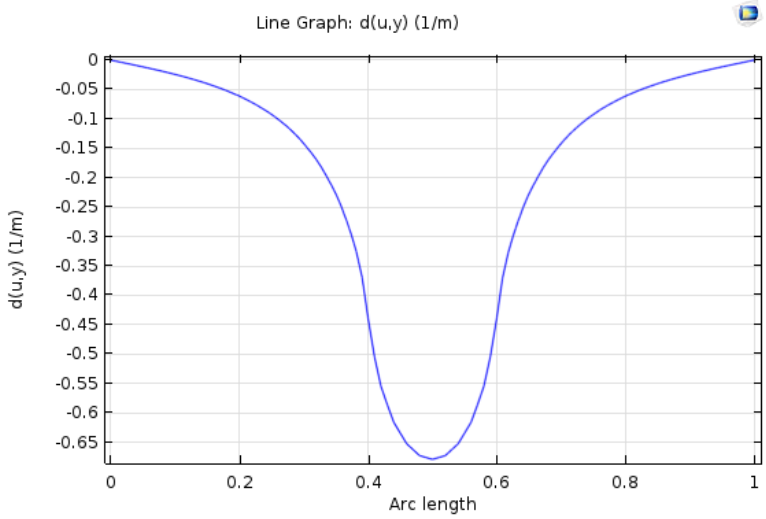

c) The gradient of the potential of the gravitational field on the earth's surface.

Figure 3

Conclusion

The purpose of this article was to show that when studying a region with a subterranean anomaly, one should not place an anomaly close to the lateral boundaries. This gives incorrect results associated with zeroing the boundary conditions. These results will be very useful in the further solution of the inverse problem, since in solving inverse problems we will need to solve the direct problem many times. If there are inaccuracies in the direct problem, then this will necessarily affect the results of the inverse problem. We need to most accurately investigate the direct problem in order to exclude in advance the errors of the direct problem.

References

1. Jacoby W., Smilde P. "Gravity Interpretation: Fundamentals and Application of Gravity Inversion and Geological Interpretation." *Springer Science & Business Media* (2009): 395.

2. Balk P., Dolgal A., Balk T., Khristenko L. "Joint use of inverse gravity problem methods to increase interpretation informativity." *Geofizicheskiy Zhurnal* 37, no. 4 (2017): 75-92.

3. Balk P.I., Yeske A. “Fitting approach of V.N. Strakhov to solving inverse problems of gravity exploration: up-to-date status and real abilities.” *Geophysical journal* 35, no. 1 (2013): 12-26.

4. Vasin V.V., Akimova E.N., Miniakhmetova A.F. “Iterative Newton Type Algorithms and Its Applications to Inverse Gravimetry Problem.” *Vestnik of the South Ural State University.* Series: Mathematical modelling and programming 6, no. 3 (2013): 26-33.

5. Akimova E.N., Vasin V.V., Misilov V.E. “Algorithms for solving inverse gravimetry problems of finding the interface between media on multiprocessing computer systems.” *Vestnik of Ufim State Aviation Technical University* 18, no. 2 (2014): 208-217.

6. Prutkin I., Saleh A. “Gravity and magnetic data inversion for 3D topography of the Mono discontinuity in the northern Red Sea area.” *Journal of Geodynamics* 47, no. 5 (2009): 237-245.

7. Strakhov V.N., Lapina M.I. “The assembly method for solving the inverse problem of gravimetry.” *RAS* 227, no. 2 (1976): 344-347.

8. Mikhailov V.P. *Differential Equations in Partial Derivatives*. Moskow: Nauka Publ., 1976.

9. Kabanikhin S.I. *Inverse and ill-posed problems. Textbook for students of higher educational institutions*. Novosibirsk: Siberian Scientific Publishing House, 2009. – 457 p.

10. Alexidze M.A. *Approximate methods for solving direct and inverse problems of gravimetry*. Moscow: Nauka Publ., 1987. – 333 p.

IRSTI 30.17.51

[1*]Ye. Belyayev, [2]A. Naimanova, [1]A. Kaltayev, [3]S. Jayaraj

[1]al-Farabi Kazakh National University, Almaty, Kazakhstan
[2]Institute of Mathematics and Mathematical Modelling, Ministry of Education and Science, Almaty, Kazakhstan
[3]Department of Mechanical Engineering, National Institute of Technology Calicut-673601, Kerala, India
*e-mail: yerzhan.belyayev@gmail.com

Numerical study of supersonic turbulent free shear layer mixing and combustion

Abstract. Numerical study of two-dimensional supersonic hydrogen-air mixing and combustion in free shear layer is performed. The system of Favre-Averaged Naveir-Stokes equations for multispecies reacting flow is solved using ENO scheme of third-order in accuracy. The k-ε two-equation turbulence models with compressibility correction are applied to calculate the eddy viscosity coefficient. In order to produce the roll-up and pairing of vortex rings, an unsteady boundary condition is applied at the inlet plane. At the outflow, the non-reflecting boundary condition is taken. The influence of different Mach numbers on the formation of vorticity structures and shear layer growth rate are studied. The obtained results are compared with available experimental data and the numerical results of other authors. For the description of reaction pathways of hydrogen, a seven species chemical reaction model by Jachimowski is adopted. The influence of Mach numbers on turbulent mixture and combustion is reported.
Key words: supersonic shear flow, mixing layer, hydrogen combustion, ENO-scheme, turbulence model, seven chemical reactions mechanism.

Introduction

Compressible mixing layer is an important flow in extensive engineering applications. In particular, the shear layer configuration is a simple and yet fundamental to understand how fuel flow will mix and combust with supersonic oxidizer flow in SCRAM jet engines combustion chambers of hypersonic vehicles. As is well known the main objectives of investigating the physical processes in combustion chamber of these engines is aimed to maximize thrust by enhancing the fuel-air mixing and combustion.

It is necessary to take into account the influence of gas-dynamical structure, turbulence effects and chemical reactions for understanding physical structure of fuel-air mixture combustion in numerical model. Studying combustion in shear layer requires accurate predictions of mixing and combustion efficiency to which special attention should be paid to simulation the unsteady behavior of mixing layer roll-up and vortex formation. The gas-dynamical structure of mixing between two parallel super-subsonic flows has been comprehensively studied by many investigators. Nowadays, there are a large number of works on experimental [1-9], analytical [10-11] and numerical [12-27] study of this problem in the view of above physical effects as separately as with including all of them. Experimental efforts investigating the roll of large scale structures and growth mechanisms in compressible mixing layer have been done in sufficient details by researchers [1-6]. There are a great deal of researches devoted to the turbulence problem and influence of turbulence quantities on the mixing and vorticity formation [7-9].

The behavior of shear layers of perfect gases have been entirely realized in mathematical models, but the practical design of supersonic ramjet (scramjet) engines requires the shear layer growth enhancements for multispecies gases. Successful numerical models of such flows with the detail flow physics represent a difficult problem. Therefore the investigators studied some physical phenomena

 Printed in Kazakhstan

separately or proposed the numerical method, which are important for solution of this complex system. In [12, 15-16] have been modeled the free shear layer flowfield structures using the system of compressible Euler equations. For example, in [12] have been numerically studied the supersonic-subsonic free shear layer applying high order WENO scheme to the system of 2D axisymmetric Euler equations and numerical turbulence model taken as a SGS model. During numerical experiment revealed that at high-convective Mach number turbulence mixing rates reduces and vortex roll-up and pairing suppresses. In [13-14, 17] have been performed numerical experiment based on the system of Navier-Stokes equations for monatomic (air) gas to study the growth of instabilities in supersonic free shear layers. Xiao-Tian Shi et al. [17] conducted numerical simulations of compressible mixing layers based on discontinuous Galerkin method with inflow perturbation for prediction of the flowfield structures obtained in experiments. Numerical experiments of influence of unsteady inflow perturbations on the mixing in supersonic free shear layers on the basis of second and fourth order MacCormack scheme have been performed by authors [13-14]. Their studies revealed that normal velocity perturbation is more efficient than streamwise and spanwise. To date rarely performed the numerical investigation of growth of instabilities in shear layer using unsteady disturbances for multispecies gas mixture. In these works have accurately predicted the gas-dynamical structure of shear layers by advanced numerical methods without chemical reactions terms.

The mathematical model and numerical method of solution of supersonic combustion in shear layer flow has been performed for laminar [18-24] and turbulent [25-27] flows. In these works the basic efforts is directed on analysis of influence different effects such as inlet swirl, initial temperature, velocity and pressure ratios on ignition time delay. The detail chemical reaction mechanism during calculation have been adopted in [21, 25-26], while in [18-19, 23] reduced reaction mechanisms. For example, the numerical study of ignition in supersonic turbulent hydrogen-air mixing layer including detail chemical kinetics and advection upstream splitting method ($AUSM^+$) have performed in [25-26]. In this study illustrates that the swirl used in the fuel and oxidizer flows decreases the ignition time delay significantly by enhancing the swirl angle [25-26]. Numerically investigation of the ignition and combustion of hydrogen-air and ethylene-air mixture in supersonic shear flow configuration on the base of fourth-order accurate in space and second-order accurate in time MacCormak-like scheme with compact difference operators and automatic reduction procedure chemical kinetics, for various Mach numbers and temperatures have been made in [18-19]. In these investigations with the simulation of reacting shear layer were insufficiently paid attention to the vortical nature of mixing layer. Up to date there are few works on numerical study of unsteady combustion in supersonic shear layer.

In the present study, the third order essentially non-oscillatory (ENO) finite difference scheme is adopted to solve the system of Favre-averaged Navier-Stokes equations with chemical kinetics terms to supersonic planar shear layer. The k-ε two-equation turbulence model with compressibility correction is used to predict the turbulence characteristics. To verify the mathematical model and numerical algorithm obtained results compared with experimental study of Samimy and Elliot [8-9] for supersonic-subsonic free shear layer. Simulation of the flame propagation with combustion products formation is performed including the seven reaction and seven component Jachimowski's kinetics mechanism. The effect of flows Mach number on turbulent mixture and combustion of hydrogen-air flow is reported. For more information, see [36] and references therein.

The inflow physical parameters profile across the non-premixed hydrogen (fuel) and air stream at the splitter plate leading edge is assumed to vary smoothly according to a hyperbolic-tangent function (Fig. 1).

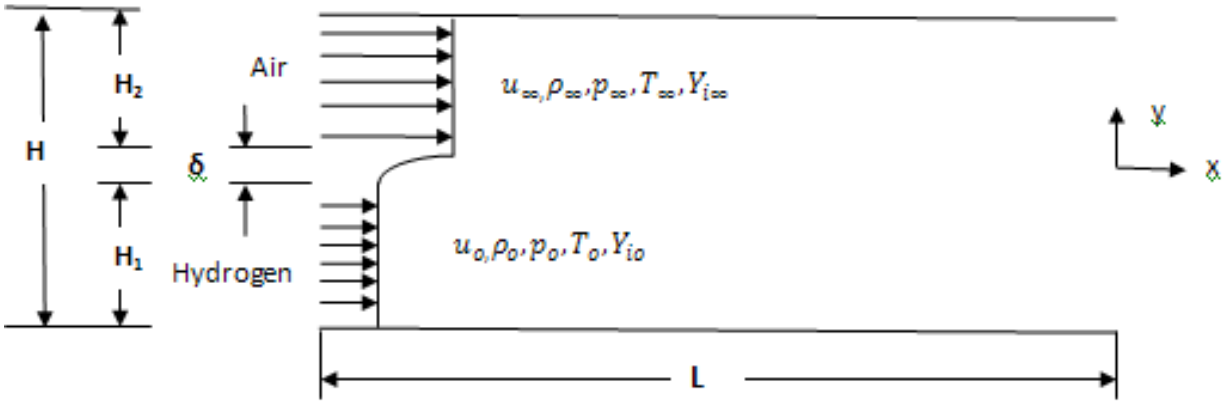

Figure 1 – An illustration of the flow configuration

Mathematical model

The two-dimensional Favre-averaged Navier-Stokes equations for multi-species flow with chemical reactions is:

$$\frac{\partial \vec{U}}{\partial t} + \frac{\partial (\vec{E} - \vec{E}_v)}{\partial x} + \frac{\partial (\vec{F} - \vec{F}_v)}{\partial z} = 0, \qquad (1)$$

where the vector of the dependent variables and the vector fluxes are given as

$$\vec{U} = \begin{pmatrix} \rho \\ \rho u \\ \rho w \\ E_t \\ \rho Y_k \\ \rho k \\ \rho \varepsilon \end{pmatrix}, \quad \vec{E} = \begin{pmatrix} \rho u \\ \rho u^2 + p \\ \rho uw \\ (E_t + p)u \\ \rho u Y_k \\ \rho uk \\ \rho u\varepsilon \end{pmatrix}, \quad \vec{F} = \begin{pmatrix} \rho w \\ \rho uw \\ \rho w^2 + p \\ (E_t + p)w \\ \rho w Y_k \\ \rho wk \\ \rho w\varepsilon \end{pmatrix},$$

$$\vec{E}_v = \left(0, \tau_{xx}, \tau_{xz}, u\tau_{xx} + w\tau_{xz} - q_x, J_{kx}, \frac{1}{\mathrm{Re}}\left(\mu_l + \frac{\mu_t}{\sigma_k}\right)\frac{\partial k}{\partial x}, \frac{1}{\mathrm{Re}}\left(\mu_l + \frac{\mu_t}{\sigma_\varepsilon}\right)\frac{\partial \varepsilon}{\partial \mathrm{x}}\right)^T,$$

$$\vec{F}_v = \left(0, \tau_{xz}, \tau_{zz}, u\tau_{xz} + w\tau_{zz} - q_z, J_{kz}, \frac{1}{\mathrm{Re}}\left(\mu_l + \frac{\mu_t}{\sigma_k}\right)\frac{\partial k}{\partial z}, \frac{1}{\mathrm{Re}}\left(\mu_l + \frac{\mu_t}{\sigma_\varepsilon}\right)\frac{\partial \varepsilon}{\partial z}\right)^T,$$

$$\vec{W} = \left(0,0,0,0,0, \left[P_k - \rho\varepsilon\left(1 + \alpha M_t^2\right) + D\right], \left[C_{\varepsilon 1} P_k \varepsilon / k - C_{\varepsilon 2} f_{\varepsilon 2} \rho \varepsilon^2 / k\right]\right)^T$$

Here, the viscous stresses, thermal conduction, and diffusion flux of species are:

$$\tau_{xx} = \frac{1}{\mathrm{Re}}\left(\mu_l + \frac{\mu_t}{\sigma_k}\right)\left(2u_x - \frac{2}{3}(u_x + w_z)\right);$$

$$\tau_{zz} = \frac{1}{\mathrm{Re}}\left(\mu_l + \frac{\mu_t}{\sigma_k}\right)\left(2w_z - \frac{2}{3}(u_x + w_z)\right);$$

$$\tau_{xz} = \tau_{zx} = \frac{1}{\mathrm{Re}}\left(\mu_l + \frac{\mu_t}{\sigma_k}\right)(u_z + w_x);$$

$$q_x = \frac{1}{\Pr \mathrm{Re}}\left(\mu_l + \frac{\mu_t}{\sigma_k}\right)\frac{\partial T}{\partial x} + \frac{1}{\gamma_\infty M_\infty^2}\sum_{k=1}^{N} h_k J_{xk};$$

$$q_z = \frac{1}{\Pr \mathrm{Re}}\left(\mu_l + \frac{\mu_t}{\sigma_k}\right)\frac{\partial T}{\partial z} + \frac{1}{\gamma_\infty M_\infty^2}\sum_{k=1}^{N} h_k J_{zk};$$

$$J_{kx} = -\frac{1}{Sc\,\mathrm{Re}}\left(\mu_l + \frac{\mu_t}{\sigma_k}\right)\frac{\partial Y_k}{\partial x},$$

$$J_{kz} = -\frac{1}{Sc\,\mathrm{Re}}\left(\mu_l + \frac{\mu_t}{\sigma_k}\right)\frac{\partial Y_k}{\partial z}.$$

Parameters of the turbulence are:

$$P_k = \tau_{txx}\frac{\partial u}{\partial x} + \tau_{txz}\frac{\partial u}{\partial z} + \tau_{tzx}\frac{\partial w}{\partial x} + \tau_{tzz}\frac{\partial w}{\partial z};$$

$$\tau_{txx} = \frac{\mu_t}{\mathrm{Re}}\left(2\frac{\partial u}{\partial x} - \frac{2}{3}\left(\frac{\partial u}{\partial x} + \frac{\partial w}{\partial z}\right)\right);$$

$$\tau_{txz} = \frac{\mu_t}{\mathrm{Re}}\left(\frac{\partial u}{\partial z} + \frac{\partial w}{\partial x}\right);$$

$$\tau_{tzz} = \frac{\mu_t}{\mathrm{Re}}\left(2\frac{\partial w}{\partial z} - \frac{2}{3}\left(\frac{\partial u}{\partial x} + \frac{\partial w}{\partial z}\right)\right);$$

$$M_t^2 = 2 \cdot M_\infty^2 \cdot k / T;$$

$$f_{\varepsilon 2} = 1 - 0.3 \cdot \exp\left(-\mathrm{Re}_t^2\right), \quad \mathrm{Re}_t = \mathrm{Re}\left(\frac{\rho k^2}{\mu_l \varepsilon}\right);$$

$$C_{\varepsilon 1} = 1.44; C_{\varepsilon 2} = 1.92; \sigma_k = 1.0; \sigma_\varepsilon = 1.3,$$

where k, ε – turbulent kinetic energy, rate of dissipation of turbulent kinetic energy. P_k – is turbulence production term, M_t – is the turbulence Mach number.

Y_k – is the mass fraction of k^{th} species, $\dot{\omega}_k$ – rate of mass production of species, $k = 1 \ldots N$, with N – number a components in a gas mixture. The thermal equation for multi-species gas is:

$$p = \frac{\rho T}{\gamma_\infty M_\infty^2 W}, \quad W = \left(\sum_{k=1}^{N}\frac{Y_k}{W_k}\right)^{-1}, \quad \sum_{k=1}^{N} Y_k = 1 \qquad (2)$$

where W_k is the molecular weight of the species.

The equation for a total energy is given by

$$E_t = \frac{\rho h}{\gamma_\infty M_\infty^2} - p + \frac{1}{2}\rho\left(u^2 + w^2\right) \qquad (3)$$

The enthalpy of the gas mixture is calculated according to $h = \sum_{k=1}^{N} Y_k h_k$, with specific enthalpy of k^{th} species evaluated suing $h_k = h_k^0 + \int_{T_0}^{T} c_{pk} dT$.

The specific heat at constant pressure for each component c_{pk} is:

$$c_{pk} = C_{pk} / W, \; C_{pk} = \sum_{i=1}^{5} \overline{a}_{ki} T^{(i-1)}, \; \overline{a}_{jk} = a_{jk} T_\infty^{\;j-1}$$

where the molar specific heat C_{pk} is given in terms of the fourth degree polynomial with respect to temperature, consistent with the JANAF Thermochemical Tables [28].

The system of the equations (1) is written in the conservative, dimensionless form. The air flow parameters are $\rho_\infty, u_\infty, w_\infty, T_\infty, h_\infty, W_\infty, R_\infty$, hydrogen jet parameters are $\rho_0, u_0, w_0, T_0, h_0, W_0, R_0$. The governing parameters are the air flow parameters, the pressure and total energy are normalized by $\rho_\infty u_\infty^2$, the enthalpy by $R_0 T_\infty / W_\infty$, the molar specific heat by R_0 and the spatial distances by the thickness of the splitter plate δ.

The coefficient of viscosity is represented in the form of the sum of μ_l – molecular viscosity and μ_t – turbulent viscosity: $\mu = \mu_l + \mu_t$, where μ_t is defined according to k-ε model with compressibility correction. The mixture averaged molecular viscosity is evaluated using from Wilke's formula.

The chemical reactions of hydrogen H_2 with air are described using Jachimowski's seven species model used in the NASA SPARK code [28]. This model includes the following seven species: $H_2, O_2, H_2O, OH, H, O, N_2$.

Initial and boundary conditions

At the entrance:

$u_1 = M_0\sqrt{\frac{\gamma_0 R_0 T_0}{W_0}}$, $w_1 = 0$, $p_1 = p_0$, $T_1 = T_0$, $Y_{k1} = Y_{k0}$,

$k = k_0$, $\varepsilon = \varepsilon_0$ at $x = 0$, $0 \leqslant z < \mathrm{H}_1$.

$u_2 = M_\infty\sqrt{\frac{\gamma_\infty R_0 T_\infty}{W_\infty}}$, $w_2 = 0$, $p_2 = p_\infty$, $T_2 = T_\infty$, $Y_{k2} = Y_{k\infty}$, $k = k_\infty$, $\varepsilon = \varepsilon_\infty$ at $x=0$, $H_1 + \delta \leqslant z \leqslant H_2$.

In the region of $H_1 \leqslant z \leqslant H_1 + \delta$ all physical variables are varied smoothly from hydrogen (fuel) flow to air flow using a hyperbolic-tangent function of any variable φ, so the inflow profiles are defined by

$$\phi(z) = 0.5(\phi_2 + \phi_1) + 0.5(\phi_2 - \phi_1)\tanh(0.5z/\theta)$$

at $x = 0$, $0 \le z \le H$.

where $\phi = (u, v, p, T, Y_k, k, \varepsilon)$, θ - is the momentum thickness. The pressure is assumed to be uniform across the shear layer. On the lower and upper boundary the condition of symmetry are imposed. At the outflow, the non-reflecting boundary condition is used [29].

In order to produce the roll-up and pairing of vortex rings, an unsteady boundary condition is also applied at the inlet plane, i.e.

$$u = u(z) + A\Delta U Gaussian\,(z)\cos(\omega t)$$

$$w = \Delta w_{factor}\, A\Delta U Gaussian\,(z)\sin(\omega t)$$

$$Gaussian(z) = \exp(-z^2/2\sigma^2),$$

where $u(z)$ _ velocity profile at the entrance corresponding to hyperbolic-tangent function. The unsteady part of the condition is about 0.2-0.3 percent of the Favre-averaged velocity. $\Delta U = (u_\infty - u_0)$ – the difference of two stream velocities which measures the strength of shearing. $Gaussian\,(z)$ – is a Gaussian function which has a peak value of unity at z=0 and the $\pm 2\sigma$ width was matched to the vorticity layer thickness at the entrance. Coefficient A is the disturbance amplitude which is defined from the $A \cdot \Delta U$, where this product was specified to be 0.2-0.3 percent of the higher inflow speed. The Δw_{factor} was set at 0.7 (70%) of $A \cdot \Delta U$ based on [16]. The $\omega = 2\pi\left(\frac{\left(\sqrt{\frac{\gamma_0 R_0 T_0}{W_0}} + \sqrt{\frac{\gamma_\infty R_\infty T_\infty}{W_\infty}}\right)/2}{2\delta_w}\right)$ is the frequency of perturbation. $\delta_w = \frac{(u_\infty - u_0)}{(\partial u/\partial z)_{\max}}$ – is the vorticity thickness.

Method of solution

To take into account the flow in the shear (at the entrance) and mixing layer, i.e., in regions of high gradients, more accurately, we refine the grid in the longitudinal and transverse directions by the transformations

$$\frac{\partial \tilde{U}}{\partial t} + \frac{\partial \tilde{E}}{\partial \xi} + \frac{\partial \tilde{F}}{\partial \eta} = \frac{\partial \tilde{E}_{v2}}{\partial \xi} + \frac{\partial \tilde{E}_{vm}}{\partial \xi} + \frac{\partial \tilde{F}_{v2}}{\partial \eta} + \frac{\partial \tilde{F}_{vm}}{\partial \eta}, \qquad (4)$$

where $\tilde{U} = \vec{U}/J$, $\tilde{E} = \xi_x \vec{E}/J$, $\tilde{F} = \eta_z \vec{F}/J$, $\tilde{E}_{v2} = \xi_x \vec{E}_{v2}/J$, $\tilde{E}_{vm} = \xi_x \vec{E}_{vm}/J$, $\tilde{F}_{v2} = \eta_z \vec{F}_{v2}/J$, $\tilde{F}_{vm} = \eta_z \vec{F}_{vm}/J$, and $J = \partial(\xi,\eta)/\partial(x,z)$ is the Jacobian of mapping.

System (4) linearized with respect to the vector U in form:

$$\tilde{U}^{n+1} + \Delta t\left(\frac{\partial \tilde{E}^{n+1}}{\partial \xi} + \frac{\partial \tilde{F}^{n+1}}{\partial \eta} - \frac{\partial \tilde{E}_{vm}^{n+1}}{\partial \xi} - \frac{\partial \tilde{E}_{v2}^{n+1}}{\partial \xi} - \frac{\partial \tilde{F}_{vm}^{n+1}}{\partial \eta} - \frac{\partial \tilde{F}_{v2}^{n+1}}{\partial \eta}\right) = \tilde{U}^n + O(\Delta t^2). \qquad (5)$$

Here,

$$\tilde{E}^{n+1} \approx A_\xi^n \tilde{U}^{n+1},\ \tilde{F}^{n+1} \approx B_\eta^n \tilde{U}^{n+1}, \qquad (6)$$

$A_\xi = \xi_x A$, $B_\eta = \eta_z B$, $A = \partial\vec{E}/\partial\vec{U}$, $B = \partial\vec{F}/\partial\vec{U}$ – are the Jacobian matrices [32-33].

The terms containing the second derivatives are presented as sums of two vectors:

$$\tilde{E}_{v2}^{n+1} = \tilde{E}_{v21}^{n+1} + \tilde{E}_{v22}^{n},\quad \tilde{F}_{v2}^{n+1} = \tilde{F}_{v21}^{n+1} + \tilde{F}_{v22}^{n}, \qquad (7)$$

where the vectors $\tilde{E}_{v21}^{n+1}$, $\tilde{F}_{v21}^{n+1}$ are written in the following form:

$$\widetilde{E}_{v21}^{n+1}=\frac{\mu_t\xi_x}{\mathrm{Re}\,J}\left[0,\frac{4}{3}\frac{\partial}{\partial\xi}\left(\frac{u\rho}{\rho}\right)^{n+1},\frac{\partial}{\partial\xi}\left(\frac{w\rho}{\rho}\right)^{n+1},\frac{\gamma}{\mathrm{Pr}}\frac{\partial}{\partial\xi}\left(\frac{E_t}{\rho}\right)^{n+1}\right]^T,$$

$$\widetilde{F}_{v21}^{n+1}=\frac{\mu_t\eta_z}{\mathrm{Re}\,J}\left[0,\frac{\partial}{\partial\eta}\left(\frac{u\rho}{\rho}\right)^{n+1},\frac{4}{3}\frac{\partial}{\partial\eta}\left(\frac{w\rho}{\rho}\right)^{n+1},\frac{\gamma}{\mathrm{Pr}}\frac{\partial}{\partial\eta}\left(\frac{E_t}{\rho}\right)^{n+1}\right]^T,$$

and the vectors $\widetilde{E}_{v12}^{n}$, $\widetilde{F}_{v22}^{n}$ contain the remaining dissipative functions of the form:

$$\widetilde{E}_{v12}^{n}=\frac{\xi_x^2}{\mathrm{Re}\,J}\left[0,0,0,\left[\left(\mu-\frac{\gamma\mu}{\mathrm{Pr}}\right)\left(w\frac{\partial w}{\partial\xi}\right)+\left(\frac{4}{3}\mu-\frac{\gamma\mu}{\mathrm{Pr}}\right)u\frac{\partial u}{\partial\xi}\right]^n\right]^T,$$

$$\widetilde{F}_{v22}^{n}=\frac{\eta_z^2}{\mathrm{Re}\,J}\left[0,0,0,\left[\left(\mu-\frac{\gamma\mu}{\mathrm{Pr}}\right)\left(u\frac{\partial u}{\partial\eta}\right)+\left(\frac{4}{3}\mu-\frac{\gamma\mu}{\mathrm{Pr}}\right)w\frac{\partial w}{\partial\eta}\right]^n\right]^T,$$

$$\tilde{E}_{vm}=\frac{\xi_x\mu_t}{ReJ}\left[0,-\frac{2}{3}\left(\eta_z\frac{\partial w}{\partial\eta}+\zeta_y\frac{\partial v}{\partial\zeta}\right),\eta_z\frac{\partial u}{\partial\eta},-\frac{2}{3}\left(\zeta_y u\frac{\partial v}{\partial\zeta}+\eta_z u\frac{\partial w}{\partial\eta}\right)+\left(\eta_z w\frac{\partial u}{\partial\eta}+\zeta_y v\frac{\partial u}{\partial\zeta}\right)\right],.$$

$$\tilde{F}_{vm}=\frac{\eta_z\mu_t}{ReJ}\left[0,\eta_z\frac{\partial w}{\partial\eta},-\frac{2}{3}\left(\xi_x\frac{\partial u}{\partial\xi}+\zeta_y\frac{\partial w}{\partial\zeta}\right),\left(\xi_x u\frac{\partial w}{\partial\xi}+\zeta_y u\frac{\partial w}{\partial\zeta}\right)-\frac{2}{3}\left(\xi_x w\frac{\partial u}{\partial\xi}+\zeta_y w\frac{\partial v}{\partial\zeta}\right)\right].$$

According to a principle of construction ENO scheme [30-31] the system (5) for integration on time is formally represented as:

$$\begin{aligned}&\Delta\tilde{U}^{n+1}+\\&+\Delta t\left[\left(\hat{A}^{+}+\hat{A}^{-}\right)\frac{\partial\vec{E}^{m}}{\partial\xi}+\left(\hat{B}^{+}+\hat{B}^{-}\right)\frac{\partial\vec{F}^{m}}{\partial\eta}-\right.\\&\left.-\left[\frac{\partial(\tilde{E}_{v2}{}^{n+1}+\tilde{E}_{vm}{}^{n})}{\partial\xi}-\frac{\partial(\tilde{F}_{v2}{}^{n+1}+\tilde{F}_{vm}{}^{n})}{\partial\eta}\right]\right]=\\&=O\left(\tfrac{1}{2}\Delta t^2\right)\end{aligned}\qquad(8)$$

Here $\vec{E}^{m}$, $\vec{F}^{m}$ is called the modified flux vector. It consists from the original flux vector ($\tilde{E}$, $\tilde{F}$ and additional terms of third-order accuracy $\vec{E}_\xi,\vec{D}_\xi$, $\vec{E}_\eta,\vec{D}_\eta$) :

$$\vec{E}^{m}=\tilde{E}^{n+1}+(\vec{E}_\xi+\vec{D}_\xi)^n\ ,\qquad(9)$$

modified flux $\vec{F}^{m}$ is written similarly and $A^{+}+A^{-}=I$, $A^{\pm}=A^{\pm}A^{-1}$, $B^{\pm}=B^{\pm}B^{-1}$, I - unity matrix.

Applying factorization to (8), we obtain two one-dimensional operators, which are resolved by matrix sweep:

Step 1:

$$\left[I + \Delta t \left\{ (A^{+}_{i-1/2}\Delta_{-} A^{n}_{\xi} + A^{-}_{i+1/2}\Delta_{+} A^{n}_{\xi}) + \Delta \frac{\mu_t \xi_x^2}{\mathrm{Re}\, J} \Delta \frac{1}{U_1^n} \right\} \right] \mathrm{U}^{*} = RHS^{n}_{\xi} + RHS^{n}_{\eta}$$

Step 2:

$$\left[I + \Delta t \left\{ (B^{+}_{j-1/2}\Delta_{-} B^{n}_{\eta} + B^{-}_{j+1/2}\Delta_{+} B^{n}_{\eta}) + \Delta \frac{\mu_t \eta_z^2}{\mathrm{Re}\, J} \Delta \frac{1}{U_1^n} \right\} \right] \tilde{\mathrm{U}}^{n+1} = \mathrm{U}^{*}, \tag{10}$$

$$RHS^{n}_{\xi} = A^{-}_{i+1/2j} \left[\left(\vec{E}_{\xi} + \vec{D}_{\xi} \right)_{i+1j} - \left(\vec{E}_{\xi} + \vec{D}_{\xi} \right)_{ij} \right]^{n} + A^{+}_{i-1/2j} \left[\left(\vec{E}_{\xi} + \vec{D}_{\xi} \right)_{ij} - \left(\vec{E}_{\xi} + \vec{D}_{\xi} \right)_{i-1j} \right]^{n},$$

$$A^{-}_{i+1/2j} \left[\left(\vec{E}_{\zeta} + \vec{D}_{\zeta} \right)_{ij} \right]^{n} = \left(\boldsymbol{minmod} \left(\overline{E}_{\xi i+1/2j}\ \overline{E}_{\xi i-1/2j} \right) + \right.$$

$$\left. + \begin{cases} \dot{\boldsymbol{m}} \left(\Delta_{-} D_{\xi i+1/2j},\ \Delta_{+} D_{\xi i+1/2j} \right) & \text{if} \quad \left| \Delta_{-} \tilde{U}_{ij} \right| > \left| \Delta_{+} \tilde{U}_{ij} \right| \\ \dot{\boldsymbol{m}} \left(\Delta_{-} \overline{D}_{\xi i-1/2j},\ \Delta_{+} \overline{D}_{\xi i-1/2j} \right) & \text{if} \quad \left| \Delta_{-} \tilde{U}_{ij} \right| \le \left| \Delta_{+} \tilde{U}_{ij} \right| \end{cases} \right),$$

$$A^{+}_{i-1/2j} \left[\left(\vec{E}_{\xi} + \vec{D}_{\xi} \right)_{ij} \right]^{n} = R\, \Lambda^{+} R^{-1}_{i-1/2j} \left[\left(\boldsymbol{minmod} \left(\overline{E}_{\xi i+1/2j}\ \overline{E}_{\xi i-1/2j} \right) - \right. \right.$$

$$\left. \left. - \begin{cases} \dot{\boldsymbol{m}} \left(\Delta_{-} D_{\xi i-1/2j},\ \Delta_{+} D_{\xi i-1/2j} \right) & \text{if} \quad \left| \Delta_{-} \tilde{U}_{ij} \right| \le \left| \Delta_{+} \tilde{U}_{ij} \right| \\ \dot{\boldsymbol{m}} \left(\Delta_{-} \overline{D}_{\xi i-1/2j},\ \Delta_{+} \overline{D}_{\xi i-1/2j} \right) & \text{if} \quad \left| \Delta_{-} \tilde{U}_{ij} \right| \le \left| \Delta_{+} \tilde{U}_{ij} \right| \end{cases} \right],$$

$$\overline{E}_{\xi i\pm 1/2j} = \left(R\, sign\,(\Lambda) R^{-1} \right)_{i\pm 1/2j} \frac{1}{2} \left[I - \frac{\Delta t}{\Delta \xi} \left(R\, |\Lambda|\, R^{-1} \right)_{i\pm 1/2} \right] \Delta_{\pm} \tilde{E}_{ij},$$

$$\overline{D}_{\xi i\pm 1/2j} = \left(R\, sign\,(\Lambda) R^{-1} \right)_{i\pm 1/2j} \frac{1}{6} \left[\frac{\Delta t^2}{\Delta \xi^2} \left(R\, |\Lambda|\, R^{-1} \right)^2_{\pm} - I \right] \Delta_{\pm} \tilde{E}_{ij},$$

$$D_{\xi i\pm 1/2j} = \overline{E}_{\xi i\pm 1/2j} + \overline{D}_{\xi i\pm 1/2j},$$

where:

$$\boldsymbol{minmod}\,(a,b) = \begin{cases} s \cdot min\left(|a|, |b| \right) & \text{if} \quad sign(a) = sign(b) = s \\ 0 & \text{other} \end{cases},$$

$$\dot{\boldsymbol{m}}(a,b) = \begin{cases} a & \text{if} \quad |a| \le |b| \\ b & \text{if} \quad |a| > |b| \end{cases}.$$

The second term $RHS^n{}_\eta$ is written similarly.

In approximation of derivatives in convective and diffusion terms, we use second-order central-difference operators.

The numerical solution of the system (5) is calculated in two steps. The first determines the dynamic parameters and second determines the mass species.

Then it is necessary to define Jacobian matrix which in a case of the thermally perfect gas represents difficult task. This problem is connected with the explicit representation of pressure through the unknown parameters. Here pressure is determined by introducing an effective adiabatic parameter of the gas mixture [34].

$$\bar{\gamma} = \frac{h_{sm}}{e_{sm}}\ , \qquad (11)$$

where $h_{sm} = \sum_{i=1}^{N} Y_i \int_{T_0}^{T} c_{p_i} dT$, $e_{sm} = \sum_{i=1}^{N} Y_i \int_{T_0}^{T} c_{v_i} dT$ – is the enthalpy and internal energy of the mixture minus the heat and energy of formation; $T_0 = 293\ K$ - is the standard temperature of formation, which allows to write an expression for the pressure

$$p = (\bar{\gamma} - 1)\left[E_t - \frac{1}{2}\rho\left(u^2 + w^2\right) - \rho\frac{h_0}{\gamma_\infty M_\infty^2} \right] + \frac{\rho T_0}{M_\infty^2 W}.$$

The temperature is found from the Newton-Raphson iteration [32-33, 35].

The equations for species are solved by the scalar sweep, where in the first-step convection and diffusion terms are included and calculated using ENO scheme [30-31]. In the second-step, the matrix equation with terms ($\dot{w}_k = W_k \dot{\omega}_k$) is solved implicitly. These source terms $\dot{W}_k$ are linearized by expansion in a Taylor series,

$$\dot{W}_k^{n+1} = \dot{W}_k^n + \gamma\left(\frac{\partial \dot{W}_k}{\partial Y_m}\Delta Y_m + \frac{\partial \dot{W}_k}{\partial T}\Delta T + \frac{\partial \dot{W}_k}{\partial \rho}\Delta\rho \right)$$

Results and discussion

The parameters of coordinate transformation have the form:

$$\xi(x) = H\left[(\beta+1) - (\beta-1)\left(\frac{\beta+1}{\beta-1}\right)^{1-\frac{x}{L}} \right] \Bigg/ \left[\left(\frac{\beta+1}{\beta-1}\right)^{1-\frac{x}{L}} + 1 \right], \quad \eta(z) = K + \frac{1}{\tau} arsh\left[\left(\frac{z}{z_c} - 1\right) sh(\tau K) \right],$$

$$K = \frac{1}{2\tau} \ln\left[\left(1 + (e^\tau - 1)\frac{z_c}{H}\right) \Bigg/ \left(1 - (e^\tau - 1)\frac{z_c}{H}\right) \right],$$

β, τ are refinement factors (β>1 and τ>1), L – is the length of the computational domain in the generalized coordinates, and z_c – is the point with respect to which grid refinement is performed.

Previously the shear layer problem for monatomic (air) gas has been tested by the following parameters: M_0 = 0.51, T_0 = 285.07 K, P_0 = 56088.91 Pa, M_∞ = 1.8, T_∞ = 176.58 K, P_∞ = 54648.65 Pa. The computational grid is 526x201. The channel height and length were 8 cm and 50 cm, respectively. The splitter plate thickness is 0.3175 cm, and at the trailing edge is 0.05 cm. The initial momentum thickness $\theta = \int_{-\infty}^{+\infty} \left(\frac{\rho}{\rho_\infty} u^* \left(1 - u^*\right) dz \right)$ is 0.05 cm. The geometrical parameters above are taken from experimental work of Samimy and Elliot [8-9].

Experiment was conducted in tunnel, present calculation performed for planar channel to estimate the behavior of turbulence quantities. Figures 2-4 shows (M_c – 0.51) the comparison of the calculated distributions of longitudinal (axial) mean velocity, variation of the momentum (θ) and vorticity (δ_w) thicknesses, and turbulence quantities with the

experimental data [8-9]. The non-dimensional variables $u^* = \frac{(u-u_0)}{(u_\infty - u_0)}$, $z^* = \frac{(z-z_c)}{\delta_w}$, $\theta = \int_{-\infty}^{+\infty}\left(\frac{\rho}{\rho_\infty}u^*(1-u^*)dz\right)$, $\delta_w = \frac{(u_\infty - u_0)}{(\partial u/\partial z)_{\max}}$ are defined as in the experiments [8-9]. Figure 2 indicates that the shear layer growth in terms of momentum and vorticity thickness is predicted reasonably accurate by the present algorithm, as compared to experimental data.

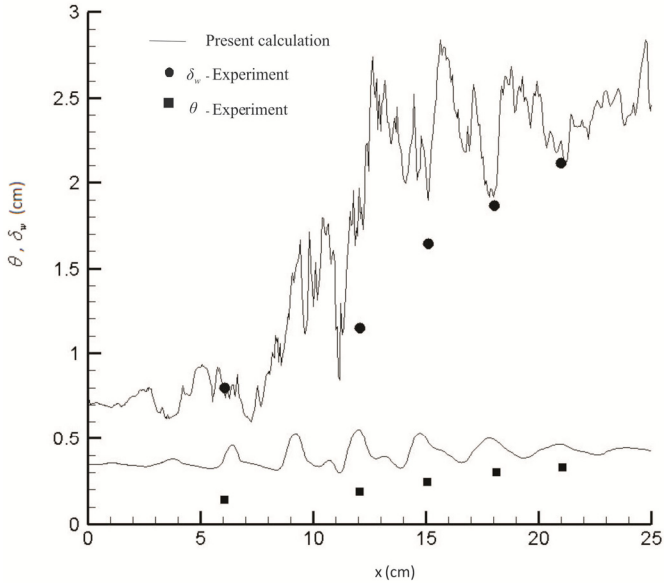

Figure 2 – Comparison of present calculation with experimental data by the growth of momentum and vorticity thickness

The comparison of calculated transverse distribution of the normalized streamwise mean velocity at five longitudinal positions with experimental measurements as shown in Figure 3 suggest that in the fully developed region for x≥12 cm the mean flow is self-similar.

Further comparison of the calculated results with experimental data are shown for the development of the Reynolds stress $-\overline{u'v'}/(u_\infty - u_o)^2$ in Figures 4 and streamwise turbulence intensity $\sqrt{2/3k}/(u_\infty - u_o)$ in Figure 5. The contribution of transverse velocity fluctuating component to turbulent kinetic energy was neglected. It is visible from figures that the calculated turbulence quantities are distorted at x≥15 cm, which shows that the turbulence similarity is achieved further downstream than the mean flow similarity. The preliminary test shown that the mean and turbulence quantities are in a good agreement with experimental data.

In the sequel the shear layer problem has been numerically studied for multi-component gas mixture with the following parameters without chemical reactions and turbulence model: M_0 = 2.3, T_0 = 400 *K*, P_0 = 101320 *Pa*, M_∞ = 4.0, T_∞ = 800 *K*, P_∞ = 101320 *Pa*. The computational grid is 526x201. The non-dimensional channel height and length were 100 and 367, respectively. According to [13-14] it was assumed that there is initial vorticity thickness ($\delta_w = \frac{(u_\infty - u_0)}{(\partial u/\partial z)_{\max}}$) at the inflow, δ_w = 1/15. Figure 6 shows the comparison of mixing layer growth by density a, c and vorticity b, d contours in two physical domain a-b 100x20 and c-d 367x100.

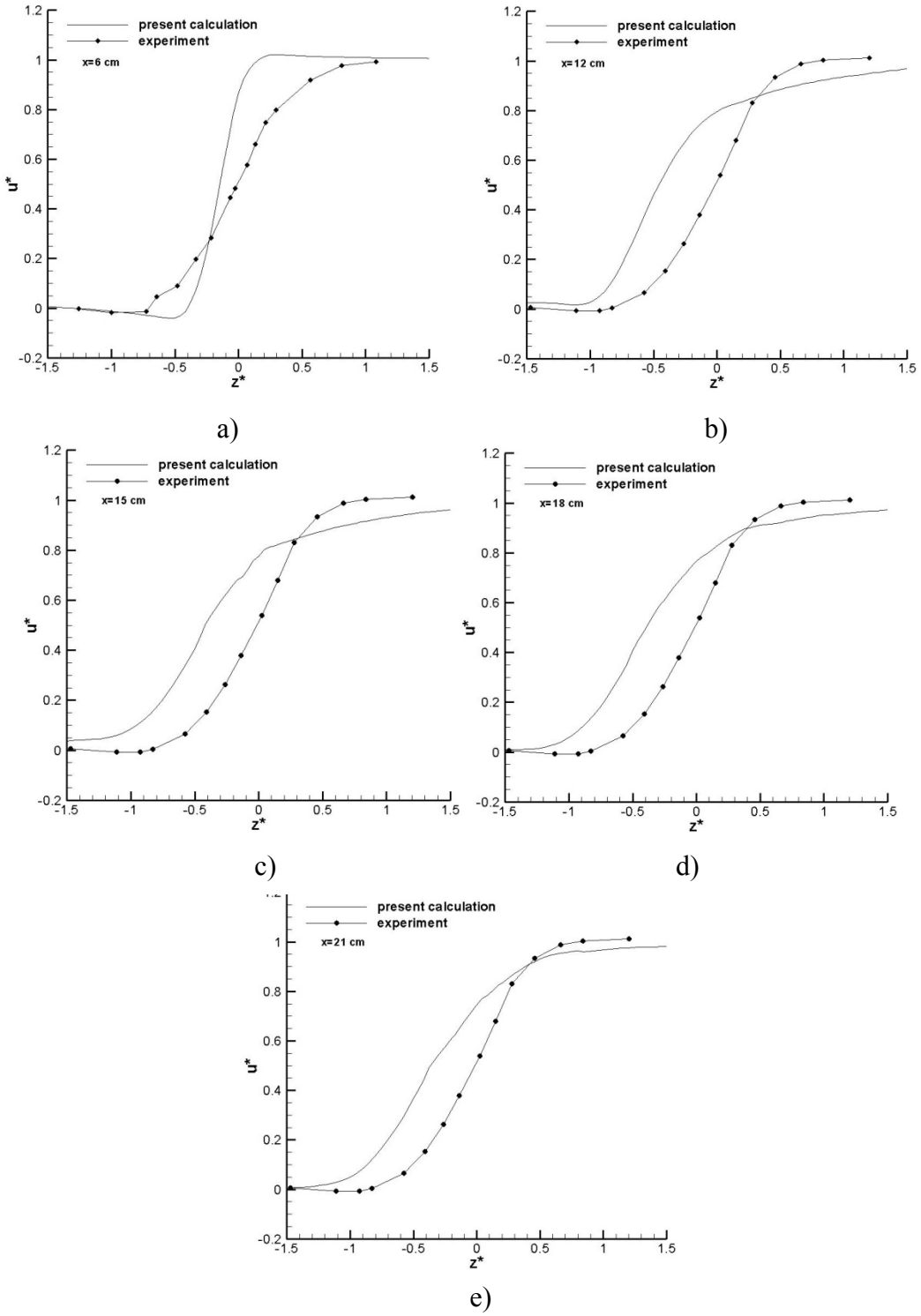

Figure 3 – Comparison of present calculation with experimental data
by longitudinal mean velocity profiles at five longitudinal positions in the shear layer
a) x=6, b) x=12, c) x=15, d) x=18, e) x=21 cm

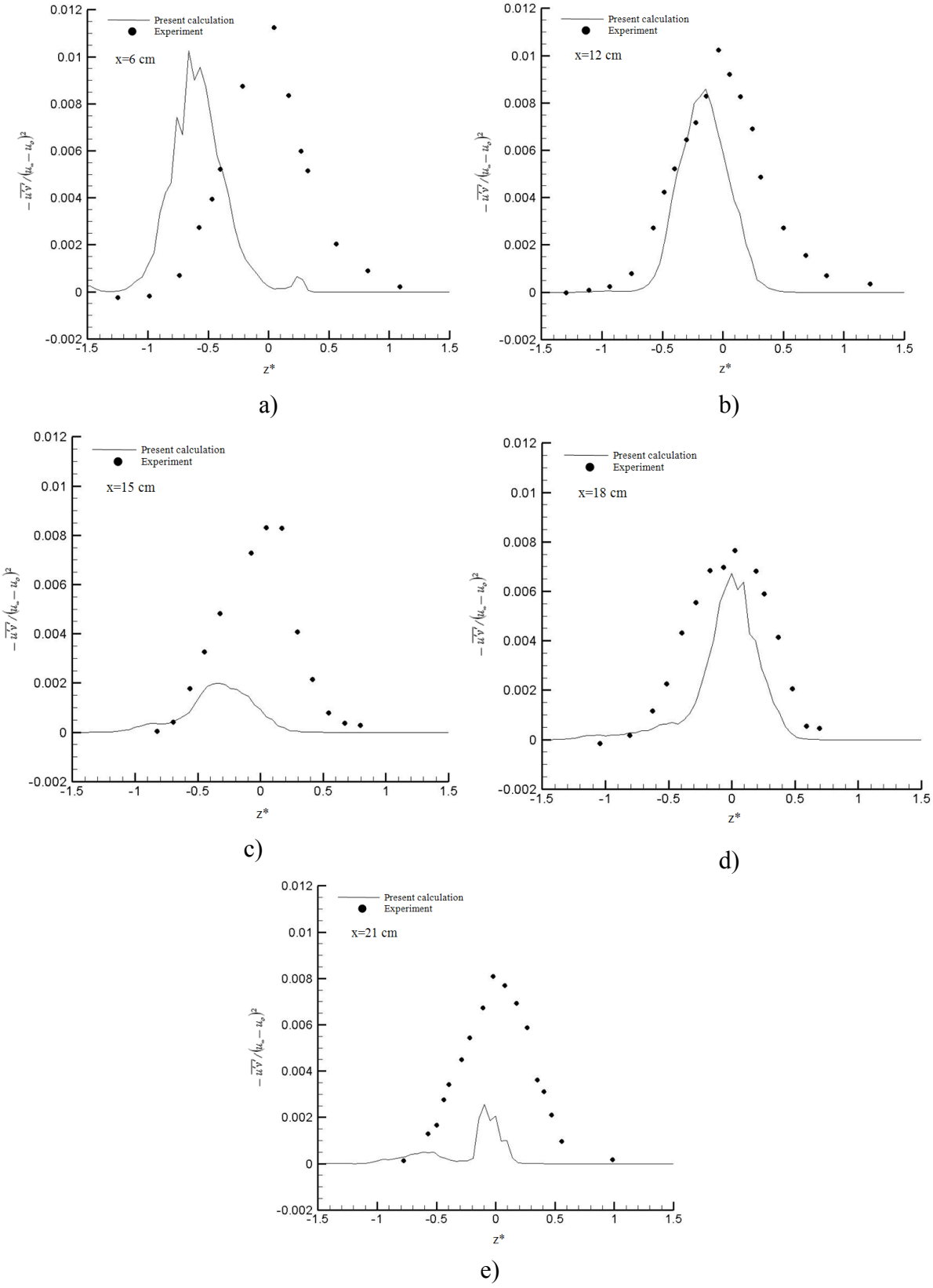

Figure 4 – Comparison of present calculation with experimental data by Reynolds stress at five longitudinal positions in the shear layer a) x=6, b) x=12, c) x=15, d) x=18, e) x=21 cm

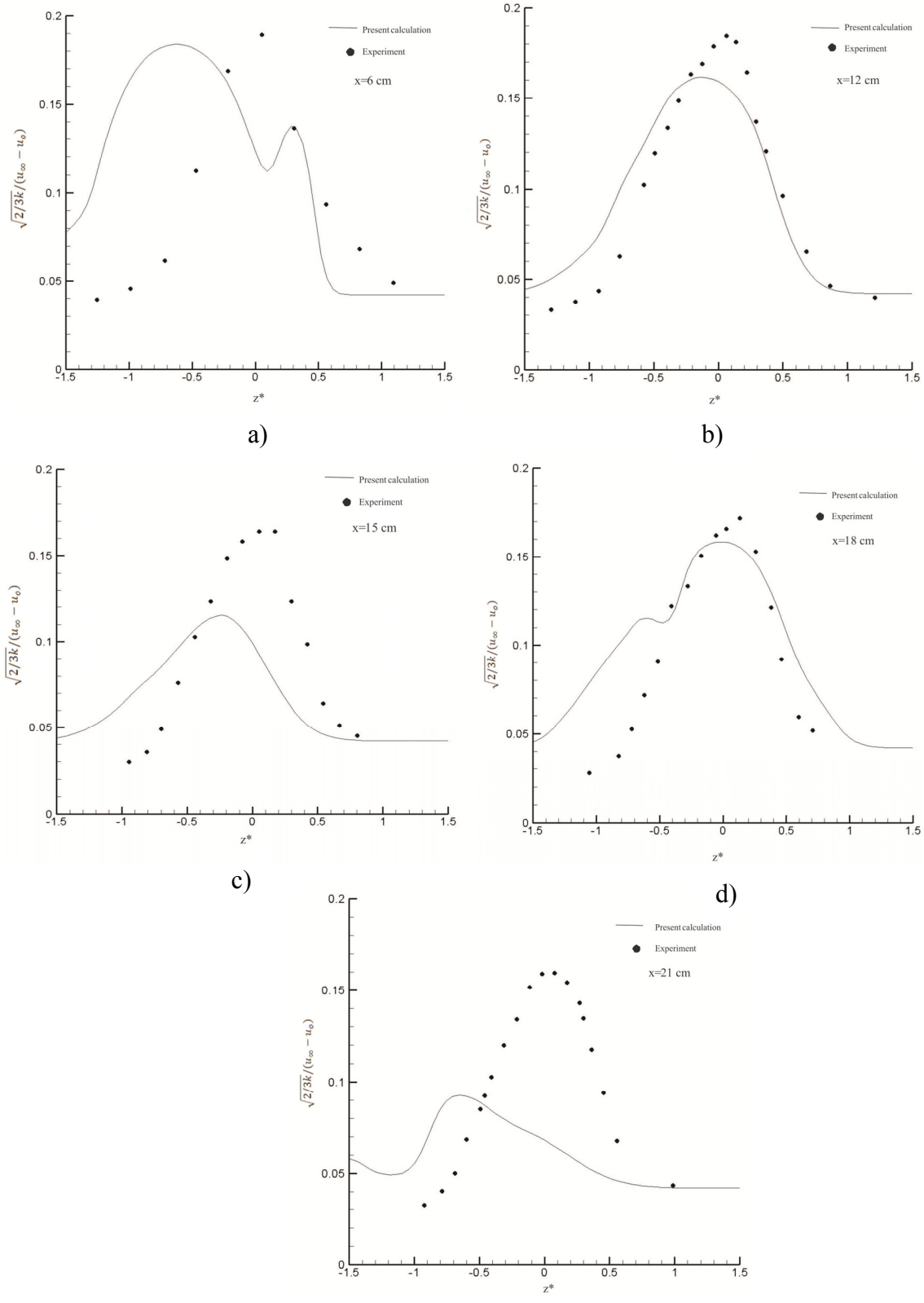

Figure 5 – Comparison of present calculation with experimental data by turbulent intensity at five longitudinal positions in the shear layer a) x=6, b) x=12, c) x=15, d) x=18, e) x=21 cm

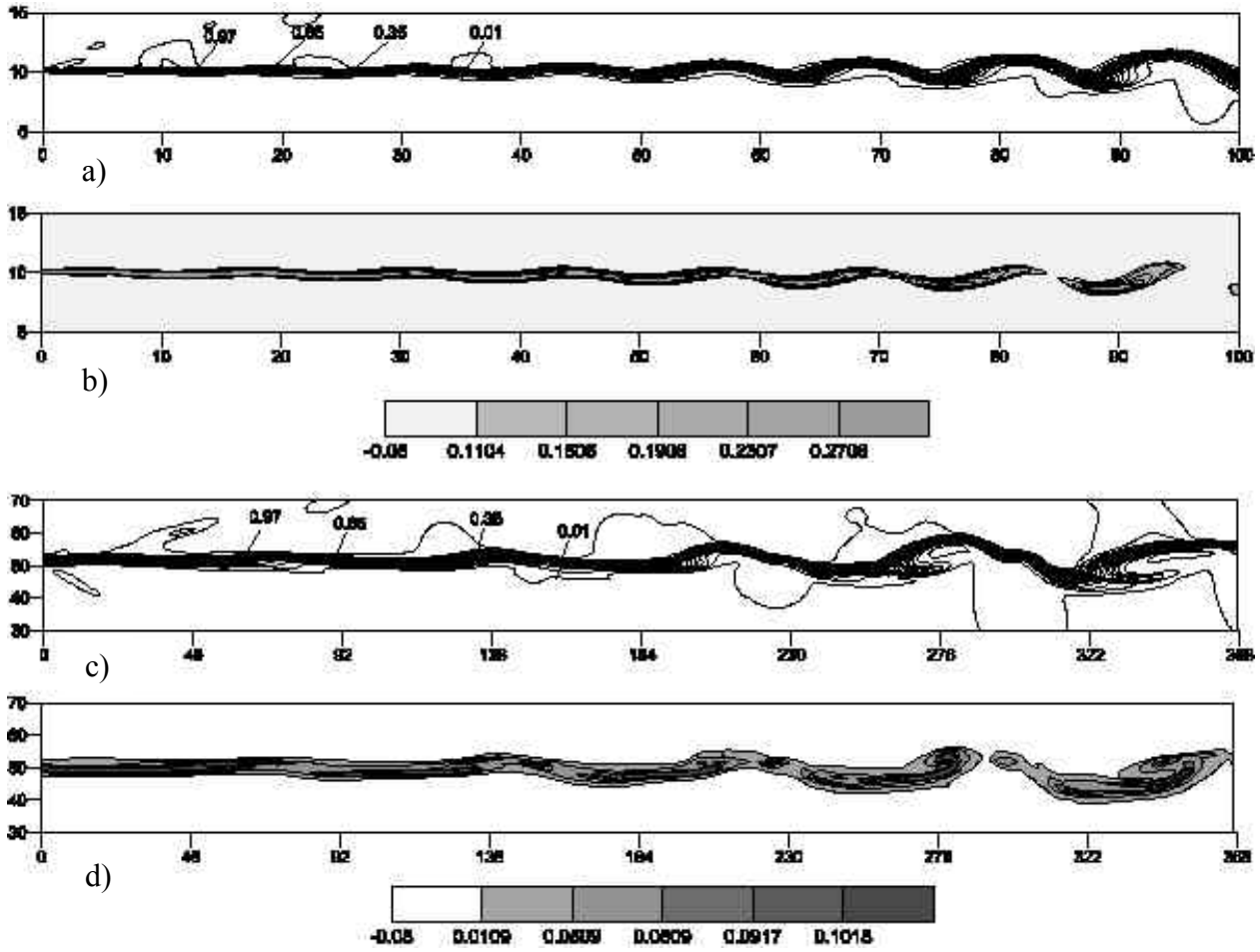

Figure 6 – Comparison of mixing layer growth
by density and vorticity contours in two physicaldomain
a-b) 100x20, c-d) 367x100

It visible from Figure 6 that in c, d the growth of the mixing layer is larger than in a, b. As the supersonic shear layer growth slower than subsonic, so to the formation of vortical structures and its growth in supersonic shear layer need longer domain (Figure 6-c-d). Figure 7 shows the comparison of vorticity contours obtained by present calculation and by authors [13-14]. In [13-14] studied the growth of instabilities in monatomic (air) gas flows, while in the present study considered the mixing layer growth in multi-component gas mixture. Present results indicate that in the case of multi-component gas the vortical structure has a growing character as it is shown in Figure 7-b.

Also, this example show the advantage of using high order ENO scheme in modeling of mixing process, formation and growing of vortical structures.

Combustion results

The free shear layer of hydrogen-air turbulent flows mixing and combustion are numerically studied. The simulations are performed in a rectangular domain of 4 cm in stream-wise direction and 1.5 cm in transverse direction. The splitter plate thickness is 0.1 cm, and at the trailing edge is 0.0045 cm. At the inflow plane, hydrogen enters from the lower half and air enters from the upper half. A 401x151 grid with stretching at the entrance and mixing layer was used. The hydrogen flow parameters are $M_0 = 1.4$ ($M_0 = 1.1$), $T_0 = 400$ K, $P_0 = 101320$ Pa, and air flow parameters are $M_\infty = 1.8$ ($M_\infty = 1.5$), $T_\infty = 1300$ K, $P_\infty = 101320$ Pa.

The Figure 8-a, c, d, f ($M_0 = 1.4$, $M_\infty = 1.8$) are illustrated the comparison of temperature fields

without and with chemical reactions for moments t=5.35 mks (Figure 8-a-c) and t =10.6 mks (Figure 8-d-f). The temperature for both cases is equal to 0.97 (1261 K) at t=5.35 mks. From figure follows mixing layer growth lead to an increase in the temperature and mixing intensity of fuel and oxidizer. It is evident from Figure 8-a, c the difference between results are negligible, consequently at the ignition stage the chemical reactions passes without significant heat generation. At the moment t=10.6 mks the temperature of the mixture increase till 1.1 (T=1430 K) due to chemical reaction, while in the non-reacting case the mixture temperature is 0.97.

For the description of reaction pathways of hydrogen, a seven species chemical reaction model by Jachimowski (see table 1 [31]) is taken.

The water vapor H_2O formation for the chemical reaction case at the ignition moment t=5.35 mks (Figure 8-b) and at the moment t=10.6 mks (Figure 8-e) are also illustrated.

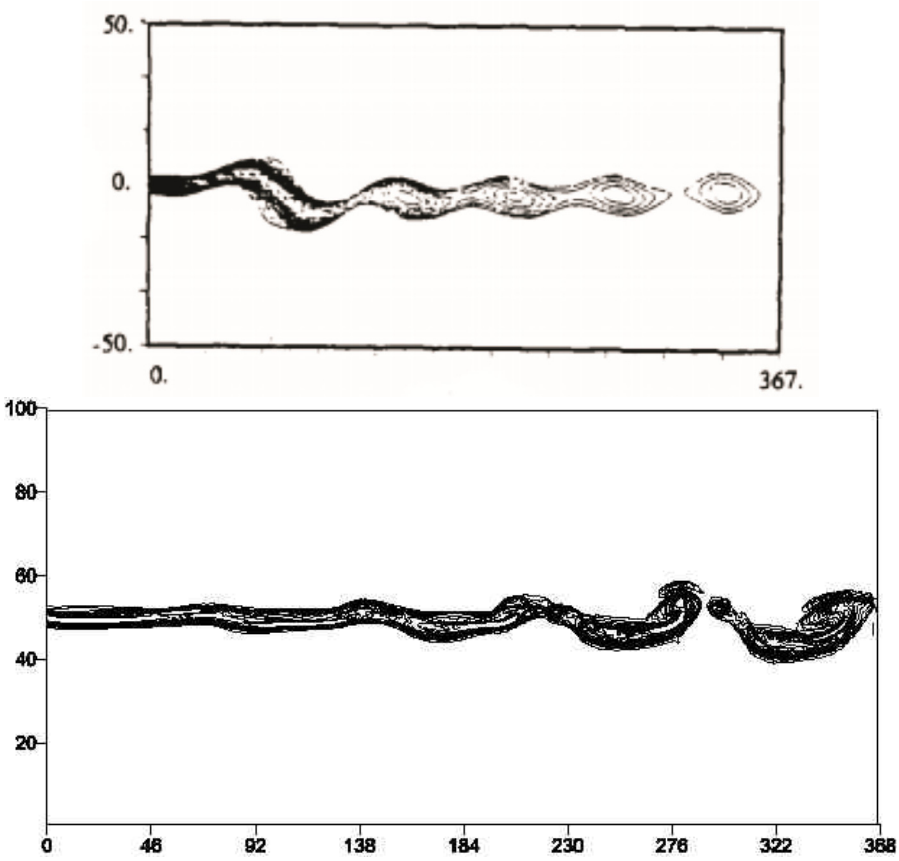

Figure 7 – Comparison of present calculation with numerical results [13-14] by vorticity contours
a) numerical results [13-14], b) present calculation

Table 1 – Jachimowski's reaction mechanism

Reaction number	Reaction	A_k (m^3/mole·s)	β_k	E_k/R
1	$H_2 + O_2 = OH + OH$	0.170E +14	0.0	24233
2	$H + O_2 = OH + O$	0.142E +15	0.0	8254
3	$OH + H_2 = H_2O + H$	0.316E +08	1.8	1525
4	$O + H_2 = OH + H$	0.207E +15	0.0	6920
5	$OH + OH = H_2O + O$	0.550E +14	0.0	3523
6	$H + OH + M = H_2O + M$	0.221E +23	-2.0	0
7	$H + H + M = H_2 + M$	0.653E +18	-1.0	0

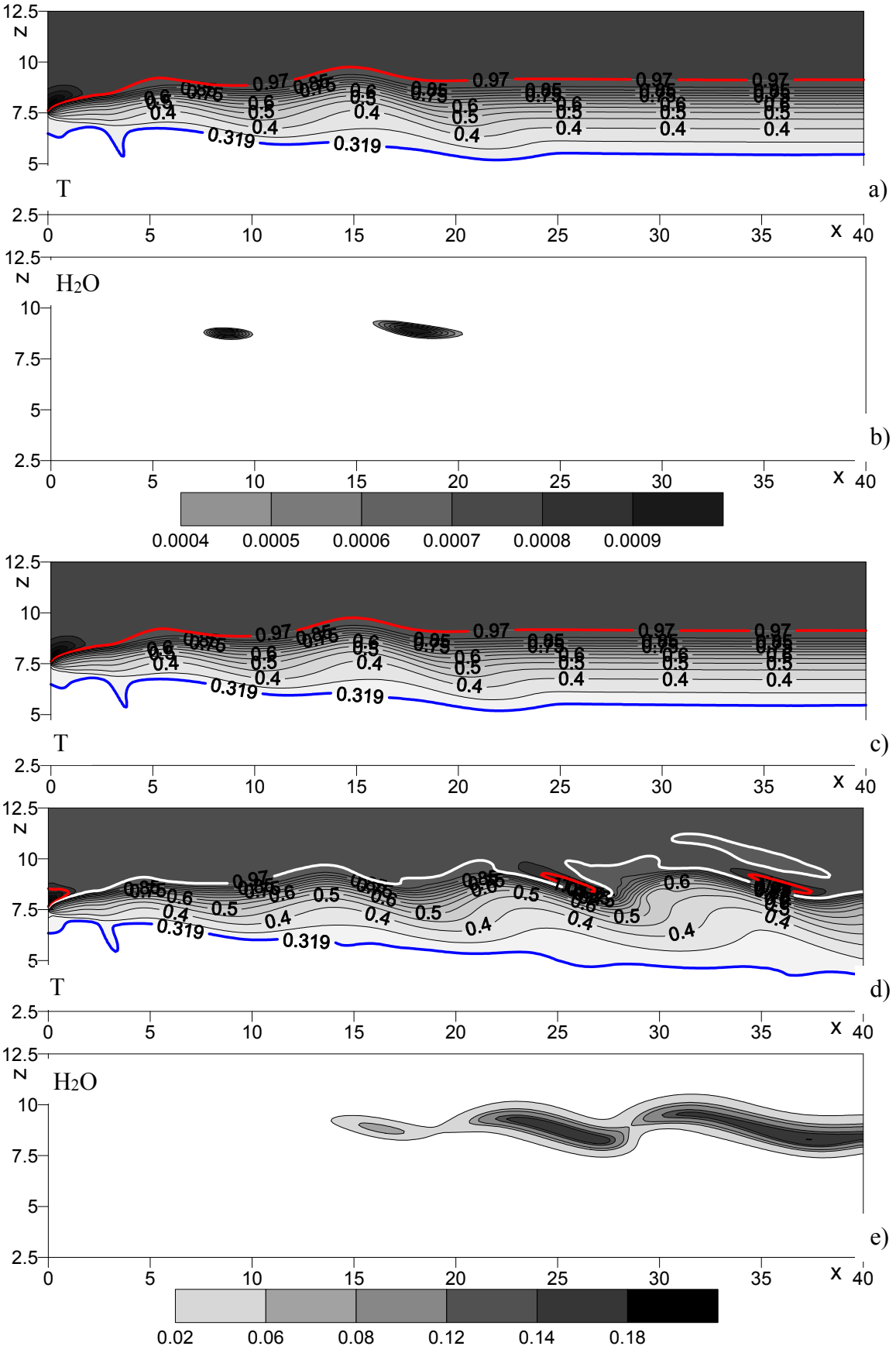
z
x
T
a)
H2O
b)
0.0004 0.0005 0.0006 0.0007 0.0008 0.0009
T
c)
T
d)
H2O
e)
0.02 0.06 0.08 0.12 0.14 0.18

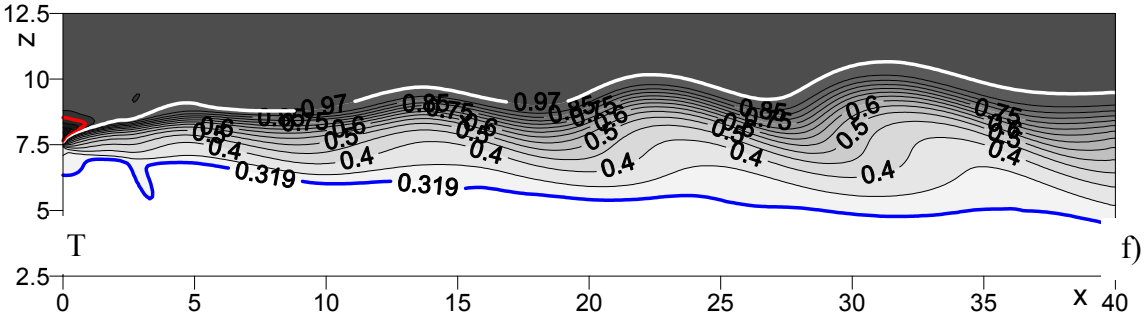

Figure 8 – The temperature field with a, c) and without b, d) chemical reactions
a-b) t=5.35, c-d) t=10.6 mks

Figure 9 shows the mass concentration contours of oxidant (Figure 9-a-b) and hydrogen (Figure 9-c-d) with combustion (Figure 9-b, d) and without it (Figure 9-a, c) at the moment t=10.6 mks. As can be seen from the figure as a result of combustion the oxidant O_2 field change significantly (Figure 9-b), while the hydrogen H_2 changes little (Figure 9-d). The isolines of the formation of combustion products such as water vapor (H_2O), hydroxyl radical (OH), hydrogen atom (H) and oxygen atom (O) concentrations and vorticity contours at various times are presented in Figures 10-13.

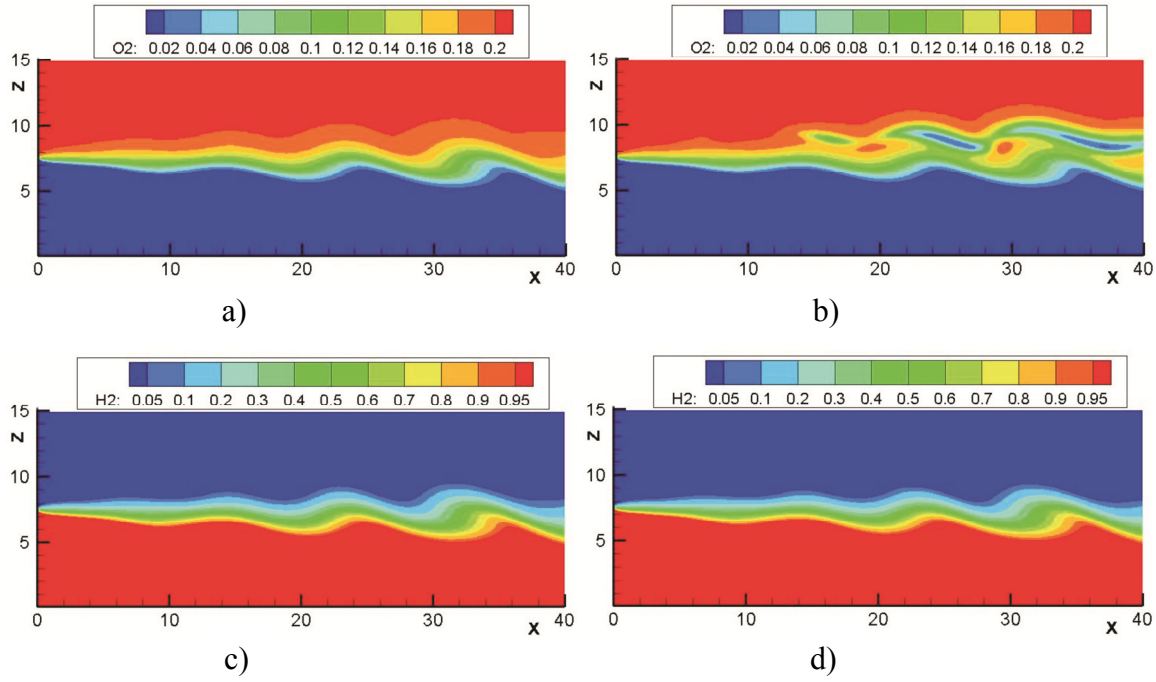

Figure 9 – Mass concentration contours of O_2 a-b) and H_2 c-d)

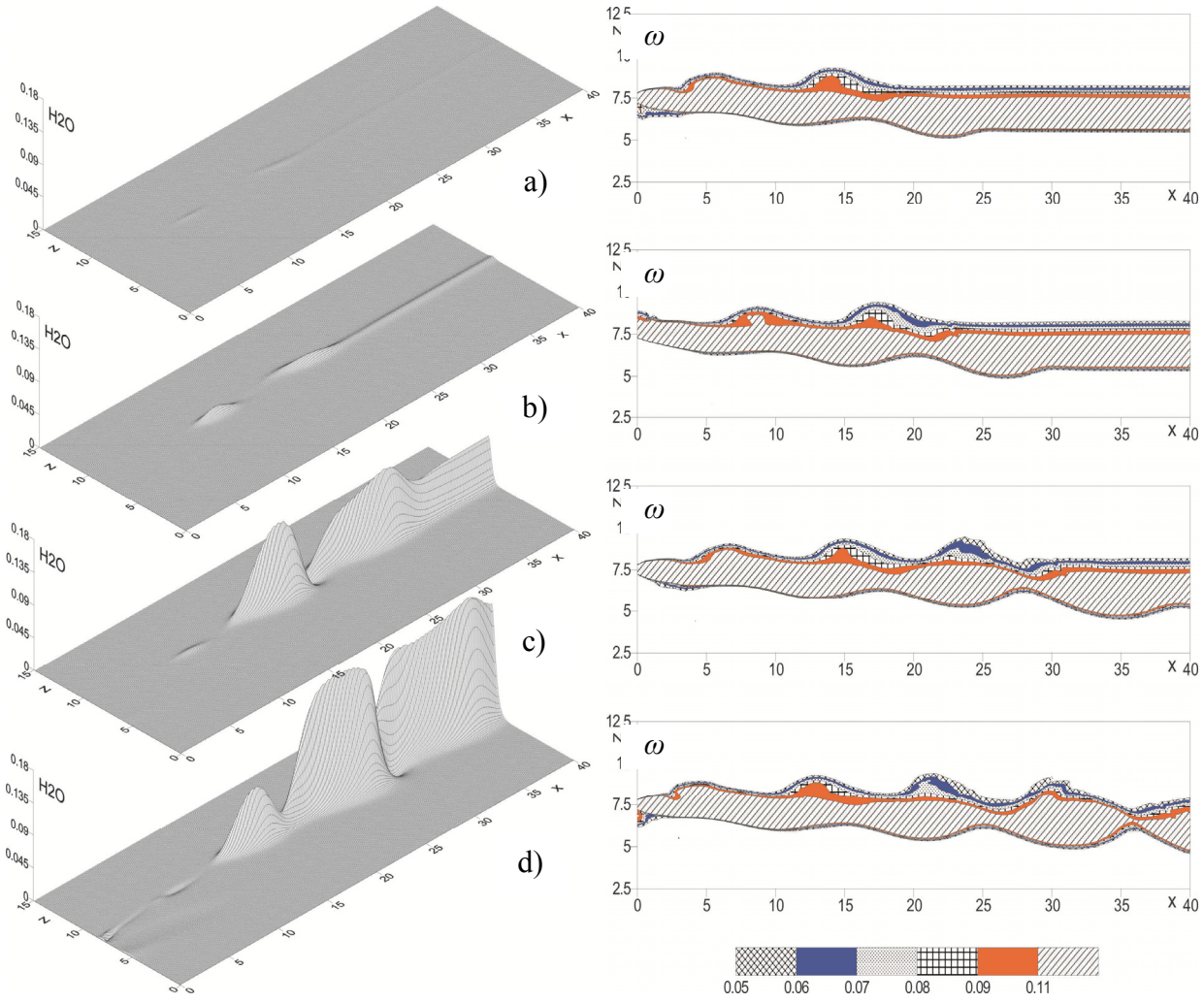

Figure 10 – The dynamic of water vapor concentration formation and vorticity contours at four times
a) t=5.35, b) t=6.4, c) t=8.5, d) t=10.6 mks

It is visible (Figure 10-a), initially combustion product H_2O is concentrated in the thin mixing layer at the moment t=5.35 mks. In this time the maximum of water vapor is of the order 10^{-4}, Figure 10-a. From the period of time t=5.35 up to t=6.4 mks (Figure 10-b) this value growth up to 10^{-3}. Obviously, it is the induction period which is period of accumulation of radicals and active centers, where there is also growth reaction rate.

The vorticity contours formed in the shear layer are illustrated in Figure 10-a-d (right, ω). In process of time the separation of vortical structure occurs Figure 10-b-d, thus with increasing of vorticity formation intensity (Figure 10-b-d, right) the separation of combustion zone concentrated in the upper region of vortices (Figure 10-b-d, left). The same behavior has products OH, H and O as it is illustrated in Figures 11-13-b-d, right with different induction period of formation. For example, the water vapor H_2O (Figure 10-a, left) and oxygen atom O (Figure 13-a) are formed earlier at t=5.35 mks than hydroxyl radical OH at t=5.7 mks (Figure 11-a) and hydrogen atom H at t=6.75 mks (Figure 12-a).

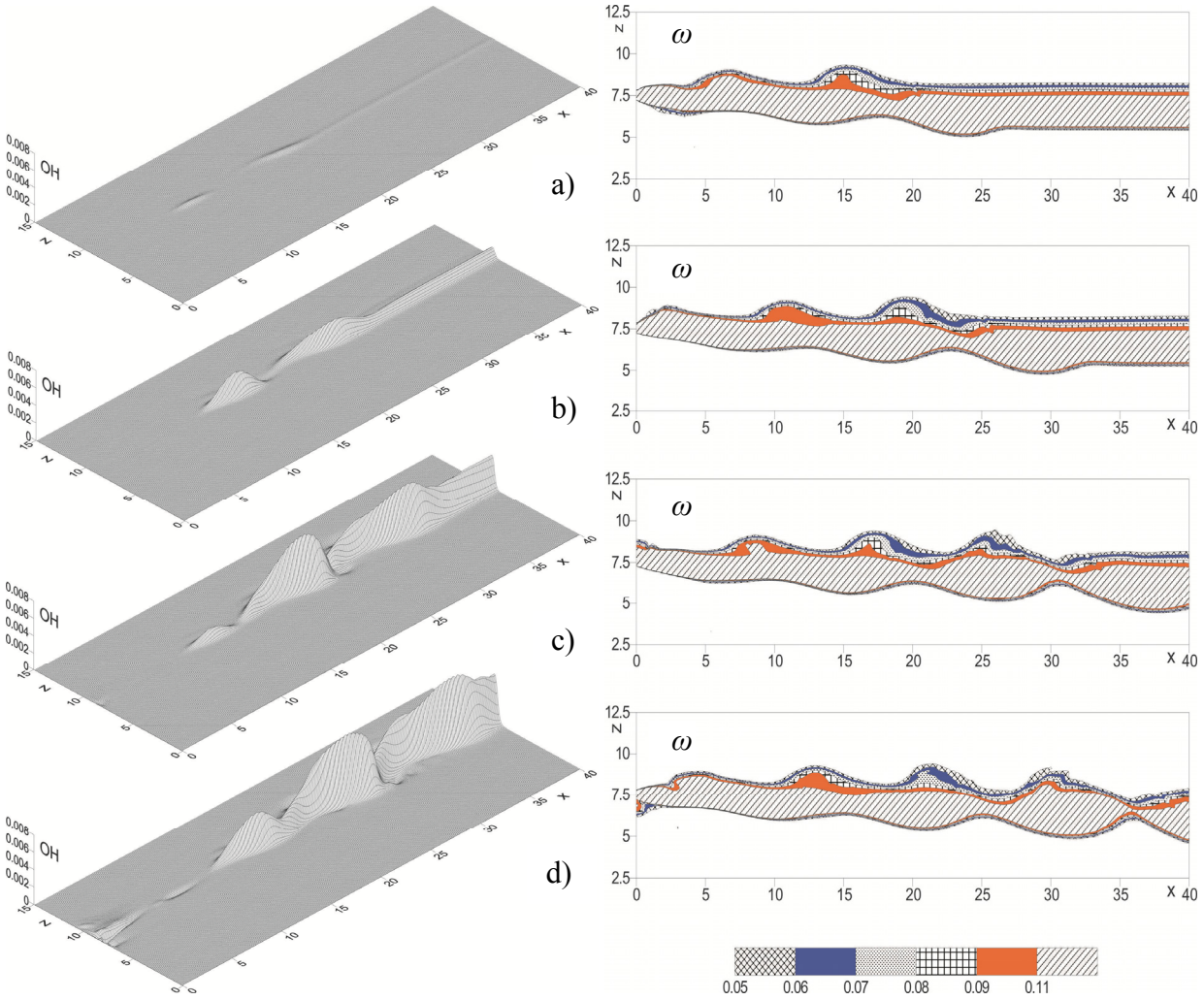

Figure 11 – The dynamic of hydroxyl radical concentration formation and vorticity contours at four times
a) t=5.7, b) t=7.1, c) t=9.2, d) t=10.6 mks

Numerical calculations performed with lower values of Mach numbers $M_0 = 1.1$, $M_\infty = 1.5$ are showed the presence of subsonic zones, which are visible from iso-Mach line contours in Figure 14-a. The minimum value of Mach number for $M_0 = 1.1$, $M_\infty = 1.5$ is 0.8, while for $M_0 = 1.4$, $M_\infty = 1.8$ this value is equal to 1.0. However, comparing with the higher Mach number case Figure 14-d the presence of subsonic zones does not have appreciable influence on the qualitative picture of combustion zone (Figure 14-c, f). Although, quantitatively this difference is more visible. For example, the maximum of water vapor and temperature are 0.16 and 1.1 (1430 K) for the case $M_0 = 1.4$, $M_\infty = 1.8$ whereas for other case maximum H2O is equal to 0.19 and temperature is 1.18 (T=1534 K). Therefore the occurrence of subsonic zones has insignificantly affects on combustion zone, whereas that the crucial aspect is the presence of vortical structures. The determinative factor in combustion stabilization and efficiency is the formation of vortices and their growth.

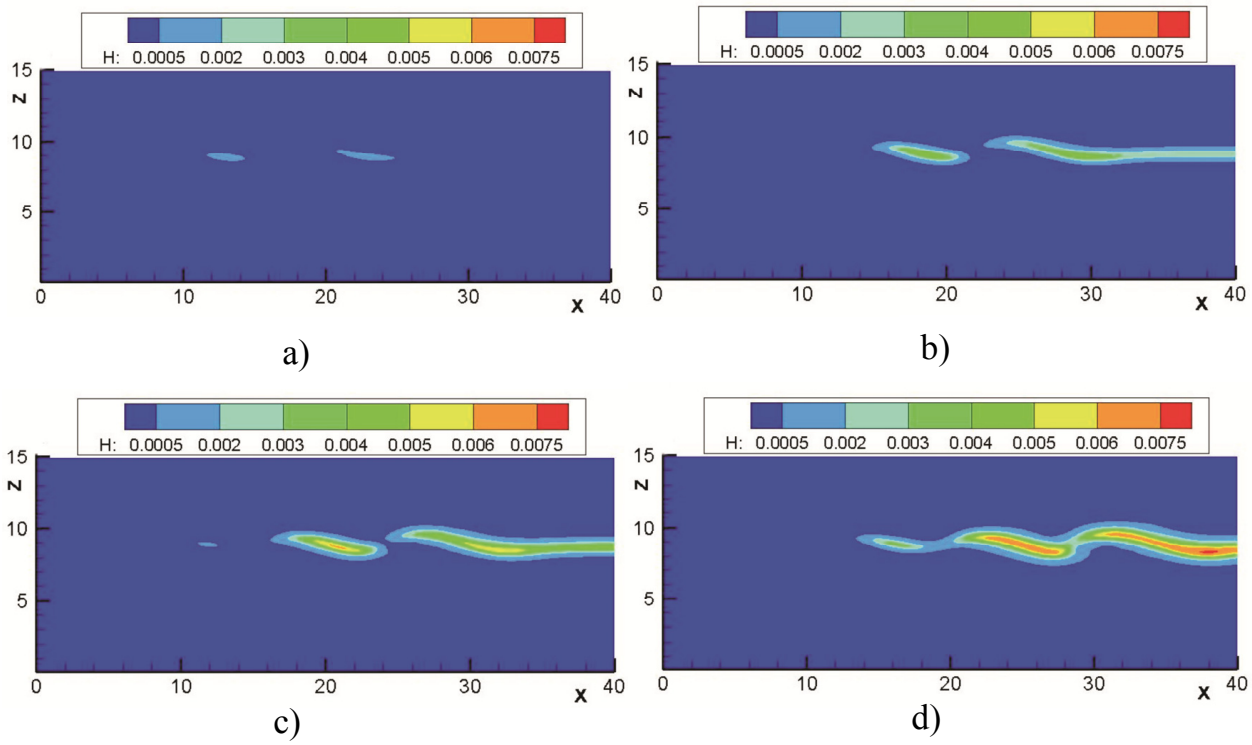

Figure 12 – The dynamic of hydrogen atom concentration formation at four times
a) t=6.75, b) t=8.5, c) t=9.2, d) t=10.6 mks

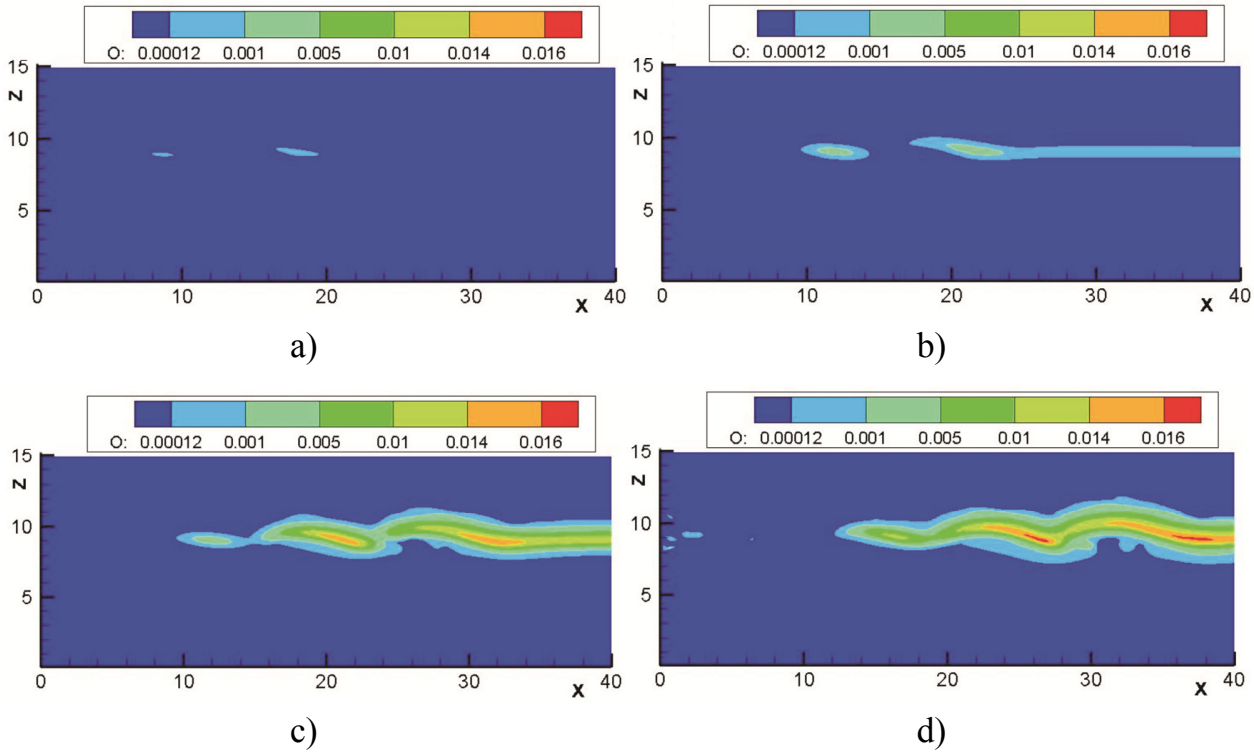

Figure 13 – The dynamic of hydrogen atom concentration formation at four times
a) t=5.35, b) t=6.4, c) t=9.2, d) t=10.6 mks

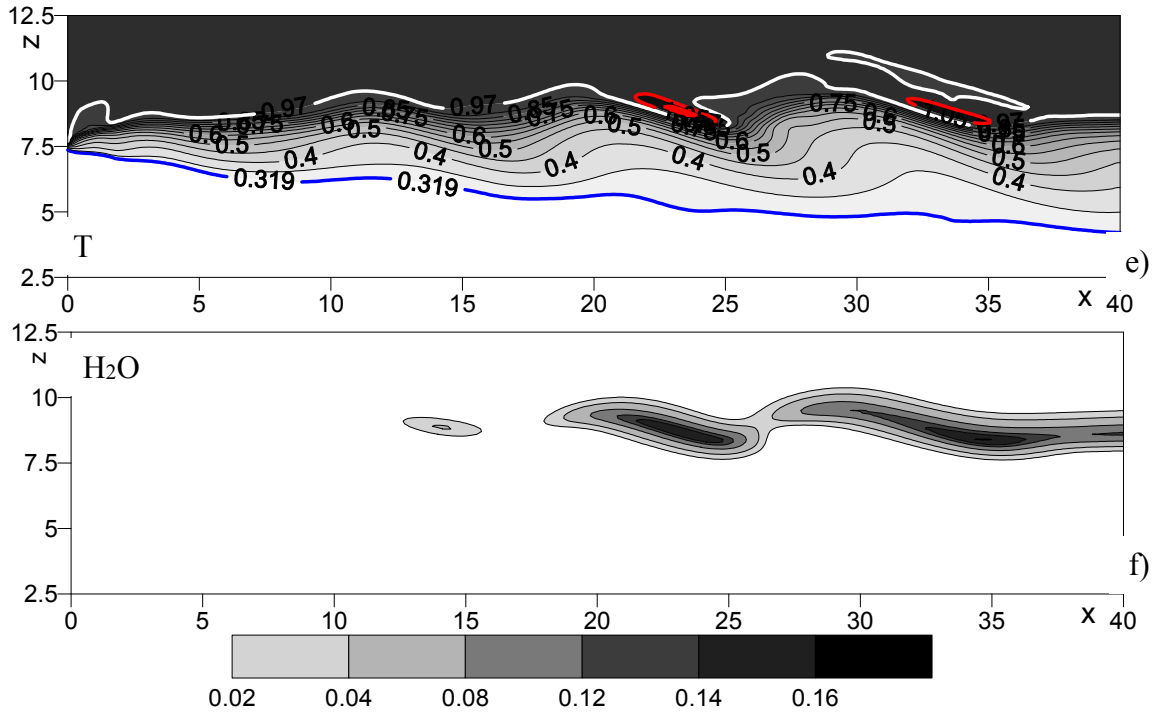

Figure 14 – The distribution of iso-Mach a, d), hydrogen b, e) and water vapor concentration c, f) contours
a-c) $M_0 = 1.1$, $M_\infty = 1.5$
d-f) $M_0 = 1.4$, $M_\infty = 1.8$

It should be noted the process of ignition represented in the Figure 15 are different for given cases. From isolines of water vapor concentration H_2O Figure 15-b, d are visible the ignition delay time is t=1.25 mks for result with smaller parameter, while for large Mach numbers are t=5.35 mks. The temperature in the ignition region for both cases Figure 15-a, c is equal to 0.97 (1261 K). As a identifier of the given mixture ignition it was taken the main product – water vapor H_2O with the value approximately 0.2 percent of initial oxidant fracture.

The combustion efficiency can be estimated from the overall chemical reaction of hydrogen oxidation. It appears from this reaction that for the 0.004 kg/mole hydrogen completely oxidation it is need 0.032 kg/mole oxygen. As a parameter characterized complete combustion it is taken the relation of the mass flow rates Q_{O2}/Q_{H2}, where $Q_{O2} = \int \rho_{O2} u_\infty dz$ and $Q_{H2} = \int \rho_{H2} u_0 dz$. This relation should be $Q_{O2}/Q_{H2} \geqslant 8$ to complete hydrogen combustion. Numerical experiment revealed that for the $M_0 = 1.4$, $M_\infty = 1.8$ at the exit plane x=4 cm this relation is equal to 18.7, which is pointing out that the hydrogen completely oxidize. The initial mass flow rates ratio at the entrance for this case $Q_{O2}/Q_{H2} = 14.8$, which indicate on the poor mixture. For Mach numbers $M_0 = 1.1$, $M_\infty = 1.5$ the initial mass flow rates ratio $Q_{O2}/Q_{H2} = 15.6$. At the exit plane x=4 cm combustion efficiency parameter is equal to 19.8. This comparison has been confirmed that subsonic zones have not strong affect on increasing the total residence time of fuel (hydrogen) in the combustion chamber. So the presence of isolated vortices and their growth downstream provides a better mixing of fuel, air and hot combustion products, which greatly stabilizes the combustion process.

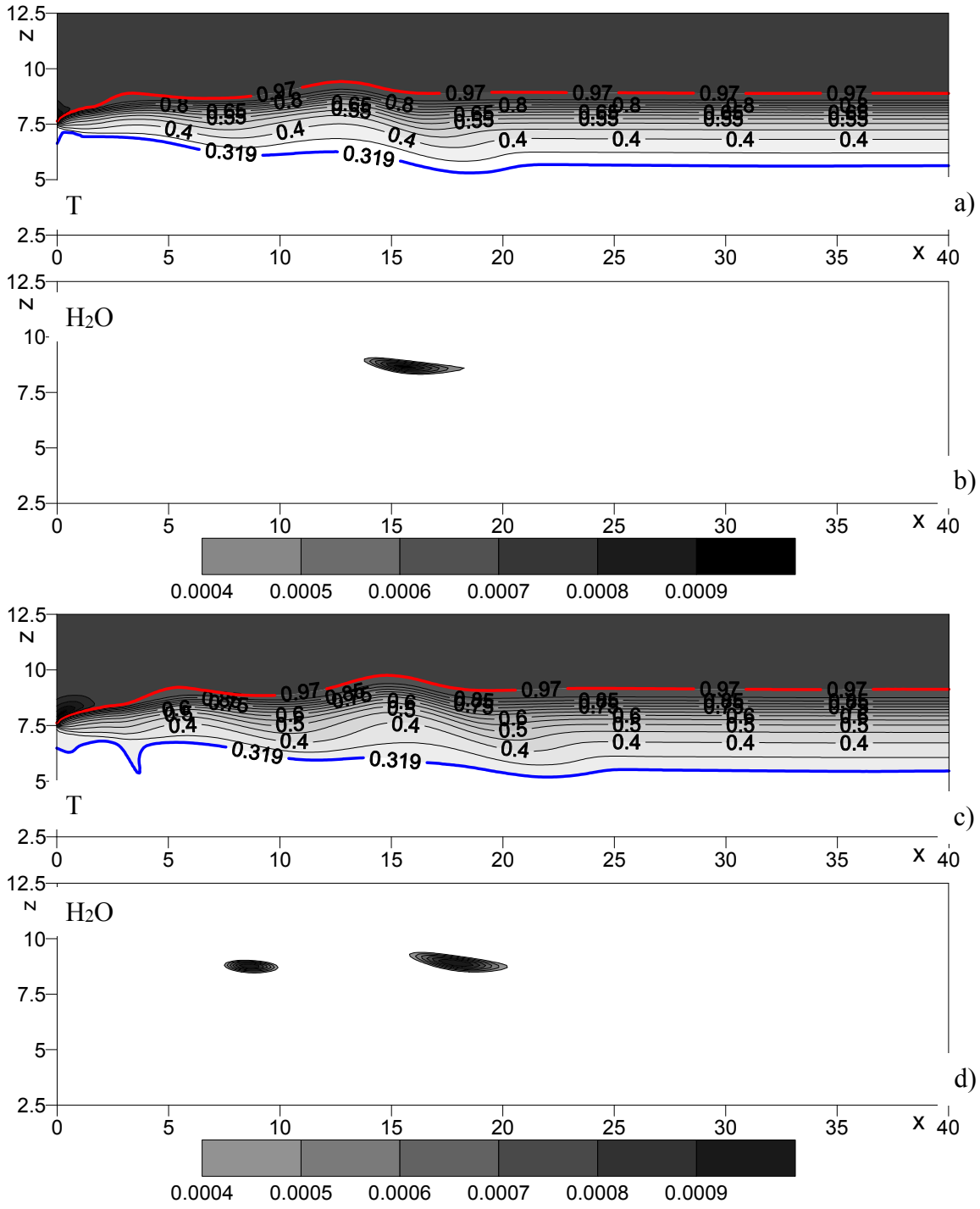

Figure 15 – The temperature field a, c) and formation of water vapor b, d) a-b) $M_0 = 1.1$, $M_\infty = 1.5$, c-d) $M_0 = 1.4$, $M_\infty = 1.8$

Conclusion

The flowfield structures of supersonic turbulent planar shear layer and combustion computed by calculation of the system of two-dimensional planar Favre-averaged Navier-Stokes equations. The k-ε two-equation turbulence model with compressibility correction is used to determine the eddy viscosity coefficient. The numerical method is based on the third order ENO finite-difference scheme. The

comparison of present results obtained by using ENO scheme and k-ε turbulence model with experimental data demonstrates a satisfactory prediction of mean and turbulence properties of the flow. The numerical results of hydrogen-air mixture combustion based on Jachimowski's seven-species seven reaction model.

The calculation reacting shear layer revealed distribution and enhancement of hydrogen-air mixing and combustion is strongly depend on vortices formation, a namely their intensity and growing. The present numerical experiments show that the combustion zone is concentrated in the upper (oxidizer) boundary of mixing layer.

It have been graphically illustrated that for the lower Mach numbers case the hydrogen-air mixture ignition is occurred faster than for the higher one.

Thus the constructed algorithm based on the high order scheme and computer code for turbulent supersonic reacting flow allows to study influence parameters that control mixing and combustion, which is important in the design of supersonic combustion ramjet (scramjet) engines and easily expanded into 3D case.

References

1. Winant C.D., Browand F.K. “Vortex pairing: the mechanism of turbulent mixing-layer growth at moderate Reynolds number.” *J. Fluid Mech*. 63 (1974): 237-255.

2. Brown G.L., Roshko A. “On the density effects and large structures in turbulent mixing layers.” *J. Fluid Mech.* 64 (1974): 775-816.

3. Bogdanoff D.W. “Compressibility effects in turbulent shear layers.” *AIAA J*. 21 (1983.): 926-927.

4. Papamoschou D., Roshko A. “The compressible turbulent shear layer: an experimental study.” *J. Fluid Mech*. 197 (1988): 453-477.

5. Chinzei N., Masuya G., Komuro T., Murakami A., Kudou K. “Spreading of two-stream supersonic turbulent mixing layers.” *Phys. Fluids* 29 (1986): 1345-1347.

6. Goebel S. G., Dutton J.C. “Experimental study of compressible turbulent mixing layers.” *AIAA J.* 29, no. 4 (1991): 538-546.

7. Oster D., Wygnanski I. “The forced mixing layer between parallel streams”. *J. Fluid Mech.* 123 (1982): 91-130.

8. Samimy M., Elliot G.S. “Effects of compressibility on the characteristics of free shear layers.” *AIAA J.* 28 (1990): 439-445.

9. Elliot G.S., Samimy M. “Compressibility effects in free shear layers.” *Phys. Fluids A 2* (1990): 1231-1240.

10. Ju Y., Niioka T. “Ignition Analysis of Unpremixed Reactants with Chain Mechanism in a Supersonic Mixing Layer.” *AIAA J.* 31, no. 5 (1993): 863-868.

11. Im H. G., Chao B. H., Bechtold J. K., Law C. K. “Analysis of Thermal Ignition in the Supersonic Mixing Layer.” *AIAA J.* 32, no. 2 (1994): 341-349.

12. Cheng T.S., Lee K.S. “Numerical simulations of underexpanded supersonic jet and free shear layer using WENO schemes.” *International Journal of Heat and Fluid Flow* 26 (2005): 755-770.

13. Tang W., Komerath N.M., Sankar L.N. “Numerical simulation of the Growth of instabilities in Supersonic Free Shear Layers.” *J. Propulsion* 6, no. 4 (1990): 455-460.

14. Tang W., Sankar, L.N., Komerath, N. “Mixing enhancement in supersonic free shear layers.” AIAA 2nd Shear Flow Conference, *AIAA J.* (1989): 89-98.

15. Reichert R.S., Biringen S. “Numerical simulation of compressible plane jets.” *Mechanics Research Communications* 34 (2007): 249-259.

16. Dale A. Hudson *Numerical simulation of a confined supersonic shear layer*. PhD dissertation, (1996): 1-181.

17. Xiao-Tian Shi, Jun Chen, Wei-Tao Bi, Chi-Wang Shu, Zhen-Su She. “Numerical simulations of compressible mixing layers with a discontinuous Galerkin method.” *Acta Mech. Sin.* 27, no.3 (2011): 318-329.

18. Zambon A.C., Sriram A.T., Chelliah H.K. “Development and Implementation of Explicit Reduced Reaction Models in Supersonic Reacting Shear Flow Simulations.” 45th AIAA Aerospace Sciences Meeting and Exhibit, Reno, Nevada, *AIAA-2007* (2007): 772.

19. Sriram A.T., Zambon A.C., Chelliah H.K. “Validation of Ethylene-Air Reduced Reaction Models in Supersonic Shear Flows.” 46th AIAA Aerospace Sciences Meeting and Exhibit, Reno, Nevada, *AIAA-2008* (2008): 993.

20. Da Silva L. F. F., Deshaies B., Champion M. “Some Specific Aspects of Combustion in Supersonic H2-Air Laminar Mixing Layers.” *Combustion Science and Technology 89* (1993): 317-333.

21. Nishioka M., Law C.K. “A Numerical Study of Ignition in the Supersonic Hydrogen/Air Laminar

Mixing Layer." *Combustion and Flame* 108 (1997): 199-219.

22. Fang X., Liu F., Sirignano W. A. "Ignition and Flame Studies for an Accelerating Transonic Mixing Layer." *Journal of Propulsion and Power* 17, no. 5 (2001): 1058-1066.

23. Ju Y., Niioka T. "Reduced Kinetic Mechanism of Ignition for Nonpremixed Hydrogen/Air in a Supersonic Mixing Layer." *Combustion and Flame* 99 (1994): 240-246.

24. Ju Y., Niioka T. "Ignition Simulation of Methane/Hydrogen Mixtures in a Supersonic Mixing Layers." *Combustion and Flame* 102 (1995): 462-470.

25. Tahsini, A.M. "Ignition Analysis in Supersonic Turbulent Mixing Layer." *World Academy of Science, Engineering and Technology* 57 (2011): 353-357.

26. Tahsini A.M. "Ignition Time Delay in Swirling Supersonic Flow Combustion." *World Academy of Science, Engineering and Technology* 70 (2012): 623-627.

27. Chakraboty D., Paul P. J., Mukunda H. S. "Evaluation of Combustion Models for High Speed H2/Air Confined Mixing Layer Using DNS Data." *Combustion and Flame* 121 (2000): 195-209.

28. Kee R. J., Rupley F. M., Miller J. A. "CHEMKIN-II: a Fortran chemical kinetic package for the analysis of gas-phase chemical kinetics." *SANDIA Report SAND89-8009* (1989).

29. Poinsot T.J., Lele S.K. "Boundary conditions for direct simulation of compressible viscous flows." *Journal of Computational Physics* no. 101 (1992): 104-129.

30. Harten A., Osher S., Engquist B., Chakravarthy S.R. "Some Results on Uniformly High-Order Accurate Essentially Non-oscillatory Schemes." *Applied Num. Math*. 2 (1986): 347-377.

31. Yang J. Y. "Third order nonoscillatory schemes for the Euler equations." *AIAA J.* 29, no. 10 (1991): 1611-1618.

32. Bruel P., Naimanova A. Zh. "Computation of the normal injection of a hydrogen jet into a supersonic air flow." *Thermophysics and Aeromechanics* 17, no. 4 (2010): 531-542.

33. Belyayev Ye., Naimanova A. Zh.. "Two-Dimensional Supersonic Flow with Perpendicular Injection of the Gas." *Chapter 2 InTech open access book Advanced Methods for Practical Applications in Fluid Mechanics* (2012): 23-44.

34. Shuen J. Sh., Yoon S. "Numerical study of chemical reacting flows using a lower-upper symmetric successive overrelaxation scheme." *AIAA J.* 27, no. 12 (1989): 1752-1760.

35. Belyayev Ye., Kaltayev A., Naimanova A. Zh. "Supersonic Flow with Perpendicular Injection of a Hydrogen." Proceedings of 2010 2nd International Conference on Computer Engineering and Technology, *Mechanical and Aerospace Engineering* 5(2010): 531-534.

36. Cao D.G., He G.Q., Qin F., Wei X.G., Shi L., Liu B., Huang ZW. "LES study on flow features of the supersonic mixing layer affected by shock waves." *International communications in heat and mass transfer* 85 (2017): 114-123.

IRSTI 27.29.23

[1,3]M.K. Dauylbayev, [2]M. Akhmet, [4,*]A.E. Mirzakulova, [1,3]A.B. Uaissov

[1]al-Farabi Kazakh National University, Almaty, Kazakhstan
[2]Middle East Technical University, Ankara, Turkey
[3]Institute of Mathematics and Mathematical Modeling, Almaty, Kazakhstan
[4]Abay Kazakh National Pedagogical University, Almaty, Kazakhstan
[*]e-mail: aziza.mirzakulova@mail.ru

Asymptotic convergence of the solution of the initial value problem for singularly perturbed higher-order integro-differential equation

Abstract. The article is devoted to research the Cauchy problem for singularly perturbed higher-order linear integro-differential equation with a small parameters at the highest derivatives, provided that the roots of additional characteristic equation have negative signs. An explicit analytical formula of the solution of singularly perturbed Cauchy problem is obtained. The theorem about asymptotic estimate of a solution of the initial value problem is proved. The nonstandard degenerate initial value problem is constructed. We find the solution of the nonstandard degenerate initial value problem. An estimate difference of the solution of a singularly perturbed and nonstandard degenerate initial value problems is obtained. The asymptotic convergence of solution of a singularly perturbed initial value problem to the solution of the nonstandard degenerate initial value problem is established.
Key words: singular perturbation, small parameter, the initial functions, asymptotics, passage to the limit.

Introduction

The differential and integro-differential equations with small parameters at the highest derivatives are used as mathematical models of various problems of physics, astrophysics, chemistry, biology, mechanics, engineering, etc. At present time, these equations are called *singularly perturbed*.

The initial value problem with initial jumps for a nonlinear ordinary differential equation of the second order with a small parameter was studied by M.I. Vishik and L.A. Lyusternik [1] and K. A. Kassymov [2]. They show that the solution of the original initial value problem tends to the solution of the degenerate equation with changed initial conditions, when the small parameter approaches zero. Such problems became known as the Cauchy problems with *initial jumps*. The most general cases of the Cauchy problem for singularly perturbed nonlinear systems of ordinary differential and integro-differential equations, as well as for partial differential equations of hyperbolic type were studied by K.A. Kassymov [3-6].

For the first time, boundary value problems with initial jumps for singularly perturbed linear ordinary differential and integro-differential equations of the second order was studied by K. A. Kassymov [7, 8]. A systematic study of boundary value problems with initial jumps Kassymov and his students began in the nineties of the last century. He developed methods for qualitative research and the construction of an asymptotic expansion of solutions of boundary value problems with initial jumps for singularly perturbed ordinary differential equations [9, 10]. General boundary-value problems for singularly perturbed ordinary differential equations of higher orders are investigated by D. N. Nurgabyl. He singled out a class of singularly perturbed boundary value problems with an initial jump and developed an algorithm for constructing and investigating the asymptotic behavior of solutions of general boundary value problems [11, 12].

 Printed in Kazakhstan

K. A. Kassymov and M. K. Dauylbayev for singularly perturbed higher-order integro-differential equations studied problems of a special type, when the presence of integral terms leads to a qualitative change in the behavior of the solution [13-15]. It is shown that, in the absence of integral terms, the solution of the differential equation obtained in this case grows unboundedly as the small parameter tends to zero and, consequently, has no finite limit. But the solution of the initial integro-differential problem has a certain limit, but the limit function is not a solution of the usual degenerate equation. The initial jump takes not only a solution, but also integral terms. For singularly perturbed higher-order integro-differential equations, phenomena of initial jumps of any order were first revealed. It is established that this property essentially depends on the order of the derivatives entering under the integral sign.

M. K. Dauylbayev [16, 17] studied boundary value problems with two boundary layers possessing the phenomena of initial jumps. The novelty of these studies is that when the small parameter tends to zero, the fast solution variable grows unlimitedly, not only at one, the so-called initial point, but also at the other end of the considered segment. Thus, a class of singularly perturbed integro-differential equations with initial jump phenomena at both ends of the given segment is singled out. He also developed a method for studying and constructing the asymptotics of the solution of the Cauchy problem with initial jump for singularly perturbed linear differential equations with impulse action [18].

Main results

Consider the following singularly perturbed the initial value problem:

$$L_\varepsilon y \equiv \sum_{r=1}^{m} \varepsilon^r A_{n+r}(t) y^{(n+r)}(t,\varepsilon) + \sum_{k=0}^{n} A_k(t) y^{(k)}(t,\varepsilon) = F(t) + \int_0^1 \sum_{j=0}^{n+m-1} H_j(t,x) y^{(j)}(x,\varepsilon) dx, \tag{1}$$

$$y^{(i)}(0,\varepsilon) = \alpha_i,\ i = \overline{0, n+m-1}, \tag{2}$$

where $\varepsilon > 0$ is a small parameter, α_i, $i = \overline{0, n+m-1}$ are known constants, $A_{n+m}(t) = 1$.

We will need the following assumptions:

$$A_i(t) \in C^{(n+m-1)}([0,1]),\quad i = \overline{0, n+m},\quad F(t) \in C^{m-1}([0,1]) \tag{C1}$$

and $H_j(t,x) \in C^{m-1}(D),\quad j = \overline{0, n+m-1}$, where $D = \{0 \le t \le 1,\quad 0 \le x \le 1\}$.

(C2) $A_n(t) \neq 0,\quad 0 \le t \le 1.$

(C3) The roots $\mu_1 \neq \mu_2 \neq \ldots \neq \mu_m$ of "additional characteristic equation $\mu^m + A_{n+m-1}(t)\mu^{m-1} + \ldots + A_{n+1}(t)\mu + A_n(t) = 0$ satisfy the following inequalities $\mu_1 < 0,\quad \mu_2 < 0,\quad \ldots,\quad \mu_m < 0$.

Similarly the Cauchy problem (1), (2) for ordinary differential equation was considered in [19]. In the particular case, similarly boundary value problem with initial jumps for this case $m = 2,\quad l = 2$ [16, 17].

We consider the following homogeneous singularly perturbed differential equation associated with (1):

$$L_\varepsilon y(t,\varepsilon) \equiv \sum_{r=1}^{m} \varepsilon^r A_{n+r}(t) y^{(n+r)}(t,\varepsilon) + \sum_{k=0}^{n} A_k(t) y^{(k)}(t,\varepsilon) = 0. \tag{3}$$

The fundamental systems of solutions of the equation (3) has the following asymptotic representation as $\varepsilon \to 0$:

$$y_i^{(q)}(t,\varepsilon) = y_{i0}^{(q)}(t) + O(\varepsilon), \quad i = \overline{1,n}, \quad q = \overline{0,n+m-1}$$

$$y_{n+r}^{(q)}(t,\varepsilon) = \frac{1}{\varepsilon^q} e^{\frac{1}{\varepsilon}\int_0^t \mu_r(x)dx} \left(\mu_r^q(t) y_{n+r,0}(t) + O(\varepsilon)\right), \quad r = \overline{1,m}, \quad q = \overline{0,n+m-1} \tag{4}$$

where $y_{i0}(t), \quad i = \overline{1,n}$ are solutions of the problems:

$$L_0 y_{i0}(t) = 0, \quad y_{j0}^{(i-1)}(0) = \delta_{ij}, \quad i = \overline{1,n}, \quad j = \overline{0,n-1}, \tag{5}$$

δ_{ij} is a Kronecker symbol, $y_{n+r,0}(t), \quad r = \overline{1,m}$ are solutions of the following problems:

$$p_r(t) y'_{n+r,0}(t) + q_r(t) y_{n+r,0}(t) = 0,$$

$$y_{n+r,0}(0) = 1, \quad r = \overline{1,m},$$

where

$$p_r(t) = \sum_{i=0}^{m} A_{n+i}(t)(n+i)\mu_{r0}^{n+i-1}(t), \quad r = \overline{1,m},$$

$$q_r(t) = \mu'_{r0}(t)\sum_{i=0}^{m} A_{n+i}(t) C_{n+i}^2 \mu_{r0}^{n+i-2} + A_{n-1}(t)\mu_{r0}^{n-1}(t), \quad r = \overline{1,m},$$

$$C_{n+i}^2 = \frac{(n+i)!}{2!(n+i-2)!}, \quad i = \overline{0,m}.$$

In view of (4), for the Wronskian $W(t,\varepsilon)$ the following asymptotic representation holds as $\varepsilon \to 0$:

$$W(t,\varepsilon) = \frac{1}{\varepsilon^{\lambda}} \cdot \overline{W}(t)\pi(t)\omega(t) \exp\left(\frac{1}{\varepsilon}\int_0^t \overline{\mu}(x)dx\right)(1 + O(\varepsilon)) \neq 0, \tag{6}$$

where $\overline{W}(t)$ is the Wronskian,

$$\overline{W}(t) = \begin{vmatrix} y_{10}(t) & \dots & y_{n0}(t) \\ \dots & \dots & \dots \\ y_{10}^{(n-1)}(t) & \dots & y_{n0}^{(n-1)}(t) \end{vmatrix}, \quad \lambda = \frac{2n+m-1}{2},$$

$$\overline{\mu}(x) = \mu_1(x) + \dots + \mu_m(x) = \sum_{k=1}^{m} \mu_k(x),$$

$$\pi(t) = \prod_{k=1}^{m} y_{n+k,0}(t)\mu_k^n(t),$$

the determinant $\omega(t)$ is the $m-$th order Vandermond determinant,

$$\omega(t) = \begin{vmatrix} 1 & \dots & 1 \\ \mu_1(t) & \dots & \mu_m(t) \\ \dots & \dots & \dots \\ \mu_1^{m-1}(t) & \dots & \mu_m^{m-1}(t) \end{vmatrix} \neq 0.$$

Definition. The functions $K_i(t,s,\varepsilon), \quad i = \overline{1,n+m}$ are called initial functions, if they satisfy the following problem:

$$L_\varepsilon K_i(t,s,\varepsilon) = 0, \quad i = \overline{1,n+m}, \quad 0 \le s < t \le 1$$
$$K_i^{(j)}(s,s,\varepsilon) = \delta_{i-1,j}, \quad j = \overline{0,n+m-1}$$

and that can be represented in the form:

$$K_i(t,s,\varepsilon) = \frac{W_i(t,s,\varepsilon)}{W(s,\varepsilon)}, \quad i = \overline{1,n+m} \tag{7}$$

$W_i(t,s,\varepsilon)$ is the $n+m-$th order determinant obtained from the Wronskian $W(s,\varepsilon)$ by replacing the $i-$th row with $y_1(t,\varepsilon), \quad y_2(t,\varepsilon), \quad \dots, \quad y_{n+m}(t,\varepsilon)$.

In view of (6), (7), for the initial functions $K_i^{(q)}(t,s,\varepsilon), \quad i = \overline{1,n+m}$ the following asymptotic representation hold as $\varepsilon \to 0$:

$$K_i^{(q)}(t,s,\varepsilon)=\frac{\overline{W}_i^{(q)}(t,s)}{\overline{W}(s)}+\varepsilon^{n-q}\sum_{k=1}^{m}e^{\frac{1}{\varepsilon}\int_s^t\mu_k(x)dx}\frac{y_{n+k,0}(t)\mu_k^q(t)}{y_{n+k,0}(s)\mu_k^n(s)}\cdot\frac{\omega_{1k}(s)}{\omega(s)}\cdot\frac{\overline{W}_i(s)}{\overline{W}(s)}+O\left(\varepsilon+\varepsilon^{n+1-q}\sum_{k=1}^{m}e^{\frac{1}{\varepsilon}\int_s^t\mu_k(x)dx}\right), \tag{8}$$

$$i=\overline{1,n},\qquad q=\overline{0,n+m-1};$$

$$K_{n+r}^{(q)}(t,s,\varepsilon)=\varepsilon^r\left[(-1)^r\frac{\omega_{r+1}(s)}{\omega(s)A_n(s)}\cdot\frac{\overline{W}_n^{(q)}(t,s)}{\overline{W}(s)}+\varepsilon^{n-1-q}\sum_{k=1}^{m}e^{\frac{1}{\varepsilon}\int_s^t\mu_k(x)dx}+\frac{y_{n+k,0}(t)\mu_k^q(t)}{y_{n+k,0}(s)\mu_k^n(s)}\cdot\frac{\omega_{rk}(s)}{\omega(s)}+O\left(\varepsilon+\varepsilon^{n-q}\sum_{k=1}^{m}e^{\frac{1}{\varepsilon}\int_s^t\mu_k(x)dx}\right)\right], \tag{9}$$

$$r=\overline{1,m},\ \ q=\overline{0,n+m-1}$$

where $\omega_{ij}(s)$ is the $m-1-$th order determinant obtained from the determinant $\omega(s)$ by deleting i-th row and j-th column, $\omega_i(s)$ is the $m-$th order determinant obtained from the following determinant

$$\begin{vmatrix} 1 & .... & 1 \\ \mu_1(s) & ... & \mu_m(s) \\ \dots & \dots & \dots \\ \mu_1^m(s) & ... & \mu_m^m(s) \end{vmatrix}$$

by deleting i-th row, $\overline{W}_n^{(q)}(t,s)$ is the determinant obtained from the Wronskian $\overline{W}(s)$ by replacing the n-th row with $y_{10}^{(q)}(t),...,y_n^{(q)}(t)$, $\overline{W}_i(t)$ is the $n+1-$th order determinant obtained from the following determinant

$$\begin{vmatrix} y_{10}(t) & .... & y_{n0}(t) \\ y'_{10}(t) & ... & y'_{n0}(t) \\ \dots & \dots & \dots \\ y_{10}^{(n)}(t) & ... & y_{n0}^{(n)}(t) \end{vmatrix}$$

by deleting the i-th row.

Let us denote by the right-hand side of the equation (1):

$$z(t,\varepsilon)=F(t)+\int_0^1\sum_{j=0}^{n+m-1}H_j(t,x)y^{(j)}(x,\varepsilon)dx \tag{10}$$

We seek to find the solution of the differential $L_\varepsilon y=z(t,\varepsilon)$ equation in the form:

$$y(t,\varepsilon)=\sum_{i=1}^{n+m}C_iK_i(t,0,\varepsilon)+\\+\frac{1}{\varepsilon^m}\int_0^t\mathbf{K}_{n+m}(t,s,\varepsilon)z(s,\varepsilon)ds \tag{11}$$

where $K_i(t,s,\varepsilon),\ \ i=\overline{1,n+m}$ are the initial functions, $z(t,\varepsilon)$ is a unknown function. Substituting (11) into (10), we obtain that $z(t,\varepsilon)$ satisfies the following Fredholm integral equation of the second kind:

$$z(t,\varepsilon)=f(t,\varepsilon)+\int_0^1H(t,s,\varepsilon)z(s,\varepsilon)ds \tag{12}$$

where

$$f(t,\varepsilon)=F(t)+\sum_{i=1}^{n+m}C_i\int_0^1\sum_{j=0}^{n+m-1}H_j(t,x)K_i^{(j)}(x,0,\varepsilon)dx,$$

$$H(t,s,\varepsilon)=\frac{1}{\varepsilon^m}\int_s^1\sum_{j=0}^{n+m-1}H_j(t,x)K_{n+m}^{(j)}(x,s,\varepsilon)dx.$$

(C4) 1 is not an eigenvalue of the kernel $H(t,s,\varepsilon)$.

In view of condition (C4) integral equation (12) has an unique solution, that can be represented in the form

$$z(t,\varepsilon)=f(t,\varepsilon)+\int_0^1R(t,s,\varepsilon)f(s,\varepsilon)ds \tag{13}$$

where $R(t,s,\varepsilon)$ is a resolvent of the kernel $H(t,s,\varepsilon)$.

Substituting (13) into (11), we obtain the analytical formula of solution:

$$y(t,\varepsilon)=\sum_{i=1}^{n+m}C_i\left(K_i(t,0,\varepsilon)+\frac{1}{\varepsilon^m}\int_0^t K_{n+m}(t,s,\varepsilon)\overline{\varphi}_i(s,\varepsilon)ds\right)+\frac{1}{\varepsilon^m}\int_0^t K_{n+m}(t,s,\varepsilon)\overline{F}(s,\varepsilon)ds \qquad (14)$$

where C_i, $i=\overline{1,n+m}$ are unknown constants, $K_i(t,s,\varepsilon)$, $i=\overline{1,n+m}$ are the initial functions,

$$\begin{gathered}\overline{\boldsymbol{\phi}}_i(s,\boldsymbol{\varepsilon})=\int_0^1\sum_{j=0}^{n+m-1}\overline{H}_j(s,x,\boldsymbol{\varepsilon})K_i^{(j)}(x,s,\boldsymbol{\varepsilon})dx,\\ i=\overline{1,n+m}\\ \overline{H}_j(s,x,\boldsymbol{\varepsilon})=H_j(s,x)+\int_0^1 R(s,p,\boldsymbol{\varepsilon})H_j(p,x)dp\\ \overline{F}(s,\boldsymbol{\varepsilon})=F(s)+\int_0^1 R(s,p,\boldsymbol{\varepsilon})F(p)dp.\end{gathered} \qquad (15)$$

By using initial conditions (2) in (14), we find the constants $C_i=\alpha_{i-1}$, $i=\overline{1,n+m-1}$.

Theorem 1. (Theorem about the analytical formula of solution) Let assumptions (C1)-(C4) hold. Then the Cauchy problem (1), (2) on the segment $0\le t\le 1$ has an unique solution and is expressed by the formula:

$$\begin{gathered}y(t,\boldsymbol{\varepsilon})=\\ =\sum_{i=1}^{n+m}\boldsymbol{\alpha}_{i-1}\left(K_i(t,0,\boldsymbol{\varepsilon})+\frac{1}{\boldsymbol{\varepsilon}^m}\int_0^t K_{n+m}(t,s,\boldsymbol{\varepsilon})\overline{\boldsymbol{\phi}}_i(s,\boldsymbol{\varepsilon})ds\right)+\\ +\frac{1}{\boldsymbol{\varepsilon}^m}\int_0^t K_{n+m}(t,s,\boldsymbol{\varepsilon})\overline{F}(s,\boldsymbol{\varepsilon})ds\end{gathered} \qquad (16)$$

where $K_i(t,s,\varepsilon)$, $i=\overline{1,n+m}$ are the initial functions, functions $\overline{H}_j(s,x,\varepsilon)$, $j=\overline{0,n+m-1}$, $\overline{\varphi}_i(s,\varepsilon)$, $\overline{F}(s,\varepsilon)$ is defined by the formula (15).

Theorem 2. (Theorem about asymptotic estimations of solution) Let assumptions (C1)-(C4) hold. Then the Cauchy problem (1), (2) and its derivatives the following asymptotic estimation hold as $\varepsilon\to 0$:

$$\left|y^{(q)}(t,\boldsymbol{\varepsilon})\right|\le C\left(\sum_{i=0}^{n-1}|\boldsymbol{\alpha}_i|+\sum_{r=1}^{m}\boldsymbol{\varepsilon}^r\cdot|\boldsymbol{\alpha}_{n-1+r}|+\max_{0\le t\le 1}|F(t)|\right)+C\boldsymbol{\varepsilon}^{n-q}e^{-\boldsymbol{\gamma}\frac{t}{\boldsymbol{\varepsilon}}}\left(\sum_{i=0}^{n}|\boldsymbol{\alpha}_i|+\sum_{r=1}^{m-1}\boldsymbol{\varepsilon}^r\cdot|\boldsymbol{\alpha}_{n+r}|+\max_{0\le t\le 1}|F(t)|\right)\cdot\left|\sum_{k=1}^{m}\frac{\overline{\boldsymbol{\mu}}_k^q(t)\boldsymbol{\omega}_{mk}(t)}{\overline{\boldsymbol{\mu}}_k^{n+1}(0)}\right|, \qquad (17)$$
$$q=\overline{0,n+m-1}$$

where $C>0,\gamma>0$ are constant independent of ε, $\left.\sum_{k=1}^{m}\frac{\overline{\mu}_k^q(t)\omega_{mk}(t)}{\overline{\mu}_k^{n+1}(0)}\right|_{t=0}\equiv 0$, $q=\overline{n+1,n+m-1}$.

Proof: In view of (7)-(9) and conditions (C1)-(C3), for the initial functions $K_i(t,s,\varepsilon)$, $i=\overline{1,n+m}$ the following asymptotic estimation hold:

$$\left|K_i^{(q)}(t,s,\boldsymbol{\varepsilon})\right|\le C\left(1+\boldsymbol{\varepsilon}^{n-q}\exp\left(-\frac{t-s}{\boldsymbol{\varepsilon}}\right)\right), \qquad (18)$$
$$i=\overline{1,n},\ q=\overline{0,n+m-1},$$

$$\left|K_{n+r}^{(q)}(t,s,\boldsymbol{\varepsilon})\right|\le C\boldsymbol{\varepsilon}^r\left(1+\boldsymbol{\varepsilon}^{n-1-q}\exp\left(-\frac{t-s}{\boldsymbol{\varepsilon}}\right)\right), \qquad (19)$$
$$r=\overline{1,m},\ q=\overline{0,n+m-1}.$$

By applying the asymptotic estimations of the initial functions (18), (19) in (15), we obtain the following asymptotic estimations for the functions $\overline{\varphi}_i(s,\varepsilon)$, $i=\overline{1,n+m}$:

$$\begin{gathered}\left|\overline{\varphi}_i(s,\varepsilon)\right|\le C,\quad i=\overline{1,n},\\ \left|\overline{\varphi}_{n+r}(s,\varepsilon)\right|\le C\varepsilon^r,\quad r=\overline{1,m}\end{gathered} \qquad (20)$$

By applying (18)-(20) in (16), we obtain asymptotic estimations of the solution (17). Theorem 2 is proved.

We consider the following nonstandard unperturbed initial value problem:

$$\begin{gathered}L_0[\overline{y}(t)]\equiv\sum_{k=0}^{n}A_k(t)\overline{y}^{(k)}(t)=\\ =F(t)+\int_0^1\sum_{j=0}^{n+m-1}H_j(t,x)\overline{y}^{(j)}(x)dx,\end{gathered} \qquad (21)$$

$$\overline{y}^{(i)}(0)=\alpha_i,\quad i=\overline{0,n-1}. \tag{22}$$

We introduce the initial functions for the problem (21), (22), similar to functions (7):

$$\overline{K}_i(t,s)=\frac{\overline{W}_i(t,s)}{\overline{W}(s)},\quad i=\overline{1,n} \tag{23}$$

where $\overline{W}_i(t,s)$ is the $n-$th order determinant obtained from the Wronskian $\overline{W}(s)$ by replacing the $i-$th row with $y_{10}(t),\ y_{20}(t),\ \ldots,\ y_{n0}(t)$.

It is clear that the initial $\overline{K}_i(t,s)$, $i=\overline{1,n}$ functions will be the solution for the following problem:

$$L_0\overline{K}_i(t,s)=0,\quad i=\overline{1,n},\ t\neq s$$

$$\overline{K}_i^{(j-1)}(s,s)=\delta_{i,j-1},\quad i=\overline{1,n},\quad j=\overline{1,n}.$$

Differentiating $m-1$ times the equation (21) with respect to variable t, then backwards integrating $m-1$ times on the segment $[0,t]$, we get the auxiliary equation:

$$L_0[\overline{y}(t)]=F(t)+\sum_{k=0}^{m-2}B_k\frac{t^k}{k!}+\int_0^t\frac{(t-s)^{m-2}}{(m-2)!}Q[\overline{y}(s)]ds, \tag{24}$$

where B_k, $k=\overline{0,m-2}$ are arbitrary constants, operator Q is a linear integro-differential operator

$$Q[\overline{y}(t)]=\int_0^1\sum_{j=0}^{n+m-1}H_j^{(m-1)}(t,x)\overline{y}^{(j)}(x)dx, \tag{25}$$

symbol $H_j^{(m-1)}(t,x)$ means the $m-1-$th order derivative with respect to variable t of the function $H_j(t,x)$.

If the constants B_k, $k=\overline{0,m-2}$ satisfy the conditions

$$B_k=\int_0^1\sum_{j=0}^{n+m-1}H_j^{(k)}(0,x)\overline{y}^{(j)}(x)dx,\quad k=\overline{0,m-2} \tag{26}$$

then the equations (21) and (24) will be equivalent. Let us consider the equation (24) with initial conditions (22).

The solution of the Cauchy problem (22), (24) is as follows:

$$\overline{y}(t)=\sum_{i=1}^{n}C_i\overline{K}_i(t,0)+\varphi(t)+\sum_{k=0}^{m-2}B_k\varphi_k(t)+\int_0^t\frac{\hat{K}_n(t,s)}{A_n(t)}Q[\overline{y}(s)]ds \tag{27}$$

where $\overline{K}_i(t,s)$, $i=\overline{1,n}$ are the initial functions, operator Q is defined by the formula (25),

$$\boldsymbol{\phi}(t)=\int_0^t\frac{\overline{K}_n(t,s)}{A_n(t)}F(s)ds,$$

$$\boldsymbol{\phi}_k(t)=\int_0^t\frac{\overline{K}_n(t,s)}{A_n(t)}\cdot\frac{s^k}{k!}ds,\quad k=\overline{0,m-2} \tag{28}$$

$$\hat{K}_n(t,s)=\int_s^t\overline{K}_n(t,p)\frac{(p-s)^{m-2}}{(m-2)!}dp.$$

Function $\hat{K}_n(t,s)$ satisfy the following problem:

$$L_0[\overline{y}(t)]=\frac{(t-s)^{m-2}}{(m-2)!},$$

$$\hat{K}_n^{(j)}(s,s)=\begin{cases}0, & j=\overline{0,m-2}\\ 1, & j=m-1\end{cases}.$$

Substituting (27) into (22), in view of the condition of the initial functions $\overline{K}_i(t,s)$, $i=\overline{1,n}$, we find the constants $C_i=\alpha_{i-1}$, $i=\overline{1,n}$. We put defined constants $C_i=\alpha_{i-1}$, $i=\overline{1,n}$ in (27):

$$\bar{y}(t)=\sum_{i=1}^{n}\alpha_{i-1}\bar{K}_i(t,0)+\varphi(t)+\sum_{k=0}^{m-2}B_k\varphi_k(t)+\int_0^t\frac{\hat{K}_n(t,s)}{A_n(t)}Q[\bar{y}(s)]ds \tag{29}$$

where $\bar{K}_i(t,s),\ \ i=\overline{1,n}$ are the initial functions, operator Q is defined by the formula (25), functions $\varphi(t),\ \ \varphi_k(t),\ \ k=\overline{0,m-2},\ \ \hat{K}_n(t,s)$ are defined by the formula (28).

Applying operator Q to the equation (29), we arrive Fredholm integral equation of the second type

$$u(t)=\sum_{i=1}^{n}\alpha_{i-1}\tilde{K}_i(t,0)+\omega(t)+\sum_{k=0}^{m-2}B_k\omega_k(t)+\int_0^1M(t,s)u(s)ds, \tag{30}$$

where

$$M(t,s)=\begin{cases}\int_s^0\sum_{j=0}^{n+m-1}H_j^{(m-1)}(t,\tau)\hat{K}_n^{(j)}(\tau,s)d\tau+H_{n+m-1}(t,s), & s\le 0\\ \int_s^1\sum_{j=0}^{n+m-1}H_j^{(m-1)}(t,\tau)\hat{K}_n^{(j)}(\tau,s)d\tau+H_{n+m-1}(t,s), & s\ge 0\end{cases}, \tag{31}$$

functions $u(t),\ \ \boldsymbol{\omega}(t),\ \ \boldsymbol{\omega}_k(t),\ \ k=\overline{0,m-2},\ \ \tilde{K}_i(t,0),\ \ i=\overline{1,n}$ are expressed the following form:

$$u(t)=Q[\bar{y}(t)],\quad \omega(t)=Q[\varphi(t)],$$

$$\omega_k(t)=Q[\varphi_k(t)],\quad k=\overline{0,m-2},$$

$$\tilde{K}_i(t,0)=Q[\bar{K}_i(t,0)],\quad i=\overline{1,n}. \tag{32}$$

(C5) 1 is not an eigenvalue of the kernel $M(t,s)$

We introduce the operator:

$$A\upsilon(t)\equiv\upsilon(t)+\int_0^1\bar{R}(t,s)\upsilon(s)ds, \tag{33}$$

where function $\bar{R}(t,s)$ is a resolvent of the kernel $M(t,s)$. In view of the condition (C5), then the integral equation (30) has an unique solution and that can be represented in the form:

$$\begin{aligned}u(t)=&\sum_{i=1}^{n}\boldsymbol{\alpha}_{i-1}A\tilde{K}_i(t,0)+\\&+A\boldsymbol{\omega}(t)+\sum_{k=0}^{m-2}B_kA\boldsymbol{\omega}_k(t)\end{aligned} \tag{34}$$

where operator A is defined by the formula (33), $\omega(t),\ \ \omega_k(t),\ \ k=\overline{0,m-2},\ \ \tilde{K}_i(t,0),\ \ i=\overline{1,n}$ are defined by the formula (32).

Substituting the solution (34) into (29), we obtain the solution of the unperturbed problem (21), (22):

$$\bar{y}(t)=\sum_{i=1}^{n}\alpha_{i-1}\breve{K}_i(t,0)+\varphi(t)+\int_0^t\frac{\hat{K}_n(t,s)}{A_n(t)}A\omega(s)ds+\sum_{k=0}^{m-2}B_k\left(\varphi_k(t)+\int_0^t\frac{\hat{K}_n(t,s)}{A_n(t)}A\omega_k(s)ds\right) \tag{35}$$

where

$$\breve{K}_i(t,0)=\bar{K}_i(t,0)+\int_0^t\frac{\hat{K}_n(t,s)}{A_n(t)}A\tilde{K}_i(s,0)ds,\quad i=\overline{1,n}.$$

We introduce the following symbols:

$$\begin{aligned}\eta(t)=&\sum_{i=1}^{n}\alpha_{i-1}\breve{K}_i(t,0)+\varphi(t)+\int_0^t\frac{\hat{K}_n(t,s)}{A_n(t)}A\omega(s)ds,\\ \boldsymbol{\eta}_k(t)=&\boldsymbol{\phi}_k(t)+\int_0^t\frac{\hat{K}_n(t,s)}{A_n(t)}A\boldsymbol{\omega}_k(s)ds,\\ &k=\overline{0,m-2}\end{aligned} \tag{36}$$

Then the solution (35) is as follows:

$$\bar{y}(t) = \eta(t) + \sum_{k=0}^{m-2} B_k \eta_k(t). \qquad (37)$$

If applying operator Q to the functions $\eta(t)$, $\eta_k(t)$ in (36), we get the following equalities:

$$A\omega(t) = Q[\eta(t)], \quad A\omega_k(t) = Q[\eta_k(t)], \quad k = \overline{0, m-2} \qquad (38)$$

where operator A is defined by the formula (33).

Taking into account formulas (36) and (38), it is easy to verify that the function (37) satisfies equation (29). That this function is a solution of the equation (21), it is necessary to subordinate the constants B_k, $k = \overline{0, m-2}$ to the conditions (26). Substituting (37) into (26), we get the following system for determining B_k, $k = \overline{0, m-2}$:

$$B_k - \sum_{i=0}^{m-2} a_{ki} \cdot B_i = a_k, \quad k = \overline{0, m-2}, \qquad (39)$$

where

$$a_k = \int_0^1 \sum_{j=0}^{n+m-1} H_j^{(k)}(0,x)\eta^{(j)}(x)dx,$$

$$a_{ki} = \int_0^1 \sum_{j=0}^{n+m-1} H_j^{(k)}(0,x)\eta_i^{(j)}(x)dx.$$

Let Δ be a determinant of the system (39).

(C6) $\Delta \neq 0$. If the condition (C6) is valid, then the constants B_k, $k = \overline{0, m-2}$ is defined single-valued.

Theorem 3. Let assumptions (C1)-(C6) hold. Then the nonstandard unperturbed problem (21), (22) on the segment $0 \le t \le 1$ has an unique solution and is defined by the formula (37).

Let us denote by

$$u(t,\varepsilon) = y(t,\varepsilon) - \bar{y}(t) \quad \Rightarrow \quad y(t,\varepsilon) = u(t,\varepsilon) + \bar{y}(t). \qquad (40)$$

Substituting (40) into the problem (1), (2), in view of the problem (21), (22), we get the following problem for $u(t,\varepsilon)$:

$$L_\varepsilon u \equiv \sum_{r=1}^{m} \varepsilon^r A_{n+r}(t) u^{(n+r)} + \sum_{k=0}^{n} A_k(t) u^{(k)} = -\sum_{r=1}^{m} \varepsilon^r A_{n+r}(t) \bar{y}^{(n+r)} + \int_0^1 \sum_{j=0}^{n+m-1} H_j(t,x) u^{(j)}(x,\varepsilon)dx \qquad (41)$$

$$u^{(i)}(0,\varepsilon) = 0, \quad i = \overline{0, n-1},$$
$$u^{(i)}(0,\varepsilon) = \alpha_i - \bar{y}^{(i)}(0), \quad i = \overline{n, n+m-1}. \qquad (42)$$

The problem (41), (42) is of the same type as the problem (1), (2), by applying estimates (17), we get asymptotic estimations for the function $u(t,\varepsilon)$ as $\varepsilon \to 0$:

$$\left|u^{(q)}(t,\varepsilon)\right| \le C\left(\sum_{r=1}^{m} \varepsilon^r \cdot \left|\alpha_{n-1+r} - \bar{y}^{(n-1+r)}(0)\right| + \varepsilon\right) +$$
$$+ C\varepsilon^{n-q} e^{-\gamma\frac{t}{\varepsilon}} \left(\sum_{r=1}^{m-1} \varepsilon^r \cdot \left|\alpha_{n+r} - \bar{y}^{(n+r)}(0)\right| + \varepsilon\right) \cdot \left|\sum_{k=1}^{m} (-1)^{2n+m+k} \frac{\bar{\mu}_k^j(t)\omega_{mk}(t)}{\bar{\mu}_k^{n+1}(0)}\right|, \qquad (43)$$
$$q = \overline{0, n+m-1}.$$

From the estimations (43), the following limiting equalities hold:

$$\lim_{\varepsilon\to 0} u^{(q)}(t,\varepsilon)=0, \quad 0\le t\le 1, \quad q=\overline{0,n},$$

$$\lim_{\varepsilon\to 0} u^{(q)}(t,\varepsilon)=0, \quad 0< t\le 1, \quad q=\overline{n+1,n+m-1}.$$

Theorem 4. Let assumptions (C1)-(C6) hold. Then for the solution $y(t,\varepsilon)$ of the Cauchy problem (1), (2) the following limiting equalities hold:

$$\lim_{\varepsilon\to 0} y^{(q)}(t,\varepsilon)=\bar{y}^{(q)}(t), \quad 0\le t\le 1, \quad q=\overline{0,n},$$

$$\lim_{\varepsilon\to 0} y^{(q)}(t,\varepsilon)=\bar{y}^{(q)}(t), \quad 0< t\le 1, \quad q=\overline{n+1,n+m-1},$$

where function $\bar{y}(t)$ is the solution of the nonstandard unperturbed problem (21), (22) and is defined by the formula (37).

Conclusion

The article is devoted to study the initial value problem for singularly perturbed the $n+m-$th order linear integro-differential equation with a small parameters at the $m-$th derivatives. An explicit analytical formula of the solution of singularly perturbed initial value problem is obtained. The nonstandard degenerate initial value problem is constructed. The solution of the nonstandard degenerate initial value problem is obtained. The asymptotic convergence of solution of a singularly perturbed initial value problem to the solution of the nonstandard degenerate initial value problem is proved.

Acknowledgement

The authors were supported in parts by the MESRK grant AP05132587 "Boundary value problems for singularly perturbed differential equations with a continuous and piecewise constant argument" (2018-2020) of the Committee of Science, Ministry of Education and Science of the Republic of Kazakhstan.

References

1. Vishik I., Lyusternik L. A. “On the initial jump for non-linear differential equations containing a small parameter.” *Doklady Akademii Nauk SSSR* 132, no. 6 (1960): 1242-1245.

2. Kassymov K. A. “On the asymptotics of the solution of the Cauchy problem with large initial conditions for nonlinear ordinary differential equations containing a small parameter.” *Uspehi Mat. Nauk* 17, no. 5 (1962): 187-188.

3. Kassymov K. A. “The initial jump problem for non-linear systems of differential equations containing a small parameter.” *Doklady Akademii Nauk SSSR* 179, no. 2. (1968): 275-278.

4. Kassymov K. A. “Asymptotics of solutions of Cauchy problem with an initial jump for non-linear systems of integro-differential equations with a small parameter for the highest derivative.” *Izvestiya Akademii Nauk Kazakhskoi SSR* no. 5 (1968): 69-72.

5. Kassymov K. A. “Asymptotics of the solution of a problem with initial jump for nonlinear systems of differential equations with a small parameter in the highest derivative.” *Doklady Akademii Nauk SSSR* 189, no. 5 (1969): 941-944.

6. Kassymov K. A. “Asymptotics of the solutions of the problem with an initial jump for a system of differential equations of hyperbolic type with a small parameter at the derivative.” *Doklady Akademii Nauk SSSR* 196, no. 2 (1971): 274-277.

7. Kassymov K. A. *Linear singularly perturbed second-order differential equations*. Almaty: 1981. – 112 p.

8. Kassymov K. A. “Boundary value problems with initial jumps for differential equations.” *Uspekhi Matematicheskikh Nauk* 39, no. 4 (1984): 132-133.

9. Kassymov K. A., Abildayev E.A. “Asymptotic estimates for solutions of singularly perturbed boundary value problems with initial jumps for linear differential equations.” *Differential equations* 28, no. 10 (1992): 1659-1669.

10. Kassymov K. A. *Singularly perturbed boundary value problems with initial jumps*. Almaty: Sanat, 1997. – 176 p.

11. Kassymov K.A., Nurgabyl D.N. “Asymptotic behavior of solutions of linear singularly perturbed general separated boundary-value problems with initial jump.” *Ukrainian Mathematical Journal* 55, no 11 (2003): 1777-1792.

12. Kassymov K.A., Nurgabyl D.N. “Asymptotic estimates of solution of a singularly perturbed boundary value problem with an initial jump for linear differential equations.” *Differential Equations* 40, no 5 (2004): 641-651.

13. Kassymov K.A., Dauylbaev M.K. “Estimation of solutions of the Cauchy problem with initial jump of any order for linear singularly perturbed differential equations.” *Differential equations* 35, no 6 (1999): 822-830.

14. Dauylbaev M.K. “The asymptotic behavior of solutions to singularly perturbed nonlinear integro-differential equations.” *Siberian Mathematical Journal* 41, no. 1 (2000): 49-60.

15. Kassymov K.A., Dauylbaev M.K. “Singularly perturbed linear integro-differential equations with initial jumps of any order.” *Izvestiya VUZov. Matematika* 494, no. 7 (2003): 70-75.

16. Dauylbaev M.K., Mirzakulova A.E. “Asymptotic behavior of solutions of singular integro-differential equations.” *Journal of Discontinuity, Nonlinearity, and Complexity* 5, no. 2 (2016): 147-154.

17. Dauylbaev M.K., Mirzakulova A.E. “Boundary-value problems with initial jumps for singularly perturbed integrodifferential equations.” *Journal of Mathematical Sciences* 222, no. 3 (2017): 214-225.

18. Dauylbaev M.K., Mirzakulova A.E., Ergaliev M.G. “Asymptotic behavior of solutions of the Cauchy problem for singularly perturbed differential equations with impulse action.” *Bulletin KazNPU named after Abay* 49, no. 1 (2015): 24-29.

19. Nurgabyl D.N. “Asymptotic estimates for the solution of the initial value problem for linear differential equations with a small parameter for the highest derivatives.” *Bulletin ZhSU named after Zhansugurov* no. 2 (2012): 4-8.

IRSTI 44.31.31

[1]A. Askarova, [2]S. Bolegenova, [3]P. Safarik, [1]V. Maximov, [*1]M. Beketayeva

[1]Scientific Research Institute of Experimental and Theoretical Physics, Almaty, Kazakhstan
[2]Physics and Technical Physics Department, Al-Farabi Kazakh National University, Almaty, Kazakhstan
[3]Thermodynamics and Fluid Dynamics Department, Czech Technical University in Prague, Prague, Czech Republic
[*]e-mail: Beketayeva.m@gmail.com

Heat and mass transfer processes at high-temperature media during combustion of low-grade pulverized coal

Abstract. The article is devoted to the complex research processes of heat and mass transfer occurring in the real conditions of solid fuel (coal) combustion. Development of technological processes with economic and ecological advantages are the main purpose for many researches in thermal physics and technical physics. The complex processes of heat and mass transfer in the presence of combustion are non-stationary, strongly non-isothermal with a constant change in the physical and chemical state of the environment. It greatly complicates their experimental study. In this case, studying of heat and mass transfer in high-reacting media with simulation of physical and chemical processes occur during combustion of pulverized coal is important for the solution of modern power engineering industry and ecology problems. In this regard, a comprehensive study of heat and mass transfer processes at high-temperature media observed. Investigations based on the achievements of modern physics by using numerical methods for 3D modeling. Numerical experiments are conducted to describe and study aerodynamic characteristics, heat and mass transfer processes during the burning of pulverized Kazakhstan low-grade coal. The results obtained are of great practical importance, since they allow us to develop recommendations for the improvement and design of new combustion chambers and burners, and also can be useful in optimizing the whole process of burning fossil fuels.
Key words: aerodynamic, combustion, heat exchange, numerical experiment.

Introduction

Solid fuel combustion is a complex physical and chemical phenomenon, which occurs at high temperatures with rapid and complete oxidation of combustible matter (carbon) by atmospheric oxygen and accompanied by a large amount of heat release [1-2]. Due to the low quality of main Kazakh coal deposits their exploitation at industry has increased scientific and applied relevance. Conducting of deep research on coal combustion in the real conditions can ensure the efficient technological process at all [3-5]. Heightened interest observed in particular to the study of heat and mass transfer processes at combustion of pulverized Kazakh coal with high ash content [6-7]. As it known combustion processes take place under conditions of strong turbulence and non-isothermal flow, multiphase medium with a significant impact of nonlinear effects of thermal radiation, interfacial interaction and multistage proceeding with chemical reactions [8-9]. Such phenomena have an important role in studying of the natural phenomenon of low-grade coal combustion. So investigations of turbulent chemically reacting media are extremely important to deepen knowledge of physical and chemical properties, for application possibilities.

In the context of depletion of natural energy resources and environmental pollution rational use of energy fuel, increasing the efficiency of energy generation and solution of environmental problems are urgent and important task to solve. Development of technological processes with economic and ecological advantages are the main purpose for

 Printed in Kazakhstan

many researches in this area. The complex processes of heat and mass transfer in the presence of combustion are non-stationary, strongly non-isothermal with a constant change in the physical and chemical state of the environment. It greatly complicates their experimental study. In this case, studying of heat and mass transfer in high-reacting media with simulation of physical and chemical processes occur during combustion of pulverized coal is important for the solution of modern power engineering industry and ecology problems. In this regard, a comprehensive study of heat and mass transfer processes at high-temperature media observed. Investigations based on the achievements of modern physics by using numerical methods for 3D modeling [10-15] that in turn do not need labor force also much time. Applying of computational technology allow us to describe the actual physical processes that occur during combustion of energy fuel as accurate as possible. Finally, it has been put the objective of this paper oriented on holding numerical experiments on studying heat and mass transfer processes occurring in the areas of real geometry of the combustion chamber during the burning of energy fuel. It has been established mathematical model of physical-chemical combustion process.

Materials and methods

Study of processes of heat and mass transfer during coal combustion is possible only based on a complete theory of combustion physics. It includes a wide range of physical and chemical effects and its formulation of a mathematical model. For the simulation of heat and mass transfer in the presence of physical and chemical processes are used the fundamental laws of conservation of mass, momentum, energy [16-19]. Heat and mass transfer processes in the presence of physical and chemical transformations – is the interaction of turbulent flows. Therefore, the chemical processes here should take into account the law of conservation of components of the reacting mixture, multiphase medium, its turbulence degree, heat generation due to the radiation of heated fluid and chemical reactions. The law of conservation of substance written in the form of the law of conservation of matter as follows:

$$\frac{\partial \rho}{\partial t}+\frac{\partial}{\partial x_i}\left(\rho u_i\right)=q_N .$$

The law of conservation of momentum and the equation of motion expressed as:

$$\frac{\partial}{\partial t}\left(\rho u_i\right)=-\frac{\partial}{\partial x_j}\left(\rho u_i u_j\right)+\frac{\partial \tau_{ij}}{\partial x_j}-\frac{\partial P}{\partial x_i}+\rho f_i .$$

Law of energy conservation:

$$\frac{\partial}{\partial t}\left(\rho h\right)=-\frac{\partial}{\partial x_i}\left(\rho u_i h\right)-\frac{\partial q_i^{res}}{\partial x_j}+ \\ +\frac{\partial P}{\partial t}+u_i\frac{\partial P}{\partial x_i}+\tau_{ij}\frac{\partial u_j}{\partial x_i}+S_h .$$

The conservation law for the components of the reaction mixture:

$$\frac{\partial}{\partial t}\left(\rho C_\beta\right)=-\frac{\partial}{\partial x_i}\left(\rho C_\beta u_i\right)+\frac{\partial j_i}{\partial x_i}+S_\beta .$$

For technical flames, it takes into account the transfer of matter only by diffusion. Transfer of substance due to the pressure gradient, the action of external forces (electric and magnetic fields) and thermal diffusion are small and they be neglected. Then the last equation written as follow:

$$\frac{\partial}{\partial t}\left(\rho C_\beta\right)=-\frac{\partial}{\partial x_i}\left(\rho C_\beta u_i\right)+ \\ -\frac{\partial}{\partial x_i}\left(\frac{\mu_{eff}}{\sigma_{\beta eff}}\frac{\partial C_\beta}{\partial x_i}\right)+S_\beta .$$

In this paper for modeling of turbulence flows used the standard k-ε turbulence model, excluding the effect of lift or "twist" of flow, which is represented by the equation of turbulent kinetic energy transfer:

$$\frac{\partial\left(\overline{\rho}\,k\right)}{\partial t}=-\frac{\partial\left(\overline{\rho}\;\overline{u}_j\,k\right)}{\partial x_j}+ \\ +\frac{\partial}{\partial x_j}\left[\frac{\mu_{eff}}{\sigma_k}\frac{\partial k}{\partial x_j}\right]+P-\overline{\rho}\cdot\varepsilon .$$

And the equation of dissipation (turbulent kinetic energy conversion into internal) turbulent kinetic energy ε:

$$\frac{\partial\left(\overline{\rho}\,\overline{\varepsilon}\right)}{\partial t}=-\frac{\partial\left(\overline{\rho}\,\overline{u_j}\,\overline{\varepsilon}\right)}{\partial x_j}+\frac{\partial}{\partial x_j}\left[\frac{\mu_{eff}}{\sigma_{\varepsilon}}\frac{\partial\varepsilon}{\partial x_j}\right]+$$
$$+C_{\varepsilon,1}\cdot\frac{\varepsilon}{k}\cdot P-C_{\varepsilon,2}\cdot\frac{\varepsilon^2}{k}\cdot\overline{\rho}$$

Here the kinetic energy production:

$$P=\left[\mu_{turb}\cdot\left(\frac{\partial\overline{u_i}}{\partial x_j}+\frac{\partial\overline{u_j}}{\partial x_i}\right)-\frac{2}{3}\cdot\rho\cdot k\cdot\delta_{ij}\right]\cdot\frac{\partial\overline{u_i}}{\partial x_j}.$$

And the rate of dissipation of turbulent energy:

$$\overline{\rho\varepsilon}=\mu_{turb}\cdot\frac{\partial u'_i}{\partial x_j}\cdot\left(\frac{\partial u'_i}{\partial x_j}+\frac{\partial u'_j}{\partial x_i}\right).$$

If k and ε are known, the turbulent viscosity determined by the Prandtl-Kolmogorov relationship as: $\mu_{turb}=c_{\mu}\rho\frac{k^2}{\varepsilon}$.

Empirical constants c_μ = 0.09; σ_k = 1.00; σ_ε = 1.30; $C_{\varepsilon 1}$ = 1.44; $C_{\varepsilon 2}$ = 1.92 determined experimentally. For the turbulent numbers of Prandtl and Schmidt were taken as 0.9.

A generalized equation of the transport value in a turbulent flow will then be:

$$\frac{\partial}{\partial t}\left(\rho\Phi\right)=-\frac{\partial}{\partial x_j}\left(\rho u_i\Phi\right)+$$
$$+\frac{\partial}{\partial x_j}\left[\Gamma_{\varphi,eff}\frac{\partial\Phi}{\partial x_j}\right]+S_{\varphi}$$

High-temperature media emits heat during combustion. As a result this thermal energy is transformed into radiant energy on the surface of the heated body. Thus, in the heat and mass transfer studies in the presence of combustion in the energy equation (i.e. heat transfer) should be considered the heat exchange by radiation too. On the heat exchange by radiation has a major influence of the water vapor and carbon dioxide. In modeling of flows heat exchange by radiation can be treated at temperatures 500 K < T < 2000 K in the region of the visible and infrared parts of the spectrum. The emissivity of the gas mixture consists of components emissivity, and depends on the partial pressure, temperature and wavelength.

To determine the intensity of the radiation used the six-flow model in this study [20]. It allows approximating the intensity of the radiation with the help of the wall rows by the solid angle:

$$I=A_x(\vec{i}\,\Omega)+A_y(\vec{j}\Omega)+A_z(\vec{k}\Omega)+$$
$$+B_x(\vec{i}\,\Omega)^2+B_y(\vec{j}\Omega)^2+B_z(\vec{k}\Omega)^2+.....$$

This model has been used in the calculation of radiation heat transfer in combustion chambers and showed good agreement with the experimental data.

Physical and chemical processes occurring in the combustion chamber are rapid and complete processes of oxidation of the fuel (in this case high-ash content coal) take place at high temperatures, accompanied by a large release of energy due to chemical reactions and changes in the concentrations of all substances interact. To describe real physical transformations that occur during combustion of fuel, it is necessary to choose an adequate numerical model [21-24] of physical process. Chemical reactions, which in turn determines the source terms in the equations for energy and the substance components. In this paper adopted a chemical model, which takes into account only the key components of the reaction. A Mitchell-Tarbell model [25] is used, which takes into account the rank of coal for modeling nitrogen-containing components (in this case for the Kazakh coal ash content is 35.1%).

It was used one-step model of pyrolysis, when the change in the concentration of carbon described by the ordinary differential equation:

$$\frac{dc}{dt}=-k_{pyr}c,$$
$$k_{pyr}=k_{0pyr}T^n e^{-E_{pyr}/RT}.$$

The rate of combustion of volatiles ω_{Vol} associated with the energy of turbulence k and its dissipation ε. For areas with a small amount of fuel and sufficient content of oxidizer, it have:

$$\omega_{1Vol}=c_1\overline{c}_{Vol}\frac{\varepsilon}{k}.$$

For areas with sufficient amount of fuel reaction rate is determined by the stoichiometry coefficient ν_{O_2Vol}:

$$\omega_{2Vol} = C_2 \frac{\overline{c}_{02}}{\nu_{O_2Vol}} \frac{\varepsilon}{k}.$$

For areas with sufficient fuel and oxidant:

$$\omega_{3Vol} = C_{3Vol} \frac{\overline{c}_{CO_2} + \overline{c}_{H_2O}}{\nu_{O_2Vol} + 1} \frac{\varepsilon}{k}.$$

From these three speed, the minimum speed of volatile combustion in the actual process is established:

$$\omega^*_{Vol} = \min(\omega_{1Vol}, \omega_{2Vol}, \omega_{3Vol}).$$

where $C_1 = 4.0$, $C_2 = 4.0$, $C_3 = 2.0$.

The carbon C burning rate determined by the diffusion of oxygen into the pores of the solid particles and reactions on its surface:

$$k_C = \frac{k_C^{(D)} k_C^{(chem)}}{k_C^{(D)} + k_C^{(chem)}},$$

$$k_C^{(D)} = \frac{2\nu_c DM_c}{RT_m d_P}.$$

According to the Arrhenius law constant chemical reaction rate will be equal to:

$$k_C^{chem} = k_{0C} \exp(-E_C / RT).$$

The Mitchell-Tarbell model demonstrates the formation of nitrogen oxides NOx by the oxidation of fuel bound nitrogen. The kinetic scheme takes into account the reaction of the primary pyrolysis, homogeneous combustion of hydro carbonaceous compounds, heterogeneous combustion of coke and formation of nitrogen compounds by thermal and fuel NOx mechanisms. The last ending nitrogen centers considered in this model by subsystem of CN (HCN, CN et al.). The most important overall chemical reactions involved in NOx formation during coal combustion hypothesized to be those shown in Figure 1.

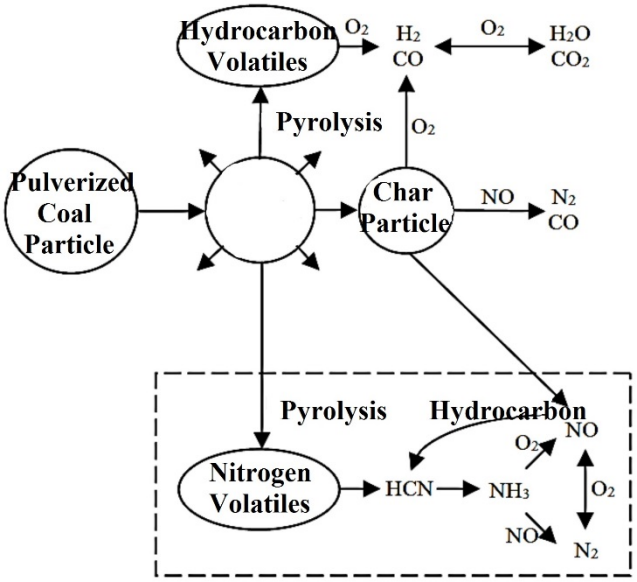

Figure 1 – Schematic Mitchell-Tarbell kinetic model

To avoid mistakes that can lead to a physically meaningless result, an adequate initial and boundary conditions corresponding to real physical process given. As an object of research chosen the combustion process of Kazakh coal in combustion chamber of the real energy facility (boiler BKZ-75 of Shakhtinsk TEC in Kazakhstan). All conditions taken into account of the real process of fuel combustion. For conducting numerical modeling were used control volume method [26-27], where in

computational experiment the chamber has been divided into 126 496 cells.

Results of numerical modelling

Following shown results of three-dimensional modeling of heat and mass transfer processes during combustion of pulverized low-grade coal in real conditions of combustion chamber of boiler. Aerodynamic pattern of motion of two-phase turbulent flow of pulverized coal combustion causes the heat and mass transfer process in general [28-30]. Figure 2 shows a two-dimensional graph of the full velocity vector, determined by the relationship: $\vec{V} = \sqrt{U^2 + V^2 + W^2}$. In the direction of camera output speed of flows decreased. The peak area values with maximum speed is clearly visible, which is equal to about 20 m/s. There at 4 meters by height of chamber located the combustor burners, and fed the fuel and oxidant mixture into the camera at maximum speed. Distribution character of flow velocity in height due to the vortex transfer of reacting medium and depending on the geometrical design of the chamber at all. At the outlet of chamber, it seen that velocity has a maximum value 8.76 m/s at section X=7.0 m and an average value not exceeding the 5 m/s by height.

There is a maximum perturbation of the turbulence characteristics in the vortex region, which cause the biggest change of velocity (Figure 3). Available surroundings of vortical flow in the central region of the combustion chamber are beneficial to the process of burning pulverized coal (heat exchange and mass transfer).

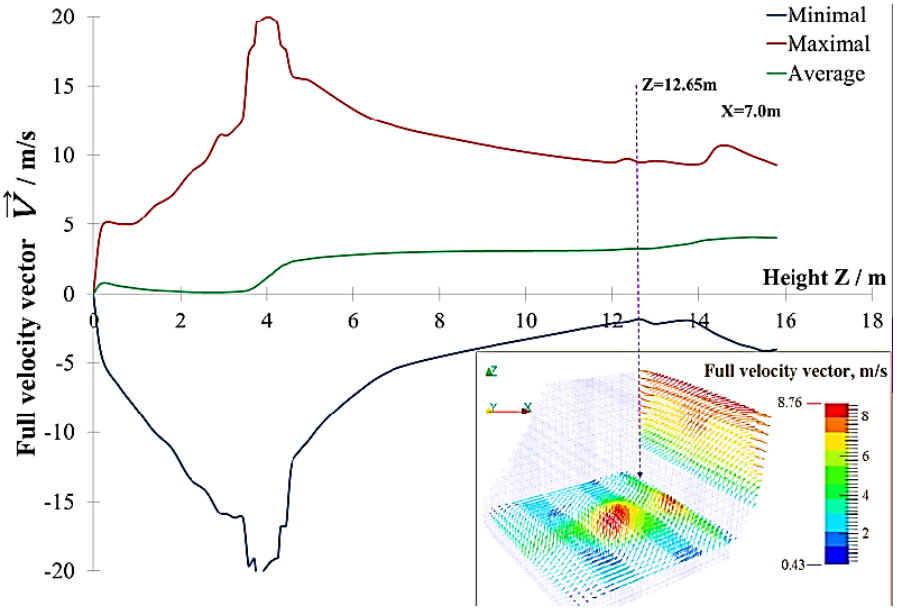

Figure 2 – Distribution of full velocity vector

Figure 4 shows the distribution of maximum, minimum and average values of the temperature field in the combustion chamber. There is also observed a sharp decrease in the temperature of fuel feeding zone. This is because the fuel supplied by a lower temperature. It can be seen that temperature values reach their maximum values in the area below a girdle of the burners where located torch core (approximately at 3 meters). This is because in this area the eddy currents (from installed four burners: on 2 burners on two opposite tiers) have a maximum convective transfer that increases the residence time of coal particles in here. As a result, in this area observed temperature rise to ~1370 ºC. In addition, at the output of the chamber maximum value of temperature is about 900-950 ºC. This clearly seen from the 3D picture placed in the right corner of the figure. In the figure also presented the point of the theoretically calculated value of the temperature of exhaust gases in the output of the chamber defined according to the normative method of thermal calculation [31] and data from the natural experiments held in real TPP of RK [32].

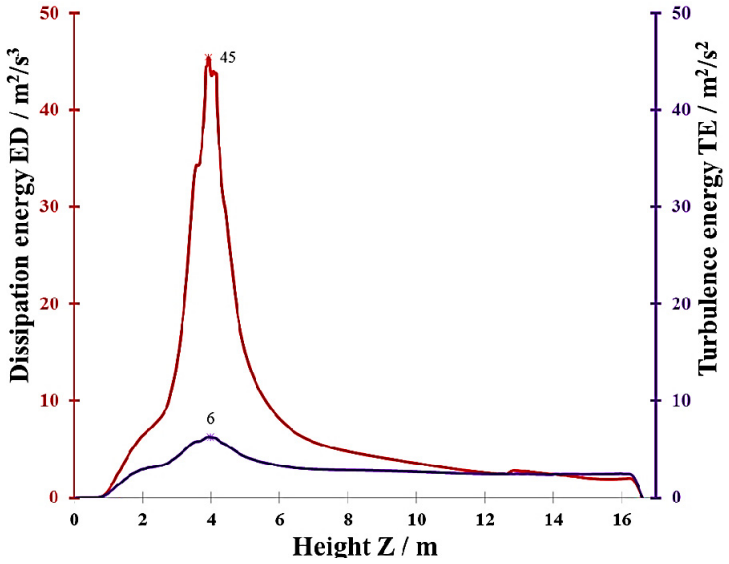

Figure 3 – 2D distribution of turbulence characteristics

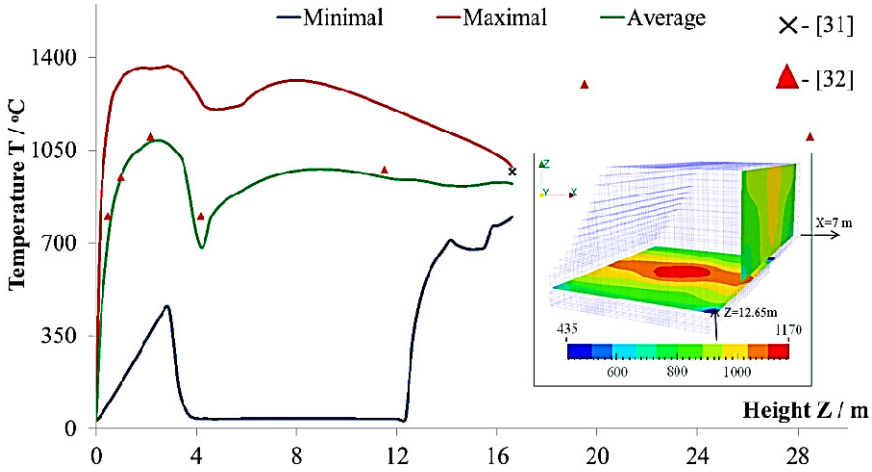

Figure 4 – Distribution of temperature fields and its verification with known data

The method of thermal calculation in power engineering is still the most reliable for finding the temperature at the outlet of the combustion chamber. It is seen that the difference between the results of numerical calculation is small and is only 4.7%. This proves that the method of 3D modeling gives good description of real processes of heat and mass transfer of fuel combustion. The verification results show the good conformity with calculated results.

The following Figure 5, which shows the 3D temperature distribution by the chamber sections, observed the same character as in the previous Figure 4. Temperature values by the height of the combustion chamber monotonically fall. From 3D distribution it is seen that the core of flame is located in the lower part of chamber in the section Y=3.19 m. Moreover, there the maximal value of temperature is equal to 1340ºC. Temperature fields are decreased by the height of camera. So temperature has the value in average 940ºC in section Z=12.65 m, when it has 922ºC at the section Z=7 m (the output of chamber).

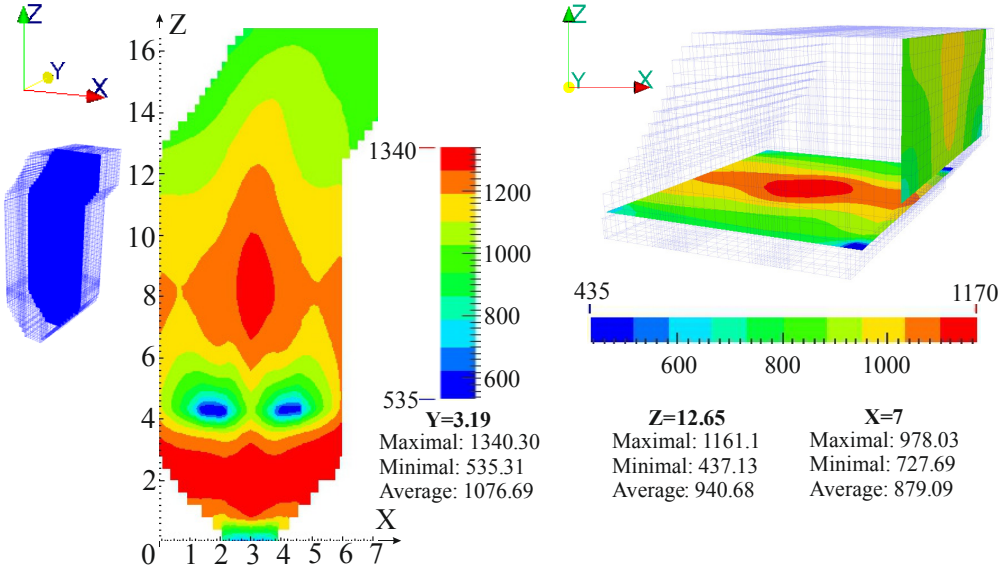

Figure 5 – 3D temperature distribution by the chamber sections

Below shown the results of 3D modeling of carbon dioxide CO_2 and nitrogen oxides NOx concentration distributions. Carbon mono oxide CO reacts with oxygen completely and so formed its dioxide CO_2. Concentrations of carbon dioxide CO_2 have their largest amount at the top areas of chamber (section Y=3.19 m). And the minimal values are observed at the region, where the burner equipment is set. From the figure 6 at the section Y=3.19 m it is seen that concentration of carbon dioxide CO_2 has the minimal value equal to 0.0089 kg/kg. In addition, in average it raised to ~ 0.13 kg/kg at the Z=12.65 m section by height and ~ 0.15 kg/kg at the outlet of the chamber (section X=7.0 m).

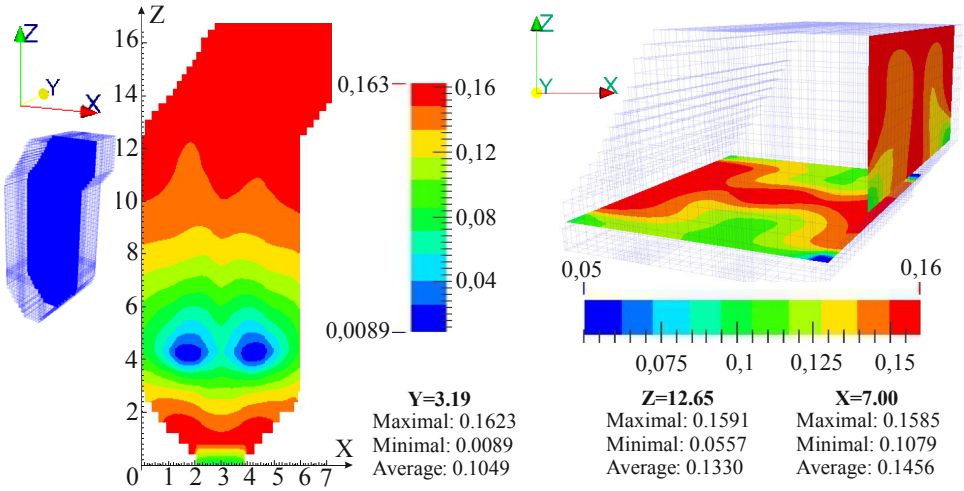

Figure 6 – 3D distribution of the carbon dioxide concentrations on sections of the chamber (CO_2, kg/kg)

Nitrous oxides NOx are formed by seven main nitrous compounds, but because of the small portions of them, except of nitrous mono- NO and dioxides NO_2 (in total NOx), we negligible others. So it could be seen that the maximal amount of nitrous oxides NOx concentrations 0.0109 kg/kg presented at the

burners zone (Figure 7, section Y=3.19 m). It caused with the fuel-N compound mechanism of NOx formation. Where with height of boiler, it shown decreasing of nitrous oxides concentration. And it has the average value equal to 5.09·10-12 kg/kg at the output of the combustion volume (section X=7.0 m).

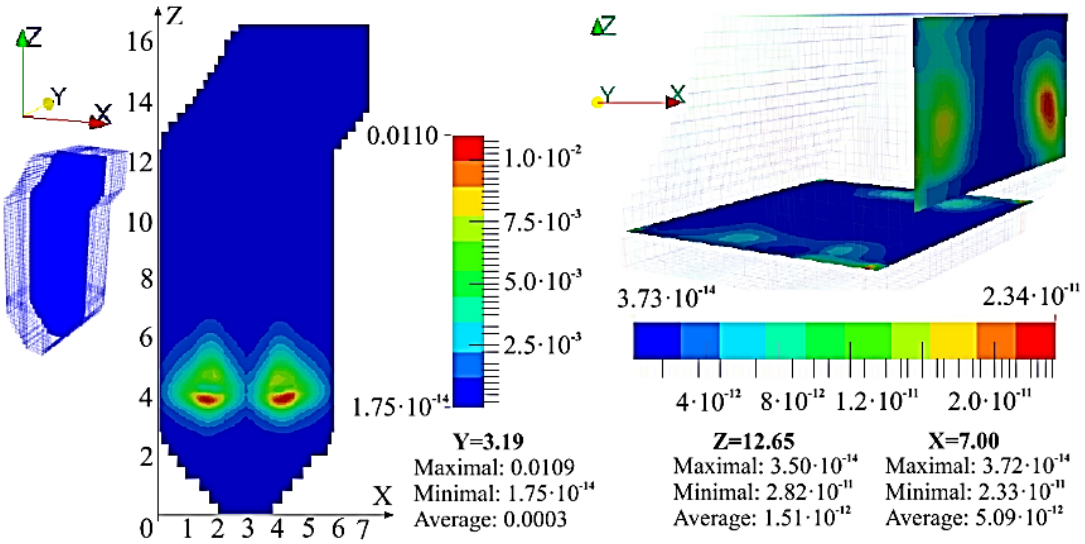

Figure 7 – 3D distribution of the nitrogen oxides concentrations on sections of the chamber (NOx, kg/kg)

These concentration distributions of carbon dioxide and NOx verified with the known data as shown in Fig. 8.

Concentrations of carbon dioxide CO_2 (a) and nitrogen oxides NOx (b) are in a good agreement with experimental data, received from real thermal power plant equipment [32]. Moreover nitrogen oxides NOx concentrations limit value for Kazakhstan Republic TPP's is given [33]. By comparisons of numerical experiment results held in this work with natural data from TPP, it noticed that the difference is for carbon dioxide CO_2 is 4 % and for nitrous oxides NOx is 5 %. So, considering results obtained in this paper we can propose the observed method of research of combustion processes is reliable and valid sufficiently to be useful in studying of low-grade coal combustion technological processes in energy objects.

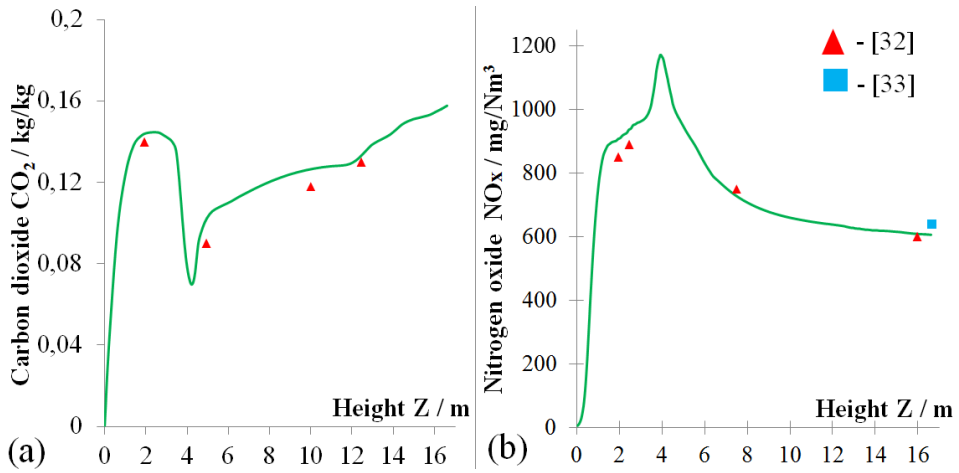

Figure 8 – Verification of calculation results with known data [32, 33]

Conclusion and perspectives

In conclusion, with computational research of combustion and modelling of heat and mass transfer processes determined velocity characteristics of turbulent flows, their turbulent kinetic energy and dissipation energy. Aerodynamic characteristics shows that intensive mixing of fuel and oxidant held in the central part of the chamber. In addition, it caused the increasing of temperature values to 1370ºC in core of torch and monotonically decreased to 922ºC at the outlet. Formation of hazardous substances as carbon and nitrous oxides (CO_2, NOx) are depends on their chemical interaction with oxygen. Carbon dioxide has its maximal values at the outlet of the chamber (~ 0.16 kg/kg), and the nitrous oxides have the maximal amount of ~ 1200 mg/Nm^3 at the burners' zone. Obtained results of numerical experiments have great theoretical and practical importance, as it will allow improve the design of combustion chambers and burners, to optimize the process of burning of high-ash content energy coal of Kazakhstan Republic.

Acknowledgment

This work supported by the Ministry of Education and Science of the Republic of Kazakhstan under the International Program of sub-priority "International Cooperation with China" (MT / 2013-2015).

References

1. Williams F. *Combustion theory*. California: Westview Press, 1985. – 704 p.

2. Zarrouk S.J., O'Sullivan M.J., St George J.D. "Modelling the spontaneous combustion of coal: the adiabatic testing procedure." *Combustion Theory and Modelling* 10, no. 6 (2006): 907-926.

3. Kez V., Consalvi J.L., Liu F., Ströhle, J., Epple, B. "Assessment of several gas radiation models for radiative heat transfer calculations in a three-dimensional oxy-fuel furnace under coal-fired conditions." *International journal of thermal sciences*. 120 (2017): 289-302.

4. Wu H.D., Han W., Wang D.D., Gao L. "A carbon oxidation factor regression model of coal-fired power plants in China." *Journal of cleaner production*. 142 (2017): 4403-4411.

5. Askarova A.S., Bolegenova S.A., Bolegenova S.A., Maximov V.Y., Beketayeva M.T. "Influence of boundary conditions to heat and mass transfer processes." *International journal of mechanics* 10 (2016): 320-325.

6. Askarova A., Bolegenova S., Safarik P., Maximov V., Beketayeva M. "Numerical Modeling of Pulverized Coal Combustion at Thermal Power Plant Boilers." *Journal of thermal science* 24, no. 3 (2015): 275-282.

7. Askarova A.S., Lavrichsheva Y.I., Leithner R., Müller H., Magda A. "Combustion of low-rank coals in furnaces of Kazakhstan coal-firing power plants." *VDI Berichte* 1988 (2007): 497-502.

8. Law Ch. K. *Combustion Physics*. Cambridge: Cambridge University Press, 2006. – 742 p.

9. Xu W., Kun L. "Analysis of pulverized coal flame stabilized in a 3D laminar counterflow." *Combustion and Flame* 189 (2018): 106-125.

10. Wieckowski L., Krawczyk P., Badyda K. "Numerical investigation of temperature distribution in the furnace of a coal fired grate boiler in part load conditions." *Journal of power technologies* 97, no. 5 (2017): 359-365.

11. Askarova A.S., Heierle E.I., Bolegenova S.A., Manatbayev R., Maximov V.J., Beketayeva M.T., Yergaliyeva A.B. "CFD study of harmful substances production in coal-fired power plant of Kazakhstan." *Bulgarian Chemical Communications* 48 (2016): 260-265.

12. Lazar J., Haugen N., Kruger J., Szlek A. "Numerical Study of Hydrogen Inhibition of Char Gasification Using Detailed Hetero- and Homogeneous Chemical Kinetics." *Energy & fuels* 30, no. 6 (2016): 4411-4418.

13. Buchmayr M., Gruber J., Hargassner M., Hochenauer C. "A computationally inexpensive CFD approach for small-scale biomass burners equipped with enhanced air staging." *Energy conversion and management* 115 (2016): 32-42.

14. Zhao Z.L., Tang H.Q., Quan Q., Zhang J., Shi S. "Simulation Study on Performance of Novel Oxygen-coal Lances for Pulverized Coal Combustion in Blast Furnace Tuyere." *Procedia Engineering* 102 (2015): 1667-1676.

15. Taraba B., Michalec Z., Michalcova V., Blejchař T., Bojko M., Kozubková M. "CFD simulations of the effect of wind on the spontaneous heating of coal stockpiles." *Fuel* 118 (2014): 107-112.

16. Muller H. *Numerische Simulation von Feuerungen.* Braunschweig: IWBT, 1997. – 8 p. (in German).

17. Leithner R., Müller H. "CFD Studies for Boilers." *Second M.I.T. Conference on*

Computational Fluid and Solid Mechanics, Cambridge, 2003. – 172 p.

18. Launder B., Spalding D. "The numerical computation of turbulent flows." *Comp. Meths. Appl. Mech. Eng*. 3 (1974): 269–289.

19. El-Mahallawy L., El-Din Habik S. *Fundamentals and technology of combustion*. Oxford: Elsevier Science: Energy, 2002. – 839 p.

20. De Marco A., Lockwood F. "A new flux model for the calculation of radiation furnaces." *La rivista dei combustibili* 29 (1975): 1-13.

21. Choubey G., Pandey K.M. "Effect of variation of inlet boundary conditions on the combustion flow-field of a typical double cavity scramjet combustor." *International journal of hydrogen energy* 43 (2018): 8139-8151.

22. Adamczyk W.P., Myöhänen K., Hartge E.U., Ritvanen J., Klimanek A., Hyppänen T., Białecki R.A. "Generation of data sets for semi-empirical models of circulated fluidized bed boilers using hybrid Euler-Lagrange technique." *Energy* 143 (2018): 219-240.

23. Li G., Gu F., Wang T., Yang T., Ball A. "Investigation into the dynamic response of cylinder liners in an IC engine based on a validated finite-element model." *Systems science & control engineering* 5, no. 1 (2017): 56-69.

24. Benard P., Balarac G., Moureau V., Dobrzynski C., Lartigue G., D'Angelo Y. "Mesh adaptation for large-eddy simulations in complex geometries." *International journal for numerical methods in fluids* 81, no. 12 (2016): 719-740.

25. Mitchell J.W., Tarbell J.M. "A kinetic model of nitric oxide formation during pulverized coal combustion." *AIChE Jornal* 28 (1982): 302-320.

26. Ali H., Askri E., Ben Nasrallah S. "Comparative study of WSGG and SLW models coupled with control volume finite element method for nongray radiation prediction." *International journal of thermal sciences* 113 (2017): 73-82.

27. Madejski P., Taler D., Taler J. "Numerical model of a steam superheater with a complex shape of the tube cross section using Control Volume based Finite Element Method." *Energy conversion and management* 118 (2016): 179-192.

28. Bhuiyan A.A., Karim M.R., Hart J.T., Witt P. J., Naser J. "Investigation of Slot-Burner Aerodynamics with Recessed-Type Nozzle Geometry." *Fluids* 1, no. 2 (2016): 10.

29. Alekseenko S.V., Anufriev I.S., Glavniy V.G., Krasinsky D.V., Rakhmanov V.V., Salomatov V.V., Shadri E.Y. "Study of 3D flow structure and heat transfer in a vortex furnace." *Heat transfer research* 47, № 7 (2016): 653-667.

30. Bhuiyan A.A., Amin M.R., Naser J., Islam A.K.M. "Effects of geometric parameters for wavy finned-tube heat exchanger in turbulent flow: a CFD modeling." *Frontiers in heat and mass transfer* 6 (2015): 013005.

31. *Teplovoi raschet kotlov: Normativnyi metod*. (*Thermal calculation of boilers: Normative method*). SPb.: NPO CKTI, 1998. – 256 p.

32. Aliyarov B.K., Aliyarova M.B. *Szhiganiye kazakhstanskikh ugley na TES i na krupnykh kotelnykh: opyt i perspektivy. (Combustion of Kazakhstani coal at TPPs and large boiler plants: experience and prospects)*. Almaty: Gylym ordasy, 2011. – 304 p.

33. RND 34.02.303-91 *Otraslevaya instruktsiya po normirovaniyu vrednykh vybrosov v atmosferu dlya teplovykh elektrostantsiy i kotel'nykh.* (*Industry guidelines for the regulation of harmful emissions into the atmosphere for thermal power plants and boilers*). Astana: MOOS RK, 2004.

IRSTI 29.27.51

[1,2*]Zhukeshov A.M., [1,2]Gabdullina A.T., [1,2]Amrenova A.U.,
[3]Batani D., [2]Mukhamedryskyzy M., [2]Moldabekov Zh.M.

[1]National Nanotechnology laboratory of open type, al-Farabi ave. 71, 050040, Almaty, Kazakhstan
[2]Al-Farabi Kazakh National University, al-Farabi ave. 71, 050040, Almaty, Kazakhstan
[3]Center intense lasers and applications, University Bordeaux 1, 351 Liberation sq., Bordeaux, France
e-mail: zhukeshov@physics.kz

The nanodimension crystallite formation in steel surface after pulsed plasma flow action

Absract. This paper presents the analysis of structural-phase changes in samples of stainless steel AISI 321 (12Х18Н10Т) and AISI 201 (12Х15Г9НД), treated by pulsed plasma flows on coaxial plasma accelerator KPU-30. Studied the sequence of phase transitions in modified layers depending on a frequency of treatment. It is shown that after treatment with a small number of shots (n = 2) in the stainless steel samples occurs plasma etching and redistribution of crystallites. At tenfold (n = 10) processing the structure of the surface layer becomes more ordered, appear nanoscale columnar blocks evenly spaced on the surface and their tracks are located mainly at the grain boundaries. The results of SEM and AFM analysis showed the presence of surface melting; this suggests probable structural and phase changes during plasma processing. Changes in the structure of the investigated structural steels, associated with the formation of new phases and the microscopic strains in the crystal lattice, studied by XRD method.
Key words: stainless steel, microstructure, nanoscale inclusions, plasma processing, pulsed plasma accelerator.

Introduction

In modern production, high requirements placed on technological and operational characteristics of construction materials. Currently, the most common among structural materials remain metallic materials. Therefore, the problem of improvement of technological methods of hardening of structural steels, including nanoscale structural modification is relevant.

As it is known, processing of pulsed plasma flows has a number of advantages in comparison with traditional technological processes of thermal-mechanical and chemical-thermal treatments, and methods of exposure based on the use of other types of concentrated energy flows, including laser radiation, high-current electron and ion beams, lasers, etc. [1-4].

The technologies of surface hardening based on a modifying effect on the metal surface by energy or physical-chemical methods, which radically changes its structure and properties [5-11]. Pulsed plasma treatment is one of the most effective ways of modifying the surface of a solid body.

Earlier in the works [12, 13] have been analyzed changes in the structure of steel and stainless steel were processed on the accelerator KPU-30. In ordinary carbon steels observed strong reduction of the crystallites size with increasing energy, but in stainless steels this is not happening. Furthermore, the iron nitride when exposed to nitrogen plasma uniquely identified only in stainless steel. Thus, to find out the reason of hardening materials, it is necessary to conduct research on materials that combine the properties of carbon and stainless steel and manufactured with the same technology. Stainless steel AISI 201, in which expensive nickel to stabilize the austenitic structure partially replaced by manganese and nitrogen, has long established itself as an effective substitute for the standard chromium-nickel steels. This paper presents the analysis of structural-phase changes in the structural

 Printed in Kazakhstan

steel samples processed by pulsed plasma streams of stainless steels AISI 201 and AISI 321.

Experiment details

Samples of the test material were exposed to pulse treatment on coaxial plasma accelerator KPU-30 with a residual air pressure of 13,3 Pa. At a voltage of 20-22 kV, the energy density of the plasma flow varied in the range of 14,2 ÷ 15,4 J/cm^2. During the experiment, the samples were placed in the working chamber at a distance of 7 cm from the end of the center electrode in the area of plasma focus.

Using atomic force microscopy (AFM) it is possible to descry in detail the topography of the surface in two forms images on the plane and in 3D format. Thus, obtained spatial images of three different areas. Figure 1 shows the AFM images of the surface of steel samples AISI 201 and AISI 321, exposed the twofold influence of plasma flow.

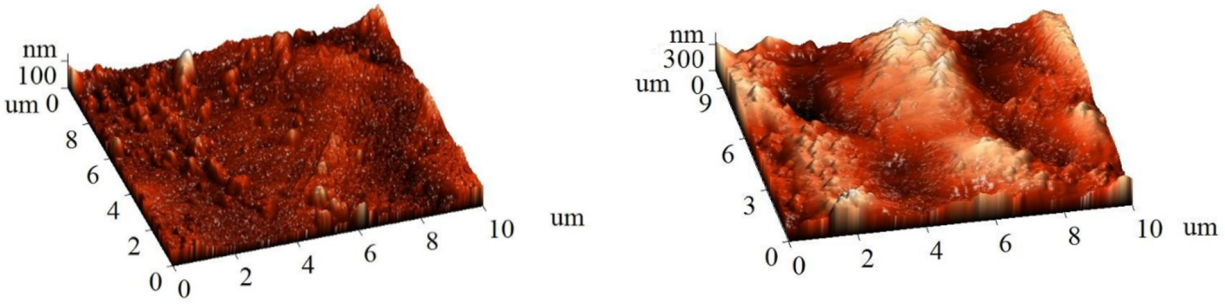

a b

Figure 1 – The AFM images of the surface of steel samples AISI 201(a) and AISI 321 (b)

As shows data analysis of steel AISI 201, the melting of the surface at twofold action leads to the local formation of blisters, also there are areas with columnar crystallites, which formed in a perpendicular direction to the surface (Fig. 1a). Tenfold treatment leads to an increased efficiency of the double treatment, and the columnar crystallites moved predominantly to the grain boundaries (blocks). The paper presents quantitative estimates of the size of crystallites. The AFM analysis of processing results of steel AISI 321 showed that, in contrast to steel AISI 201, the height of the columnar crystals are more than for steel AISI 201, already at twofold treatment (Fig. 1b), but, as well as in case of AISI 201 (n = 10), the columnar crystallites are mainly located at the grain boundaries. In some parts of the steel AISI 321 and as well as in the steel AISI 201 traces of the formation of blisters. Furthermore, for this grade of steel samples were not detected traces of delamination surface that, apparently, it is not typical for this steel. According to the preliminary results, we can conclude that under certain parameters of the plasma exposure, the modification of the surface structure of structural steel by fusion, accompanied by destruction of the crystal bonds and plasma etching.

To determine the changes in physical and mechanical properties presented studies of the microhardness on metallographic microscope “METAVAL” by Vickers method. Measurements of surface microhardness of the steels AISI 201 and AISI 321 processed by pulsed plasma streams carried out on all three areas with different surface topography.

Experimental data analysis

Comparing the results of measuring the microhardness in different areas of the twice treated surface with the original, it was found that surface hardening is uneven, with the presence of local areas with both elevated and reduced hardness. Comparing these areas with the results of the AFM analysis, in the first case, the decrease of hardness corresponds to "delamination" of the surface (1st area), in the second case - blister formation (2nd area), and in the third case, the increase of microhardness can be associated with a "leveling" of the surface and streamlining of placing the columnar

crystallites over the entire surface area (3^d area). As a result of the tenfold processing, as shown by measurements, the surface hardening at all three areas increases slightly (~ 100 MPa), thus there are areas where the microhardness is very unstable (3^d area). Comparing with the results of the AFM analysis, we can assume that this may be due to the redistribution of columnar crystallites (a preferential distribution at the grain boundaries) and increase their size (height). Microhardness measurements of the steel AISI 321, performed after double treatment, showed its reduction from baseline to a significantly greater extent than for steel AISI 201. The results of tenfold treatment, on the contrary, show that typical growth of microhardness is more significant for AISI 321 (to ~ 150 ÷ 300 MPa) than in the previous grades of steel, but the average microhardness is much less than earlier obtained data [7,9]. Perhaps, this is due to the formation of block structure, typical for plasma etching.

Data analysis by average values of surface microhardness of both grades examined steels showed that, on average, a greater growth of microhardness is typical for AISI 321 (n=10). Despite the fact, that changes in microhardness insignificant, however, they take place, moreover, the results of SEM and AFM showed the presence of surface melting, this suggests probable structural and phase changes during plasma processing.

Data for pulse plasma treatment of stainless steel grades AISI 201 and AISI 321 are given in table 1. In the initial state the samples of carbon steel were monophasic, but in this case, monophasic ferrite with lattice parameter a = 2,8686 ± 0,0007 Å (according to the standard diffractometric data parameter of iron equal to a = 2,8664 Å) (table 1).

Table 1 – The data of RSA tenfold processed steel grades AISI 201 and AISI 321

Sample status	n	Phase		a, Å	L, Å
Data for AISI 201 (12Х15Г9НД)					
Untreated	0	monophase	(Fe,C) austenite	3,6057 ± 0,0006	–
Treated	10	multiphase	(Fe,C) austenite	3,5958 ± 0,0006	1900
			($FeN_{0,076}$) iron nitride	3,6263 ± 0,0007	270
Data for AISI 321 (12Х18Н10Т)					
Untreated	0	monophase	(Fe,C) austenite	0,35824 ± 0,00006	156,0
Treated	10	multiphase	(Fe,C) austenite	0,35873 ± 0,00006	35,0
			($FeN_{5,6}$) iron nitride	0,36113 ± 0,0004	16,3

Sample steel AISI 201 has two phases. One of these phases belongs to austenite with the lattice parameter a = 3,5958 ± 0,0006 Å. The parameter of austenite is somewhat less than the initial sample, which may be associated with distortion of the crystal lattice of steel during plasma treatment. The second phase belongs to iron nitride $FeN_{0,076}$ with the lattice parameter equal to a = 3,6263 ± 0,0007 Å. On a comparison between intensities of diffraction lines of iron nitride and austenite for the same planes, we can conclude that the nitride is not the dominant phase. It is possible that the iron nitride is in the surface layer, and the austenite is a little deeper. In this case, the thickness of the nitride is small. Therefore, the data X-ray structural analysis confirmed the possibility of increasing of the microhardness after processing the surface of a material with a pulsed plasma. Thus, the surface hardening can be connected with a formation in the investigated steel new phase $FeN_{0,076}$ as was assumed in earlier works [7-9].

As a result of tenfold processing steel AISI 321 by plasma flows at a pressure of 13,3 Pa detected new phases – iron nitride $FeN_{5,6}$,and possibly iron carbide Fe_3C. The number of lines Fe_3C is extremely small for identification. As you can see, there is a broadening of the lines belonging to the iron nitride, in comparison with the lines of the austenite. The broadening of the lines of iron nitride is associated with distortion of nitride lattice, the degree of distortion, which increases with increasing frequency of treatment. According to the X-ray analysis, shown in table 1, the crystallite size of the austenite is reduced more than in 4 times with frequency of treatment n=10 in comparison with the untreated AISI 321. In addition, after ten times of treatment, the size of crystallites of both phases are identical. Therefore, multiple pulse plasma processing the most effective for the grinding of the

austenite crystallites and, in particular, of iron nitride as in the case of steel AISI 201.

Conclusion

According to the results of work, we can conclude that the treatment with pulsed plasma flows leads to a change of physical and mechanical properties owing to the structural-phase changes and defect formation, which confirmed by the following analysis methods. The results of SEM analysis revealed that after treatment plasma etching takes place, and a redistribution of the crystallites. With increasing the frequency of treatment by pulses of plasma (n=10) the etching pattern becomes more intense, and for steel AISI 321 has been identified already at double treatment in comparison with steel AISI 201.

The AFM analysis revealed that the surface of test material at twofold treatment detected traces of blister formation, the presence of layered structure and tracks, the formation of columnar structures, which may be due to the planar and linear defects. At tenfold processing, the structure is more ordered, columnar blocks arranged relatively uniformly over the surface and their tracks are located mainly at the grain boundaries.

The results of metallography, we can conclude that with multiple treatments (n=10) samples, the surface hardness is increased, and for the second type of steel (AISI 321), the effect is more pronounced than for the other (AISI 201), which is consistent with the results of the SEM analysis.

All the above is confirmed by X-ray diffraction analysis, which revealed changes in structure of the investigated steels, is related to the formation of a new phase of iron nitride and the microscopic strains in the crystal lattice that may be responsible for hardening.

In general, by the results of performed work, it concluded that treatment with pulsed plasma flows leads to a change of physical and mechanical properties at the nanoscale, and this could be due to structural phase changes and defect formation. Furthermore, the results of SEM analysis revealed that after treatment plasma etching, the formation and redistribution of nanosized crystallites take place.

Acknowledgments

The studies presented in this paper was conducted under the applied research grant No 3111 GF 4/2017.

References

1. Lieberman M.A., Lichtenberg A.G. *Principles of plasma discharges and materials processing*. New York: John Wiley & Sons Inc, 1994. – 450 p.

2. Gribkov V.A., Grigor'ev F.I., Kalin B.A., Yakushin V.L. *Perspektivnye radiatsionno-puchkovye tekhnologii obrabotki materialov*. (*Perspective radiation-beam technologies of material processing*). Moscow: Krugly God, 2001. – 501 p.

3. Kalin B.A. "Perspective radiation-beam technologies for obtaining and processing materials." *Proceedings of the Moscow Engineering Physics Institute* (2003): 46-58.

4. Piekoszewski J. "Present status and future of pulsed plasma processing of materials in SINS." *Nukleonika* 45, no. 3 (2000): 193-197.

5. Richter E., Piekoszewski J., Wieser E., Prokert F., Stanislawski J., Walis L., Reuther H. "Modification of titanium surface by its alloying with silicon using intense pulsed plasma beams." *Surface and Coatings Technology* 158 (2002): 324-327.

6. Tomida S., Nakata K. "Fe–Al composite layers on aluminum alloy formed by laser surface alloying with iron powder." *Surface and Coatings Technology* 174-175 (2003): 559-563.

7. Tereshin V.I., Bandura A.N., Bovda A.M., Brown I.G., Byrka O.V., Chebotarev V.V., Garkusha I.E., Tortika A.S. "Pulsed plasma accelerators of different gas ions for surface modification." *Review of scientific instruments* 73, no. 2 (2002): 831-833.

8. Uglov V.V., Cherenda N.N., Anishchik V.M., Astashinskii V.M., Kvasov N.T. *Modikatsiya materialov kompressionnymi plazmen-nymi potokami*. (*Modification of materials by compression plasma flows*). Minsk: BGU, 2013. – 248 p.

9. Uglov V.V., Kuleshov A.K., Soldatenko E.A., Koval N.N., Ivanov Yu.F., Teresov A.D. "Structure, phase composition and mechanical properties of hard alloy treated by intense pulsed electron beams." *Surface and Coatings Technology* 206, no. 11–12 (2012): 2972-2976.

10. Bandura A.N., Garkusha I.E., Byrka O.V., Makhlay V.A. "Modification of structural materials by pulsed plasma flows." *Proceedings of the 9th IC "Interaction of Radiations with a Solid Body"* (2011): 186-189.

11. Chebotarev V.V., Garkusha I.E., Tereshin

V.I., Derepovski N.T. “Surface structure changes induced by pulsed plasma streams processing.” *Problems of atomic science and technology. Series: Plasma physics* 3, no. 3 (1999): 273-275.

12. Zhukeshov A.M., Gabdullina A.T., Amrenova A.U., Pak S.P., Moldabekov Zh.M., Mukhamedryskyzy M. “To the effect of pulsed plasma on the surface of stainless steel.” *Proceedings of the NAS of the RK, a series of physics and mathematics* 2 (2013): 71-74.

13. Zhukeshov A.M., Gabdullina A.T. “Influence of pulsed plasma treatment parameters on tribology of stainless steel.” *NNC RK Bulletin* 2 (2007): 28-31.

IRSTI 29.27.01

N.Kh. Bastykova[1,*], S.K. Kodanova[1], T.S. Ramazanov[1], Z. Donko[2]

[1]Scientific-Research Institute of Experimental and theoretical physics,
Al-Farabi Kazakh National University, Almaty, Kazakhstan
[2]Institute for Solid State Physics and Optics, Wigner Research Centre for Physics,
Hungarian Academy of Sciences, Budapest, Hungary
*e-mail: bastykova_nuriya@physics.kz

Manipulation of the plasma-dust layer in high-frequency discharge with an additional alternative phase

Abstract. In this paper, the properties of complex plasma and the manipulation of plasma-dust layer in high-frequency discharge with an additional alternative phase have been investigated. The computer simulation of the high-frequency capacitive discharge has been carried out under the influence of an additional alternative phase on the basis of the particle-in-cell and Monte Carlo (PIC / MCC) methods. The parameters describing the kinetic and transport properties (density and temperature of electrons, electron and ion heating rates) of complex plasma of high-frequency capacitive discharge have been obtained. The charging processes of dust particles, the forces acting on dust particles, as well as the equilibrium positions of the dust particles in the plasma have been studied. A method for manipulating particles of micro and nano sizes in a low-temperature complex plasma has been developed. The results have shown that the dust charge can be tuned by the properties of the excitation waveform and in connection with it we have suggested that the dust component of the plasma can be heated through a variation of the excitation waveforms via a mechanism similar to second-order Fermi acceleration.
Key words: Complex plasma, Radiofrequency discharge, Dust particles, Particle method in cells, Monte Carlo method.

Introduction

Complex (dusty) plasma is actively studied all over the world, both for a fundamental understanding of the dynamics of strongly coupled open systems [1-4] and for practical purposes [5-7]. In the laboratory, dust plasma is investigated in various types of gas discharge [8]. At the present time, the development of new technologies based on combined discharges [9] begins, in connection with which, studies on the behavior of complex plasma in such systems become relevant. The most important applications include etching and precipitation in the crystal, in the production of individual microcircuits, solar cells and the creation of biocompatible surfaces. Also of great interest is plasma in a high-frequency (RF) discharge at atmospheric pressure for medical applications [10-12]. These applications are very demanding and require research of discharge characteristics to optimize the interaction of plasma with the surface. Control of the ionic properties of plasma is a key issue, since most processes are caused by ions. The need to different types of plasma sources and excitation schemes: a capacitive discharge operating at different frequencies, as well as hybrid (DC-RF and capacitive inductive) sources [13-14]. In addition to their interest in these areas, a discharge with high-frequency voltage exhibits a complex physics that attracts much attention. The kinetics and mode of heating of electrons are key properties of the HF discharge, since they are the basis for multiplication of charges in order to balance losses in a stable state. To date, the development of plasma diagnostics and modeling methods allows carrying out and investigating these discharges.

Manipulation of individual dust particles and their ensembles is of great interest, both for a

theoretical understanding of the fundamental properties of strongly coupled systems and for practical applications. In recent years, considerable progress has been made in controlling dusty plasma by means of lasers [15-16] and by modifying external electric and magnetic fields [17].

In this paper, we present the results of computer simulation of complex plasma properties in a combined radio frequency capacitive discharge (RF) with an additional alternative phase.

Theoretical basis of particle in cell and Monte-Carlo methods

Particle in cell (PIC) is the most common simulation method for describing the kinetic and transport properties of complex plasmas. The method, which belongs to the particle-grid class, was introduced in the 1960s and developed significantly over the next decades [18-19]. The idea of using a computational grid avoids the need to take into account the pair interaction of all individual particles. Another approach is to use "superparticles", which are a large number of charged particles (electrons and ions). In [20], electromagnetic effects are described in the scheme of the particle in cells method, and then electrostatic effects are considered in this paper.

The Monte Carlo method (MCC) is usually used in the simulation of collisions at low pressure. The combination of particle in cells and Monte Carlo methods is called the PIC/MCC approach. The PIC/MCC simulation cycle consists of the following steps [21-22]:

(i) at each time step, the charge of the superparticles (which can be located anywhere within the discharge gap) is assigned to the grid cells;

(ii) Poisson's equation is solved on the grid: the potential distribution is calculated from the charge distribution taking into account the potentials (or currents) applied to the electrodes as boundary conditions;

(iii) the forces acting on the particles are obtained by interpolating the electric field (as a result of differentiating the potential) to the positions of the particles;

(iv) new positions and particle velocities are determined from the solution of the equation of motion;

(v) because of the finite volume of the plasma, the interactions of particles with surrounding surfaces (for example, reflections, absorption, secondary emission) are taken into account;

(vi) collisions of the traced charged particles with each other and with the atoms of the background gas are verified and performed. In the PIC / MCC simulation, elastic scattering, excitation and ionization processes for electrons are usually taken into account, and for cold-gas approximation, for electron-atom collisions. For ions, it is usually sufficient to take into account elastic collisions, with the exception of high voltages, where excitations and ionization can also occur during ion-atom collisions.

Following the recommendations of Phelps [23], the momentum transfer cross section of elastic collisions of ion on atom Q_m is divided into isotropic and backscattering $Q_m = 2Q_b + Q_i$. Recharging at collisions and backscattering cross sections were discussed in Ref. [24]. It can be noted that at high ion energies these cross sections are equal. A similar approach was developed in Ref. [25] regarding the anisotropic elastic scattering of electrons by heavy particles. Subsequently, they were used in studies of electron transport and ions [26].

It should be noted that the kinetic properties of the particle in cell method negatively affect for the reading of collisions [27-28]. Nevertheless, PIC/MCC simulation provides a detailed analysis of the processes in plasma physics, providing spatiotemporal distributions of the quantities of greatest interest: particle distribution functions, ionization and excitation rate, electron heating rate, and fluxes and particle densities of various species.

The Monte Carlo method for describing the transport properties of electrons. There are two ways to describe the behaviour of charged particles in the presence of external forces: the observation of particle trajectories between collisions and the second is the processing of collisions of particles with a background gas.

The motion of particles between collisions is determined by the equation of motion:

$$m\ddot{\mathbf{r}} = q(\mathbf{E} + \mathbf{v} \times \mathbf{B}), \quad (1)$$

where q and m are the charge and mass of particle, respectively, $\mathbf{E}$ and $\mathbf{B}$ are electric and magnetic fields. In our case $\mathbf{B} = 0$. The particle trajectories are obtained by integrating the discredited formula (1) in time t. While the definition of the trajectory of

particles between collisions is deterministic, the collisions are processed by a stochastic (probabilistic) method. And so this method was called "Monte Carlo". The approach relies on the generation of random numbers, which, however, have specific probability distributions based on physical principles. All events related to collisions should be described in the centre of mass system (CMS). Denoting through υ_1 and υ_2 both the velocities of the "incident" particle and the "target", respectively (in the laboratory (LAB) frame of reference m_1 and m_2 are their masses), the authors outlined the steps of the collision in simulation.

Check for a collision. The probability of a collision after a certain period of time Δt.

$$P(\Delta t) = 1 - \exp[-\mathrm{n}\,\overline{\sigma_T(\upsilon_r)\upsilon_r}\Delta t], \qquad (2)$$

Where σ_T is the total cross section, which includes the cross sections of all possible collision processes and $\upsilon_r = \upsilon_1 - \upsilon_2$ is the difference in the velocities of the collision participants. The average value $\overline{\sigma_T \upsilon_r}$ should be taken from the ensemble of atoms by the Maxwell distribution (temperature T_2) [29].

The approximation of cold gas is used in investigations, which assumes that the gas atoms are at rest (background); $\upsilon_2 = 0$. In this case υ_r becomes equal to the velocity of the electron υ_1. In connection with the large difference in the masses of the atoms and electrons, the collision in the laboratory system is the following approximation. The collision is calculated until the average electron energy is much higher than the thermal energy of the gas atoms. Or vice versa occurs only at very low values of the electric field strength.

In the cold-gas approximation ($\upsilon_2 = 0$ and thus $\upsilon_r = \upsilon_1$), the probability of collision during the time step Δt is determined by the following equation:

$$P(\Delta t) = 1 - \exp[-\mathrm{n}\,\sigma_T(\upsilon_1)\upsilon_1\Delta t]. \qquad (3)$$

The simplest Monte Carlo simulation approach is based on (I) moving the particle in accordance with the equation of motion for time Δt (updating the position and velocity vectors) and (II) verifying the occurrence of the collision using equation (3). In practice, it is necessary to choose Δt sufficiently small to realize the exact integration of the equation of motion and to withstand the probability of more than one collision, the motion of the particle will occur during a time step with a negligibly small value.

The results and discussions

The model is a one-dimensional (spatial) problem and considers 2 * 10^5 superparticles, which are electrons and argon ions. In this model, the interactions of charged particles with the surface of electrodes are taken into account in such processes as secondary electron emission and electron reflection from the surface.

The calculations are carried out for an RF discharge with a plane-parallel electrode configuration, with an electrode separation of L = 55 mm. The bottom electrode (situated at x = 0*)* is powered, while the top electrode (at $x = L$*)* is grounded. The excitation frequency is f_{RF} = 13.56 MHz. The buffer gas is argon, at a pressure of p = 1.8 Pa, and the dust particles are assumed to have a radius of r_d = 2.19 μm.

We consider the following types of driving voltage waveforms (see Fig. 1), with an amplitude of ϕ_0 = 100 V:

1) harmonic RF voltage excitation: $\phi(t) = \phi_0 \sin[2\pi f_{RF} t]$;

2) excitation of the discharge with alternating phase of the driving voltage with an additional dc bias, $\phi(t) = \phi_0 \sin[2\pi f_{RF} t + \sin[2\pi(2 \times f_{RF})t]] + \phi_{dc}$, where the phase of the RF voltage alternates as $\sin[2\pi(2 \times f_{RF})t]$, and ϕ_{dc} is the additional dc voltage.

Combination of the two methods (the phase modulation and additional dc bias) gives more flexibility in realizing a control of the spatial profiles of electron (ion) density (temperature) and the forces exerted on dust particles. In addition, as it is shown below, there is the possibility to control interdust particle interaction keeping the vertical position of them nearly the same. Latest opens the way for investigation into the different kinds of nonlinear processes like phase transitions.

In figure 2, the density profiles of the electrons and ions are shown for the three types of excitation waveform considered. The stronger electron heating following the fast sheath expansions in the case of the alternating-phase driving voltage leads to an increase by a factor of ~2.7 of the electron and ion densities in the plasma, compared with the harmonic RF excitation. The additional dc bias applied to the powered electrode (at x = 0) results in a decrease of the peak density and shifts the peak position of the

density profiles toward the grounded electrode, as a consequence of the increasing length of the dc-biased sheath at the powered electrode. These changes in the discharge characteristics modify the levitation height of dust particle as well.

Figures 3 (a) – 6 (a) show the spatiotemporal distributions of the characteristics of the plasma of a high-frequency discharge, where the distance between the electrodes (x / L) is shown vertically and the time step (t/T) along the horizontal line. Figures 3 (b) to 6 (b) show the spatiotemporal distributions of the characteristics of a high-frequency discharge plasma with an alternative phase, such as ionization and excitation rates, electric field and potential, charged particle density (electrons / ions), electron temperature, heating rates of charged particles (electrons / ions). In figures 3 and 4, the spatiotemporal profiles of the electron density and temperature, derived from the mean energy of electrons measured in the simulation, for the case of harmonic RF excitation and for the case of alternating phase excitation with no additional dc bias are shown, respectively. Comparing figures 4 (a) and 4 (b), one can see that the highest values of the effective electron temperature are found near the edges of the expanding sheaths. In the case of the (pure) harmonic excitation waveform, the highest values are in the order of ~4 eV, while in the plasma bulk we find ~2 eV. In the case of the alternating-phase excitation voltage, the electron dynamics changes considerably. The expansion of the sheaths becomes much faster, and consequently, the electron temperature rises to higher values compared with the case of the harmonic excitation. Here, T_e reaches values exceeding 5 eV, while in the bulk we observe similar values as in figure 4.

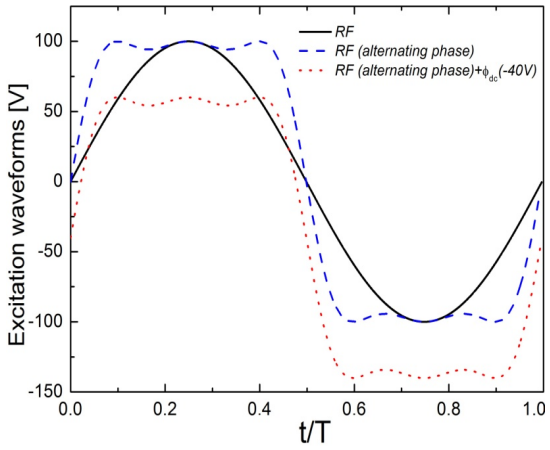

Figure 1 – Plasma excitation waveforms

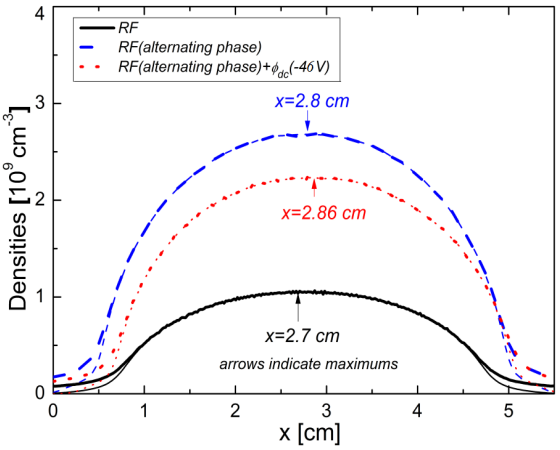

Figure 2 – Ion (thick lines) and electron (thin lines) density profiles for the different excitation waveforms

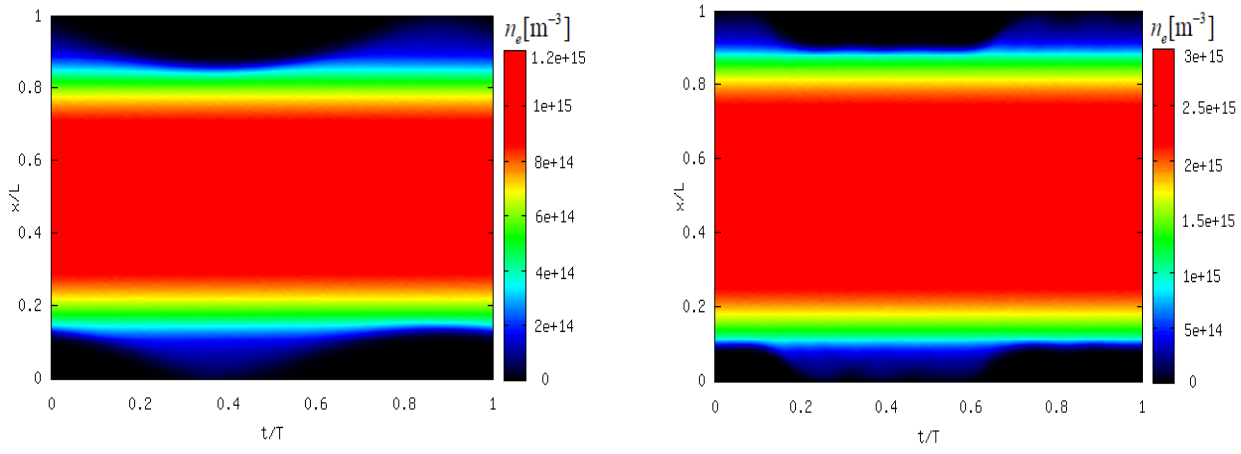

Figure 3 – Spatiotemporal profile of electron density in RF discharge (a) and RF discharge with alternating phase (b) for L = 55 mm, V_{pp} = 100 V at pressure p = 1,8 Pa

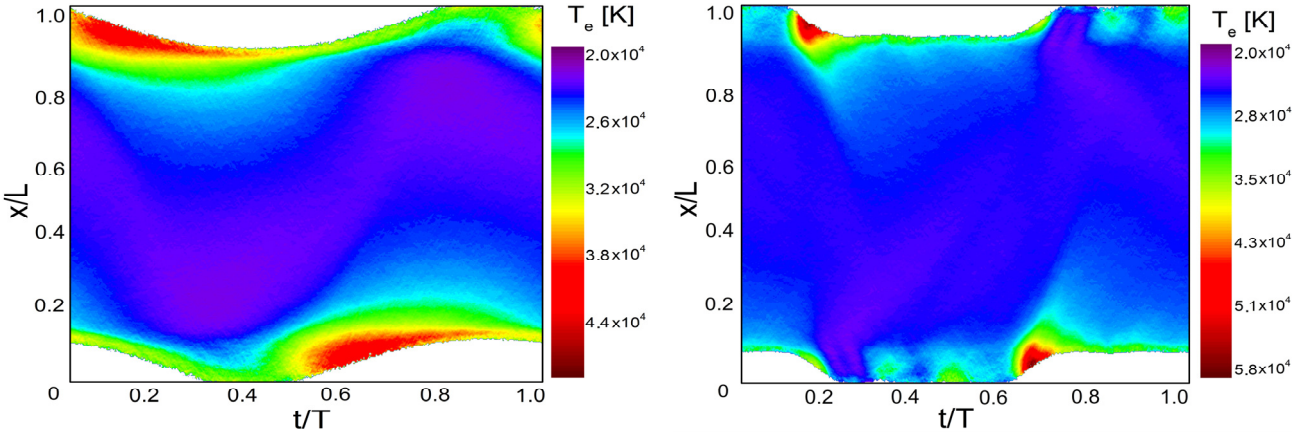

Figure 4 – Spatiotemporal profile of electron temperature in RF discharge (a) and RF discharge with alternating phase (b) for L = 55 mm, V_{pp} = 100 V at pressure p = 1,8 Pa

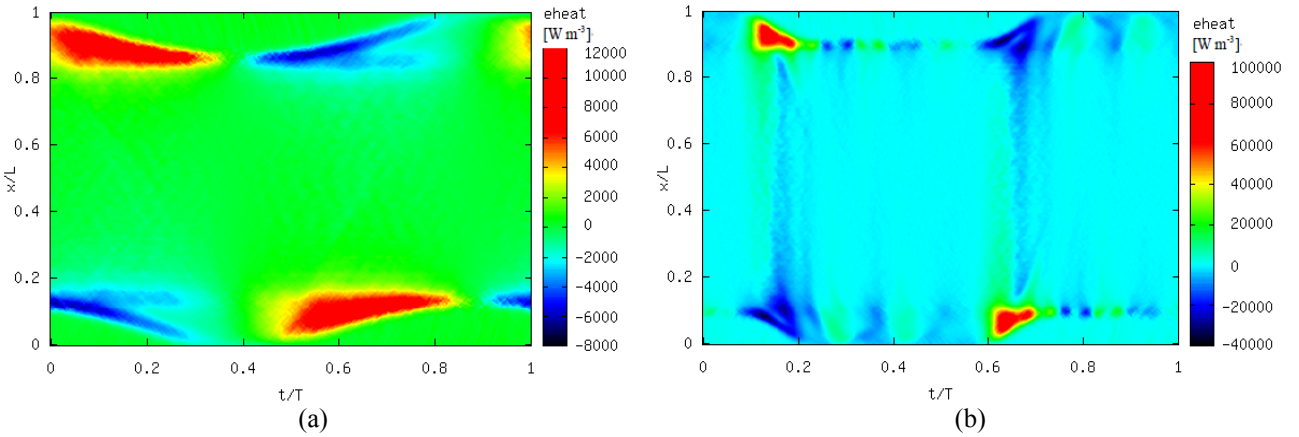

Figure 5 – Spatiotemporal profile of electron heating rate in RF discharge (a) and RF discharge with alternating phase (b) for L = 55 mm, V_{pp} = 100 V at pressure p = 1,8 Pa

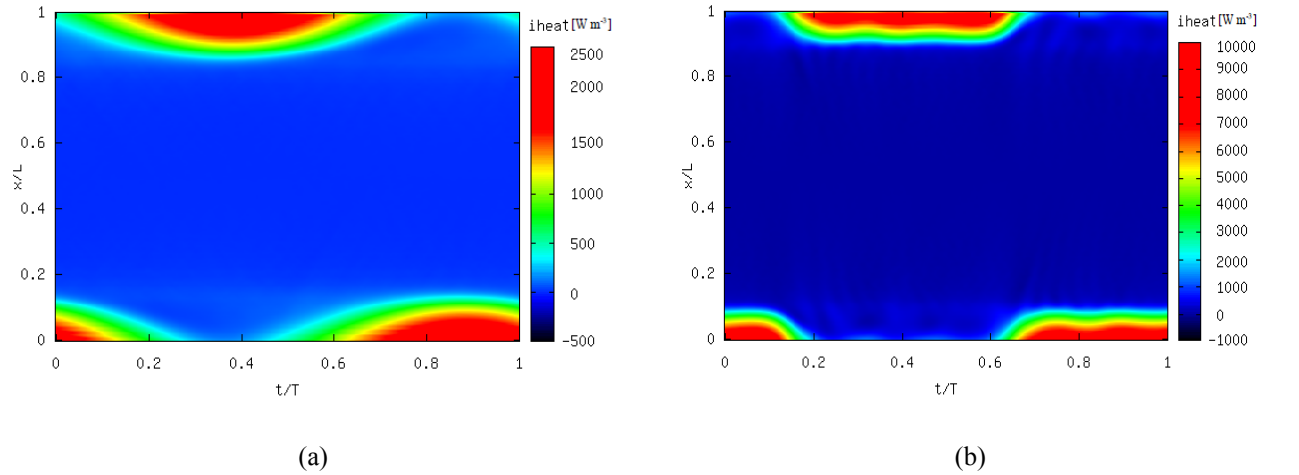

Figure 6 – Spatiotemporal profile of ion heating rate in RF discharge (a) and RF discharge with alternating phase (b) for L = 55 mm, V_{pp} = 100 V at pressure p = 1,8 Pa

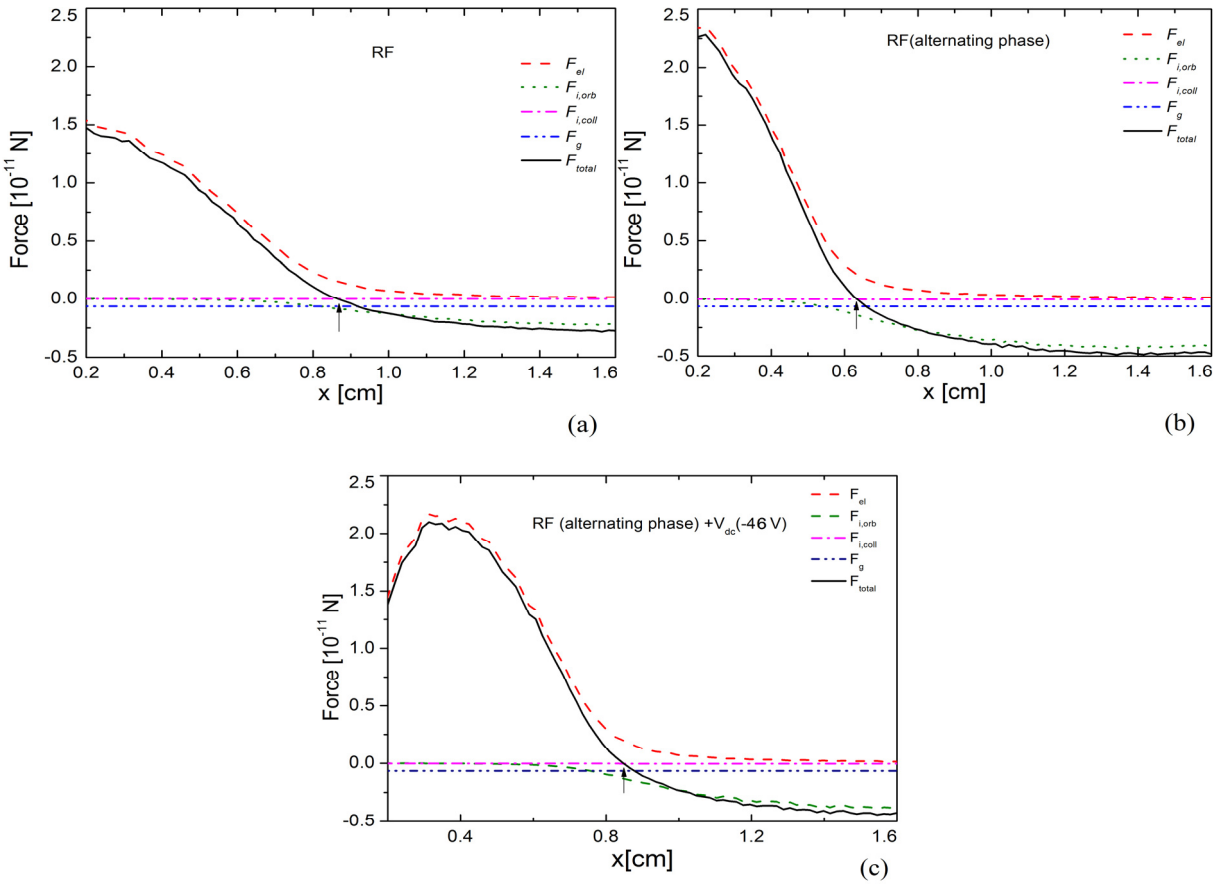

Figure 7 – Spatial dependence of the different force components in RF discharge (a) and RF discharge with alternating phase (b) and direct current (c), for conditions L = 55 mm, V_{pp} = 100 V at p = 1.8 Pa. The arrows indicate the equilibrium position of the dust particles for the corresponding conditions

Figures 7 (a)–(c) shows the individual force components and the resulting total force acting on the dust particles, for the three different excitation waveforms. A general observation is that the spatial position of the dust levitation x_d is largely defined by the spatial dependence of the electrostatic and ion orbit forces. For the harmonic RF excitation, x_d is found to be 0.84 cm. Following the changes of the sheath length and ion fluxes under the excitation with phase-alteration, x_d decreases to 0.61 cm. The negative bias voltage, which leads to a longer powered sheath, increases the position, to 0.81 cm, near to the original value found at the harmonic RF excitation waveform. These results demonstrate that the electron dynamics and the position of the dust particles can be controlled in nearly independent ways, by the change of the driving voltage waveform (including phase-modulation and using an additional dc bias). As the dust charging currents obviously change with the plasma density, which is in turn set by the waveform shape, different charging scenarios can be established at otherwise (nearly) the same levitation heights. The degrees of freedom provided by waveform tailoring and switching between different waveforms open a way to heat the dust particle suspension in a way similar to the second-order Fermi acceleration, which may induce a transition between the liquid and solid phases.

Conclusions

In this work the properties of complex plasma and the manipulation of plasma-dust layer in high-frequency discharge with an additional alternative phase are investigated. The computer simulation of the high-frequency capacitive discharge is carried out under the influence of an additional alternative phase on the basis of the particle-in-cell and Monte Carlo (PIC / MCC) methods. The charging

processes of dust particles, the forces acting on dust particles, as well as the equilibrium positions of the dust particles in the plasma are studied. A method for manipulating particles of micro and nano sizes in a low-temperature complex plasma has been developed. This method of manipulation of dust particles was tested at various plasma parameters (pressure, interelectrode distance, form of RF signal) of high-frequency discharge. The application of the RF excitation waveform with alternating phase was found to result in an increased electron temperature and plasma density and was revealed to have an effect of decreasing the dust levitation height. The additional dc bias, on the other hand, resulted in an increase of the levitation height and a moderate decrease of the plasma density. These two competing effects allow one to influence the dust charging mechanisms and screening length, while maintaining the levitation height, through which the energy balance of the dust system (similarly to Fermi acceleration) can be changed leading eventually to a phase transition.

References

1 Thomas H., Morfill G.E., Demmel V., Goree J., Feuerbacher B., Möhlmann D. "Plasma crystal: Coulomb crystallization in a dusty plasma." *Physical Review Letters* 73 (1994): 652.

2 Melzer A., Trottenberg T., Piel A. "Experimental determination of the charge on dust particles forming Coulomb lattices." *Physics Letters A* 191, no. 3-4 (1994): 301-308

3 Alexandrov A. L., Schweigert I. V., Peeters F. M. "A non-Maxwellian kinetic approach for charging of dust particles in discharge plasmas." *New Journal of Physics* 10 (2008): 093025.

4 Morfill G.E., Ivlev A.V. "Complex Plasmas: An Interdisciplinary Research Field." *Reviews of Modern Physics* 81, no. 4 (2009): 1353-1404.

5 Lieberman M.A., Lichtenberg A.J. *Principles of Plasma Discharges and Materials Processing.* 2nd ed. New York: John Wiley & Sons, 2005. – 46 p.

6 Makabe T., Petrović Z.Lj. *Plasma Electronics: Applications in Microelectronic Device Fabrication*. London: Taylor and Francis, 2006. – 124 p.

7 Bonitz M., Henning C. and Block D. "Complex plasmas: a laboratory for strong correlations." *Reports on Progress in Physics* 73, no. 6 (2010): 066501.

8 Fortov V. E., Ivlev A. V., Khrapak S. A., Khrapak A. G., and Morfill G. E. "Complex (dusty) plasmas: Current status, open issues, perspectives." *Physics reports* 421, no. 1-2 (2005): 1-103.

9 Thomas H., Morfill G.E., Demmel V., Goree J., Feuerbacher B., Möhlmann D. "Plasma crystal: Coulomb crystallization in a dusty plasma." *Physical Review Letters* 73 (1994): 652.

10 Iwashita S., Schungel E., Schulze J., Hartmann P., Donko Z., Uchida G., Koga K., Shiratani M., Czarnetzki U. "Transport control of dust particles via the electrical asymmetry effect: Experiment simulation and modelling." *J. Phys. D: Appl. Phys*. 46, no. 24 (2013): 245202.

11 Park G.Y., Park S.J., Choi I.G., Koo I.G., Byun J.H., Hong J.W., Sim J.Y., Collins G.J. and Lee J.K. "Atmospheric-pressure Plasma Sources for Biomedical Applications." *Plasma Sources Sci. Technol*. 21, no. 4 (2012): 043001.

12 Hemke T., Wollny A., Gebhardt M., Brinkmann R.P. and Mussenbrock T. "Spatially resolved simulation of a radio-frequency driven micro-atmospheric pressure plasma jet and its effluent." *J. Phys. D: Appl. Phys*. 44 (2011): 285206.

13 Kawamura E., Lichtenberg A.J. and Lieberman M.A. "Secondary electrons in rf and dc/rf capacitive discharges." *Plasma Sources Sci. Technol.* 17 (2008): 045002.

14 Klindworth M., Melzer A., Piel A., Schweigert V.A. "Laser-excited intershcll rotation of finite Coulomb dusters in a dusty plasma." *Phys. Rev. B*. 61 (2000): 8404-8410.

15 M. Bonitz, C. Henning, and D. "Block Complex plasmas: A laboratory for strong correlations." *Rep. Prog. Phys.* 73 (2010): 066501.

16 J. Schablinski, F.Wieben, and D. Block. "An optical tweezer for complex plasmas." *Phys. Plasmas*. 22 (2015): 043703.

17 Iwashita S., Schüngel, E., Schulze, J., Hartmann, P., Donkó, Z., Uchida, G., Koga K., Shiratani M., Czarnetzki, U. "Transport control of dust particles via the electrical asymmetry effect: Experiment, simulation and modelling." *Journal of Physics D: Applied Physics* 46, no. 24 (2013): 245202.

18 Birdsall C.K. and Langdon A.B. *Plasma Physics via Computer Simulation.* New York: McGraw-Hill, 1985. – 44-62 p.

19 Lieberman M.A., Booth J.P., Chabert P., Rax J.M. and Turner M.M. "Standing wave and skin effects in large-area, high-frequency capacitive

discharges." *Plasma Sources Sci. Technol.* 11 (2002): 283.

20 Chabert P. "Electromagnetic effects in high-frequency capacitive discharges used for plasma processing." *J. Phys. D: Appl. Phys* 40 (2007): R63.

21 Verboncoeur J.P. "Particle simulation of plasmas: review and advances." *Plasma Phys. Control. Fusion* 47 (2005): A231.

22 Matyash K., Schneider R., Taccogna F., Hatayama A., Longo S., Capitelli M., Tskhakaya D. and Bronold F.X. "Particle in Cell Simulation of Low Temperature Laboratory Plasmas." *Contrib. Plasma Phys*. 47 (2007): 595-634.

23 Phelps A.V. "The application of scattering cross sections to ion flux models in discharge sheaths." *J. Appl. Phys.* 76 (1994): 747.

24 Longo S. and Capitelli M. "A simple approach to treat anisotropic elastic collisions in Monte Carlo calculations of the electron energy distribution function in cold plasmas." *Plasma Chem. Plasma Proc*. 14 (1994): 1-13.

25 Biagi S.F. "Monte Carlo simulation of electron drift and diffusion in counting gases under the influence of electric and magnetic fields." *Nucl. Instrum. Methods Phys. Res. A.* 421 (1999): 234-240.

26 Turner M.M. "Kinetic properties of particle-in-cell simulations compromised by Monte Carlo collisions." *Phys. Plasmas*. 13 (2006): 033506.

27 Vahedi V., DiPeso G., Birdsall C.K., Lieberman M.A. and Rognlien T.D. "Capacitive RF discharges modelled by particle-in-cell Monte Carlo simulation. I. Analysis of numerical techniques." *Plasma Sources Sci. Technol.* 2 (1993): 261.

28 Nanbu K. "Probability Theory of Electron-Molecule, Ion-Molecule, Molecule-Molecule, and Coulomb Collisions for Particle Modeling of Materials Processing Plasmas and Gases." *IEEE Trans. Plasma Sci.* 28 (2000): 971-990.

29 Ding Li, Sudakov M. and Kumashiro S. "A Simulation study of the digital ion trap mass spectrometer." *Int. J. Mass. Spectrom.* 221 (2002): 117-139.

IRSTI 29.05.01; 27.43.51

[1]T. Sadykov, [2]F. Dankenova, [2]A.Zhumabayev,
[1,2]Y. Tautayev, [2]A. Tolenova, [2]B. Seifullina

[1]Institute of Physics and Technology, Almaty, Kazakhstan.
[2]al-Farabi Kazakh National University, Almaty, Kazakhstan.
[*]e-mail: tautaev@mail.ru

Investigation of radio emission from cosmic rays at an altitude 3340 m asl.

Abstract. The complex EAS installation of the Tien Shan mountain cosmic ray station which is situated at a height of 3340 m above sea level includes the scintillation and Cherenkov detectors of charged shower particles, an ionization calorimeter and a set of neutron detectors for registering the hadronic component of the shower, and a number of underground detectors of the penetrative EAS component. Now it is intended to expand this installation with a promising method for detecting the radio-emission generated by the particles of the developing shower. The facility for radio-emission detection consists of a three crossed dipole antennae, one being set vertically, and another two – mutually perpendicularly in a horizontal plane, all of them being connected to a three-channel radio-frequency amplifier of German production. By the passage of an extensive air shower, which is defined by a scintillation shower detector system, the output signal of antenna amplifier is digitized by a fast multichannel DT5720 ADC of Italian production, and kept within computer memory. The further analysis of the detected signal anticipates its operation according to a special algorithm and a search for the pulse of radio-emission from the shower. A functional test of the radio-installation is made with artificial signals which imitate those of the shower, and with the use of a N1996A type wave analyzer of Agilent Technologies production. We present preliminary results on the registration of extensive air shower emission at the Tien Shan installation which were collected during test measurements held in Summer 2016.
Key words: radio emission, cosmic rays, trigger, extensive air shower, background.

Introduction

The registration of radio-emission generated by particles of high-energy extensive air showers (EAS) has a number of advantages over other methods of primary cosmic ray investigation, both of which are based on direct registration of shower particles (a relative simple and cheap radio-detector system compared with wide-spread electronic detector systems, the large spatial volume of the space controlled by a single radio antenna, a sensitivity to the characteristics of longitudinal EAS development), and the methods connected with the registration of Cherenkov and fluorescent EAS emissions in ultraviolet and optic diapasons (an unrestricted duty cycle of radio installation which is independent of daytime and weather conditions). Because of these reasons, it is quite natural that the first registration attempts of radio-frequency (RF) signal from EAS were only tried in the 1960 – 1970 decades. These works were based on the results of theoretical studies of the possible generation mechanism of radio-emission by shower particles: the coherent electromagnetic radiation of negative charge excess which is present in developing EAS [1], and the model of a moving electric dipole which should arise because of the separation of the differently charged shower particles in a geomagnetic field [2]. As a result of these early investigations, the EAS signals were indeed found in the frequency range of 30-100 MHz, but the researchers met a number of difficulties in the interpretation of the registered signals which were connected with both insufficient qualities of those days' electronics and a bad reproducibility of the results because of electromagnetic interferences and

weather conditions. A comprehensive review of previous studies on the detection of EAS radio signal can be found in [3].

The interest in the radio-method of EAS investigation reappeared in the early 2000s when the experiments CODALEMA (France) [4] and LOPES (Germany) [5] started their work. The availability of this method was proved by the simplicity and low cost of radio devices built using modern electronic modules and perspective application of contemporary information technologies for analyzing the registered data, as well as its effectiveness for the study of EAS events caused by ultra-high energy cosmic ray particles (10^{19} -10^{20} eV) whose statistics remains rather scarce up to the present time.

A convenient place for the development of the radio-method of EAS particle registration is the Tien Shan mountain cosmic ray station (43° 15` N, 76° 57` E, 3340 m above sea level) whose installations for the complex EAS investigation in the range of primary energies of 10^{14} – 10^{18} eV permit both a direct detection of the charged shower particles [6] at the station's level, and registration of Cherenkov light emitted above in atmosphere. Inclusion of a system for registering EAS electromagnetic radiation in the RF range into this complex gives a possibility of mutual calibration of all three EAS investigation methods, and permits to set accuracy limits on EAS parameters definition procedures based on their simultaneous employment. Later on, with the development of experimental techniques and enlargement of the detector system the study of EAS up to 10^{19} eV primary energy should be possible. This opens up the possibility of studying many yet unclear problems, such as the primary composition, anisotropy, sources of ultrahigh energy cosmic ray particles, specific features of their interaction with matter etc, which stay before the contemporary cosmic ray physics.

Experimental set-up

The wide-spread shower installation used for the registration of EAS charged particles at Tien Shan is built on the basis of plain polystyrene scintillators with 0.5 x 0.5 x 0.05 m^3 size. For collection homogeneity of scintillation light, the scintillators are placed within a pyramid-shaped light reflector casing and viewed by photomultiplier tubes (PMT) of types FEU49, FEU84, FEU115. A pair of electric pulse signals taken from the PMT anode with different electronic amplification (a ~ 30^x amplification high-sensitive signal, and a 1^x low-sensitive one) are transmitted in parallel and in analogue form to the data collection and acquisition center; simultaneous registration of the signals of two amplitude diapasons ensures the whole dynamic range about ~ (5-7) x 10^4 of scintillation amplitudes measured linearly and without noticeable saturation effects.

In the data acquisition center, the scintillation amplitudes which were present at the PMT outputs at the time of an EAS passage are digitized by a special multichannel amplitude-to-digital conversion (ADC) system which gives the momentary distribution profile of the density of charged shower particles over the installation plane. The ADC system of the Tien Shan station is built on the basis of 12-bit ADC chips of AD7888 type [7] and permits simultaneous digitizing of up to some thousands of analogue signals for the time that does not exceed 0.5 ms.

The central part of the shower detector system which operated together with the EAS radio-emission registration facility in Summer 2016 is a carpet of 72 scintillation detectors placed nearly equidistantly in the nodes of a net with 4 m x 3 m spatial step in the shape of an elongated rectangle with a total area of about 900 m^2. The EAS selection algorithm which was applied at that time ensures a 100% registration probability for showers with primary energy $E_0 > (5 – 7) \times 10^{14}$ eV whose axes pass through the central scintillation carpet; in every case of EAS registration a special control pulse signal, the shower trigger, was generated to synchronize any detector subsystems which were working simultaneously with the shower installation.

The positions of the detectors within the central part of the Tien Shan shower installation and the basic scintillation detectors are shown in figure 1. A detailed description of the whole detector complex and the data operation algorithms of the Tien Shan mountain station, as well as a report on the results of calibration measurements made there in 2014-2015, can be found in [6].

The zenith and azimuth angles of EAS arrivals are estimated by the mutual time delays between scintillation signals in two detector pairs placed symmetrically at opposite sides of the central carpet (these detectors are shown as black squares in figure 1). These delays are measured automatically for every registered EAS event using a 4-channel Tektronix TDS 2014 digital oscilloscope which operates with a 4 ns granularity for the time axis.

A shortcoming of the Tien Shan shower installation in its current state of Summer 2016 was the absence of any operational detectors in its periphery. This limited the range of registered events with satisfactorily defined shower characteristics for only EAS whose axes came within the central scintillation carpet. To overcome this, additional scintillation detectors are now being installed at various points at distances of 20, 40, and 70 m from the carpet's center.

During the test measurements searching for EAS connected radio-signals at Tien Shan three radio-antennae sets placed along the northern side of scintillation carpet were used, as shown by A1-A3 in figure 1. Three dipole antennae were placed in each of these points; one of them being set vertically, and other two-mutually perpendicularly in the horizontal plane with their axes oriented in parallel to meridional and latitudinal directions (see the left panel of figure 2). The RF-signals from these antennae after detection in 3-channel receiver devices designed by Karlsruhe Institute of Technology and placed immediately at the antennae positions were transmitted through matched 50 Ω cable lines to the data collection center.

The frequency spectrum of background radio-emission accepted by the antennae system after its installation at the operation place (with no connection to any external trigger signal) is shown in the right panel of figure 2. According to the position of the spectrum density peaks it is seen that the considered antennae system is sensitive mostly in the 25-85 MHz frequency range. A high level of electromagnetic interference was also found to be temporarily present at these frequencies, in particular during the night time, which practically cancels any attempt of EAS signal registration by masking it between intensive high frequency noise. The problem of interference control must be one of the most important in the definitive design of the EAS radio system at Tien Shan.

A fast ADC system consisting of a pair of 4-channel CAEN DT5720 electronic modules of Italian production [8] was used to register the detected signal from radio-antennae set in the experiment.

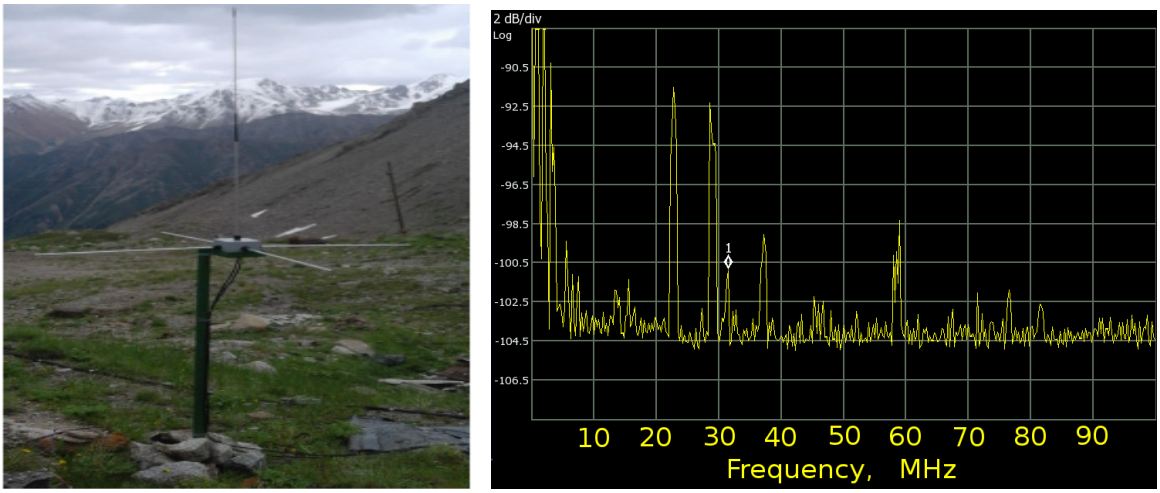

Figure 1 – Three dipole antennae set installed at point A1 at the Tien Shan mountain station (left), and the spectrum of background radio-emission measured with the Agilent Technologies N1996A wave analyzer (right)

This system ensures digitizing the analogue input signals with a 4 ns time resolution and keeps in its internal memory continuous records of the time history of the input signal stored for some tens of microseconds as a minimum. Presently, the outputs of all three antennae dipoles of the A1 point, and two horizontal dipoles of the point A2 are connected to these ADC modules.

Following the arrival of an EAS trigger signal generated by the scintillation shower system, the whole data set kept within the internal ADC memory is transmitted to a special program of the main control computer, and the latter in turn sends this information to the general Tien Shan database. Simultaneously, the spatial distribution of the EAS particle density measured with the central

scintillation carpet detector system are also loaded in the same database; these distributions can be used later for determining the parameters of the corresponding shower: the position of the shower core in the plane of the shower installation, zenith and azimuth directional angles of the shower axis, the parameters of shower age and size (the size has a physical meaning of the total number of particles in the shower. It is proportional to the primary energy of a cosmic ray particle, $E_{0,}$ which caused the event, and can be used, with some assumptions, for its immediate estimation).[9] All records in the Tien Shan database are supplied with a time stamp which marks the moment of EAS registration with an accuracy of 1 s (in the UT time zone); the clock of the local data registration system is verified continuously according to external Internet and GPS time servers.

Investigation of radio background on Tien-Shan high mountain scientific station

Measures of radio background carried out on scientific station, located at altitude 3340 meters above the sea level. On figure 2 has shown intensity of radio background in confines of frequencies between 10 and 100 MHz by the switched off antenna. For comparing, in the figure intensity of radio background on Tien-Shan station-1 and Almaty-2 is shown. It is seen that intensity of radio background in Almaty is higher than noise in mountains.

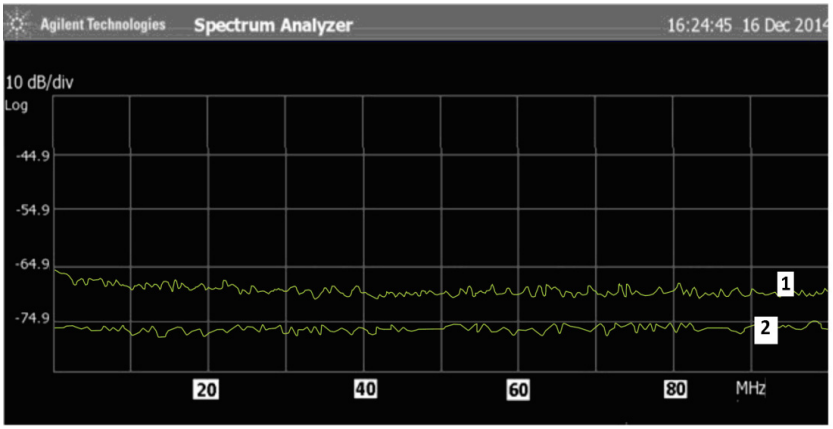

Figure 2 – Investigation of radio background by switched off antenna
a) at Tien-Shan high mountain scientific station at altitude 3340 meters above sea level,
b) in Almaty city

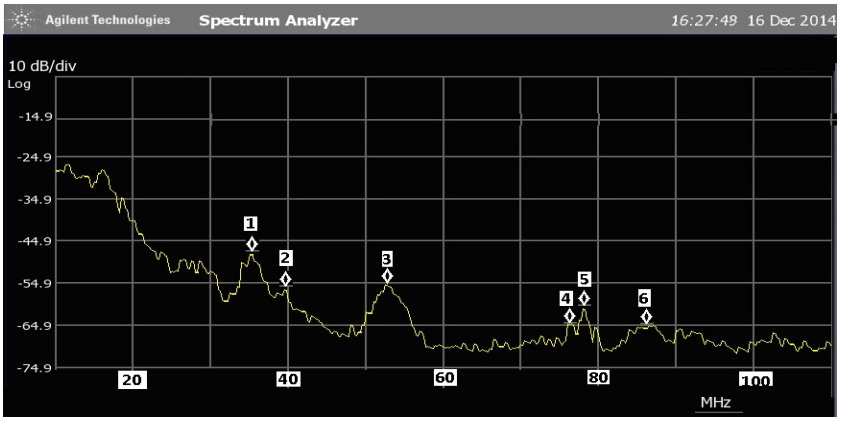

Figure 3 – Investigation of radio background by switched on antenna
at Tien-Shan high mountain scientific station

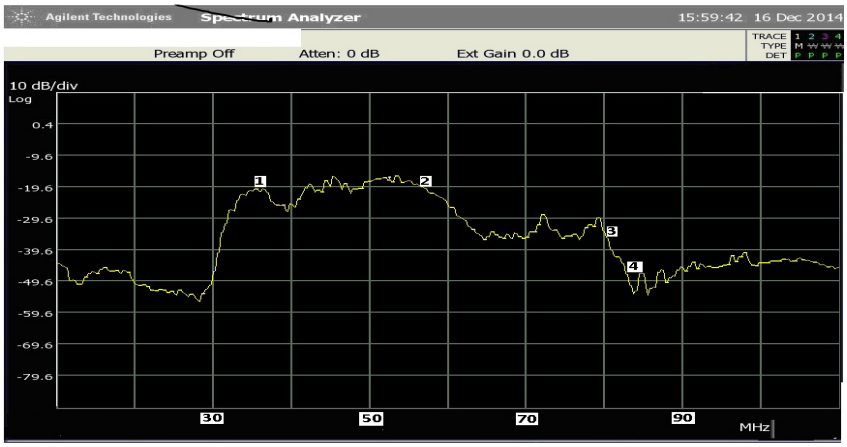

Figure 4 – Investigation of filter work on Tien- Shan high mountain scientific station.

Figure 3 presents intensity of radio background by switched on antenna. 4 frequency peaks of generation is registered between 40-80 MHz.

During the data processing we cut out all the noise. Figure 4 illustrates registration of radio frequencies with placing of filter. Filtration signals from the technical conditions in area of frequencies $33 \leq$ MHz ≥ 60 by the seize of intensity have to be stable. However, from the figure 8, it is seen that in area of frequencies $33 \leq$ MHz ≥ 60 average signal intensity is -19.6 dB/div, and in area of frequencies $60 \leq$ MHz ≥ 80 average signal intensity equal to 34.5 dB/div. It was noted, when radio antennas was established.[10]

Experimental results

The test experiment on the simultaneous registration of the data from the shower and radio systems of the Tien Shan station was held during four days in August 2016, the total life-time of the installation's operation was ~70 h. The purpose of this experiment was to clarify the real operational conditions for the registration of radio-signals at Tien Shan and to check the whole complex of hardware and software tools necessary for synchronous recording of the data from both detector system types. All records of radio-signal time series written in this period were looked over visually, and the signs of the presence of radio-emission signal above the usual fluctuation level in the ±10 μs vicinity of shower trigger moment were searched for in every registered radio-event. The total amount of examined radio-records is about ~30000, of which ~400 candidate events were selected which have an indication of a noticeable radio pulse shortly after EAS arrival time. Characteristic examples of such event type are presented in the plots of figure 3.

For each of the events in figure 3 the spatial 2D distribution of the density of EAS charged particles is shown in the plots of the left column, while the right column plots demonstrate the time distributions of detected radio-signal intensity obtained from three dipoles of antennae at point A1 (antennae signals at point A2 are quite similar to those shown in the figure). Every one of the shown distributions is registered with a 4 ns temporal resolution and consists of 10000 sequential measurements of signal intensity which correspond to the full duration of the measured time series of 40 μs. All distributions are centered relative to the arrival time of the EAS trigger which came from the scintillation shower system; hence, the leading 20 μs in every time series corresponds to the 'prehistory' of the radio-signal which precedes the EAS time, and the next 20 μs describe the time behaviour of the radio-signal after the passage of the shower front through the antennae system.

A noticeable radio-signal pulse with amplitude significantly above the mean level of stochastic fluctuations is present in all events of figure 3, and this pulse always arrives with a constant time delay of 1-3 μs duration relative to the trigger. At the same time, it is seen from the particle density distributions in the left column that the axis of corresponding shower has evidently come somewhat northward of the central scintillation carpet, i.e. at the side of the radio-antennae location, at least in the events of 09:35:43 UT and 18:28:09 UT. Such an asymmetric disposition of EAS core is typical for the greater part of the events selected by

the presence of a visible radio-signal just after the shower trigger, which is evidence that the observation of both signal types (i.e. an EAS and a radio-pulse delayed for a constant small time) in these events cannot simply be a random coincidence.

Because of the side location of EAS core in selected events relative to the central scintillation carpet and the absence of peripheral particle detectors in the operational state during the considered measurements run any strict determination of shower parameters in the presented events is impossible. If it is supposed that the shower axis of the 09:35:43 UT and 18:28:09 UT events is somewhere around the region of the radio-antennae sets, i.e. at a ~30-40 m distance from the center of the scintillation carpet, then according to the registered distributions of the particle density one can state that the primary EAS energy, E_0, in these events must be, correspondingly, at least $(2\text{-}3)\cdot 10^{16}$ eV and 10^{17} eV respectively (these estimations should be taken in the sense of lower limits). As for the 22:30:26 UT event, its maximum registered particle density of the order of 40000 particles/m^2 corresponds to a primary energy $E_0 > (3 – 5) \cdot 10^{17}$ eV. Considerable E_0 estimations which result, again, for the most part of the events selected by the presence of a radio-pulse in the vicinity of their shower front is another confirmation that this coincidence is non-random. Remembering that the threshold of the shower trigger during the measurements was about $E_0 > (5\text{-}7)\cdot 10^{14}$ eV, and the overwhelming part of registered shower events have, indeed, energies around 10^{14} -10^{15} eV (since the intensity of the primary cosmic ray flux decreases roughly with increasing energy), then the high E_0 values which result at once in all selected events cannot be fully accidental. It should also be noted that according to both modern experiments [4] and [5] the lower threshold of EAS radio-emission registration in 10-100 MHz diapason is of the order of $5\cdot 10^{16}$ eV which satisfactorily agrees with present estimations for E_0 in the events with a feasible radio-signal observation.

Besides the comparatively prominent radio-signal maximum within the closest 1 – 3 μs vicinity of EAS triggers frequently there is another secondary weak pulse which can often be seen in the time series of radio-intensity in selected candidate events, and usually follows the primary one at a fixed time of 5-7 μs after the trigger. Such a secondary pulse can be observed in the time distributions of figure 3, in particular in the 09:35:43 UT event. The characteristic 5-7 μs time delay of the secondary pulse corresponds to a linear distance of about 1.5 – 2 km, and this estimation, in its turn, to the distance to the nearest mountain slopes surrounding the Tien Shan station together with its antennae system sets. Hence, the secondary radio-pulse observed in time distributions of selected events can be interpreted as an echo signal resulting from the reflection of EAS radio-emission from the local relief details of Tien Shan station.

It is supposed that, in future, events with an appreciable EAS signal like the ones manually selected in the test experiment should serve as a prototype for the elaboration of an automatic recognition algorithm of the events with EAS radio-emission which is necessary for the final version of the corresponding software complex and any strict statistical investigations.

Conclusion

Setting up a radio-signal registration system mostly sensitive in the 25-85 MHz RF range is now in progress at the Tien Shan mountain cosmic ray station. This system is aimed for simultaneous operation with the EAS particle density and Cherenkov radiation detectors which are present at the station, and will permit a mutual calibration of all these independent methods of EAS investigation. Later on, with the use of an EAS radio-emission registration method, an enlargement of the energy range of primary cosmic ray investigation at Tien Shan up to $E_0 \sim 10^{19}$ is anticipated.

As a result of the preliminary test experiment, which was made using a newly installed dipole radio-antennae set, some candidate events were selected which demonstrate the presence of a noticeable radio-signal pulse in closest 1 – 3 μs vicinity of EAS arrival time. Specific features of particle density distribution in these events permit to state that most of them have a rather high primary energy $E_0 > (2 – 5) \cdot 10^{16}$ eV and a close location of their shower cores near to the radio-antennae set, so the time coincidence of the observed radio-pulse with the shower front arrival time in these events cannot be fully accidental. Hence, the radio-antennae system installed at Tien Shan together with a designed program complex for registration of its signal do indeed ensure an effective selection of radio-emission from EAS particles, and further work in this direction should be seriously considered.

References

1. Askaryan G.A. “Excess negative charge of an electron-photon shower and its coherent radio emission.” *Soviet Phys. J.E.T.P.* 14 (1962): 441-443.
2. Kahn F.D., Lerche I. “Radiation from cosmic ray air showers.” *Proceedings of the Royal Society of London. Series A. Mathematical and Physical Sciences* 289, no. 1417 (1966): 206-213.
3. Allan H.R. “Progress in Elementary Particle and Cosmic Ray Physics.” *North Holland Publ., Amsterdam,* (1971): 169.
4. Ardouin D., Belletoile A., Charrier D., Dallier R., Denis L., Eschstruth P., Gousset T., Haddad F., Lamblin J., Lautridou P., Lecacheux A., Monnier-Ragaigne D., Rahmani A., Ravel O. “Radio-detection signature of high-energy cosmic rays by the CODALEMA experiment.” *Nucl. Instrum. Methods A* 555, no. 1-2 (December 2005): 148-163.
5. Nigl A., Apel W.D., Arteaga T., Asch J.C., Auffenberg J., Badea F., Bähren L., Bekk K., Bertaina M., et al. “Frequency spectra of cosmic ray air shower radio emission measured with LOPES.” *Astronomy & Astrophysics* 488, no. 3 (December 2008): 807-817.
6. Arginova A.Kh., Loctionov A.A. et al. “The study of initial conditions in collisions of light, intermediate and heavy nuclei” Materials of 19-th International Symposium on Very High Energy Cosmic Ray Interactions, Moscow, Lebedev Physical Institute of RAN, *Eur.Phys.J.,* 2016.
7. “Analog Devices. 2.7 V to 5.25 V, micropower, 8-channel, 125 kSPS, 12-bit ADC in 16-lead TSSOP AD7888 Datasheet” http://www.analog.com, 2015.
8. “CAEN. Mod. DT5720 4 channel 12 bit 250 MS/s Digitizer Manual” *Rev.9.* http://www.caen.it/servlet/checkCaenManualFile Id=10257/, 2014.
9. Allan H. R. “Radio Emission From Extensive Air Showers.” *Progress in Elementary Particle and Cosmic Ray Physics* 10 (1971): 171–302.
10. Grebe S., Collaboration P.A. “Spectral index analysis of the data from the Auger Engineering Radio Array.” *AIP Conference Proceedings* 1535, no. 1 (2013): 73–77.

IRSTI 29.01.45

Z.Zh. Zhanabaev, Y.T. Kozhagulov, S.A. Khokhlov,
*A.T. Agishev, D.M. Zhexebay

Al-Farabi Kazakh National University, Almaty, Kazakhstan
*e-mail: Aldiyar.agishev@gmail.com

Informational and entropic criteria of self-similarity of fractals and chaotic signals

Abstract. Information entropy and fractal dimension of a set of physical values are usually used us quantitative characteristic of chaos. Normalization of entropy is a well-known problem. This work is devoted to develop a method to do this. In the work proposed criteria for self-similarity of information and informational entropy. We have defined normalized values of information (I_1 = 0.567) and informational entropy (I_2 = 0.806) as fixed points of probability density function of information and informational entropy. Meaning of these values is described as criteria of self-similarity of fractals and chaotic signals with different dimensions. We have shown that self-similarity occurs if normalized informational entropy S belongs to the ranges $[0,I_1)$, $[I_1,I_2)$, $[I_2,1)$, that corresponds to topological dimensions from 1 to 3 of quasi-periodic, chaotic, stochastic objects. Validity of these findings has been confirmed by calculation of entropy for hierarchical sets of well-known fractals and nonlinear maps. These criteria can be applied to a wide range of problems, where entropy is used.
Key words: information; informational entropy; fractal; chaos; self-similarity.

Introduction

Rapid development of contemporary technologies leads to necessity of study of physical processes in nanocluster materials, laws typical for microwave chaotic signals, neural networks, etc. Scale invariance is the common property of such complex processes and objects. Taking into account this property we can neglect using of physical values with given dimension (for instance, dimension corresponding to length of an object). Local properties of scale invariance are self-similarity (similarity factor is equal on different variables) and self-affinity (similarity factors are different on different variables). Self-organization of matter and motion is also a common property of different processes and can be represented as transition from chaos to order in an open nonlinear and non-equilibrium systems. So, we shall consider invariant properties of such chaotic processes.

Generally, fractal dimension and informational entropy measured for physical processes are quantitative characteristics of chaos [1, 2]. Theoretical conclusions describing behavior of entropy in chaotic systems are known. According to the Prigozhin Theorem [3], the first derivative of informational entropy by time decreases to its minimum at self-organization in a system. In case energy of system is constant, total entropy of the system decreases according to the Klimontovich Theorem [4]. Results of study of entropy can be also applied for the description of processes of controlled self-organization [5].

Recent significant researches are devoted to problems of the theory of informational entropy and its applications. For example, baryon density perturbations are studied from the point of view of information theory in [6] by use of a logarithmic measure of information. In [7], information entropy is used to describe seismic vibrations. Cell entropy is normalized to entropy corresponding to radial oscillations. The paper [8] is devoted to the importance of choosing information measures for analyzing complex structures. It is noted that informational measures are simply inadequate for determining meaningful relationships among

 Printed in Kazakhstan

variables within joint probability distributions. Results of this works reflect a fundamental importance of choice a universal normalization of information entropy.

Method for accurate calculation of universally normalized entropy of a non-equilibrium system is not realized yet. The mentioned theorems do not provide answers the questions: what is the minimum value of entropy production, how entropy decreases at self-organization? Relation between entropy criterion of self-similarity and fractal dimension characterizing corresponding chaotic processes is not quite clear also. In [9], solution of such problems by normalizing the Shannon informational entropy to the Renyi entropy is suggested. However, order of the multifractal moment is determined from experiment. The purpose of this work is to search for answers to these questions without involving empirical constants.

Informational and entropic criteria of self-similarity

Concept of information is often used in such branches of science as cybernetics, genetics, sociology, etc. As usual, considered systems are open systems. Development of methods used for the description of such systems stimulates the necessity for generalization of concept of information. As usual, open systems are considered as systems exchanging with external environment by energy, matter and information.

Actually, a complex object is characterized by its main properties. Information $I(x)$ for statistical realization of a physical non-equilibrium value x is greater than zero. Let us designate probability of realization of x as $P(x)$. So, quantity of information can be expressed as

$$I(x) = -\ln P(x). \qquad (1)$$

Information is a value which can be used in different areas, but Eq. (1) corresponds with all of them.

By definition, mutual information transmitted through a communication channel with characteristic $x = x(t)$ is determined by difference between Shannon one-dimensional entropy and conditional entropy [10] as

$$I(x;y) = S(x) - S(x \mid y), \qquad (2)$$

where $y(t)$ is a characteristic of receiver. Unconditional Shannon entropy is defined as

$$S(x) = -\sum_{i=1}^{N} P(x_i) \ln P(x_i), \qquad (3)$$

where $P(x_i)$ is expectancy of hitting of variable x in the i^{th} cell with relative size δ. Conditional entropy $S(x|y)$ can be written as

$$S(x/y) = -\sum_{i=1}^{N}\sum_{j=1}^{M} P(x_i, y_j) \ln P(x_i \mid y_j), \qquad (4)$$

where $P(x_i|y_j)$ is conditional probability. Mutual information is nonzero only in presence of correlations between quantities $x(t)$, $y(t)$. For the description of dynamic systems, we can accept $y(t) = x'(t)$, i.e. the derivative of $x(t)$ is considered as a second variable.

Instead of one-dimensional Shannon entropy $S(x)$ we can use two-dimensional summarized entropy $S(x,y)$ and rewrite Eq. (2) as

$$I(x \mid y) = S(x,y) - S(x \mid y) > 0,$$

$$S(x,y) = -\sum_{i=1}^{N}\sum_{j=1}^{M} P(x_i, y_j) \ln P(x_i, y_j), \qquad (5)$$

where $P(x_i, y_i)$ is probability of hitting into cells with equal sides δ of phase space (x, y). We use the designation $I(x|y)$ to emphasize the role of conditions in definition of information, but not of correlations as in Eq. (2).

Using of $S(x,y)$ instead of $S(x)$ provides better condition for positivity of conditional information $I(x|y) > 0$, because $S(x,y) > S(x)$ always. In this meaning, Eq. (5) corresponds to greater noise immunity than Eq. (2). Normalizing of two-dimensional information and entropy to the value of summarized entropy, from Eq. (2) we have

$$\tilde{I}(x \mid y) + \tilde{S}(x \mid y) = 1,$$

$$\tilde{I}(x \mid y) = I(x \mid y) / S(x,y),$$

$$\tilde{S}(x \mid y) = S(x \mid y) / S(x,y). \qquad (6)$$

This is a convenient ratio for analysis of probabilistic processes written as a law of conservation of conditional information and entropy. It is from Eq. (4), (5) follows that informational entropy is the average value of information. Therefore, we shall use Eq. (2) as the basic definition of information.

According to Eq. (3) entropy calculated via probability density $f(x) = dP(x)/dx$ tends to infinity if x is a continuous value. For definition of scale-invariant regularities we must use a new approach at the description of informational phenomena. Because of this fact we can consider information as a defining independent variable. Information can be used for the description of statistical processes. So, we try to describe new properties of information with taking into account that information is a scale-invariance value.

Therefore, according to Eq. (1) probability of realization of information $P(I)$ can be described as

$$P(I) = e^{-I}. \tag{7}$$

Mathematical expression for probability $P(I)$ and probability density $f(I)$ can be written as

$$0 \le P(I) \le 1, \quad 0 \le I \le \infty;$$

$$\int_0^\infty f(I)dI = 1, \quad P(I) = \int_I^\infty f(I)dI. \tag{8}$$

From Eq. (7), (8) follows that $f(I) = P(I) = e^{-I}$. It means the equality of probability function $P(I)$ and probability density function of information $f(I)$. Information calculated via Eq. (1) is a scale-invariant value. So a law of distribution is the same for both whole object and its part. Informational entropy $S(I)$ of distribution of information is a mean value of information in an ensemble:

$$S(I) = \int_I^\infty If(I)dI = (1+I)e^{-I}. \tag{9}$$

Let us take into account that information can be normalized to unit. So, $1 \ge S \ge 0$ at $0 \le I \le \infty$. We obtained a finite value of entropy of a continuous set by introducing a measure. We accepted a probability density of information as a measure and as a result we get Eq. (9). This result is valid for information of any nature (social, cyber, genetic, etc.) and for different methods (mutual, conditional) for its determination.

We use information $I(f(I))$ and entropy $S(I)$ as characteristic functions. Fixed points of I ($f(I)$ and $S(I)$) can be described by the following mathematical expressions [11]:

$$I = f(I), \quad I = e^{-I}, \quad I = I_1 = 0.567, \tag{10}$$

$$S(I) = I, \quad (1+I)e^{-I} = I, \quad I = I_2 = 0.806. \tag{11}$$

I_2 is the minimum value of normalized multidimensional entropy achieved at transition to self-similarity. Normalized entropy of chaotic objects in a three-dimensional space (x,y,z) can be defined as

$$\widetilde{S}(x,y,z) = S(x,y,z)/(S(x)+S(y)+S(z)), \tag{12}$$

because its maximal value is equal to sum of entropies of components. Therefore,

$$I_2 \le \widetilde{S}(x,y,z) < 1. \tag{13}$$

I_1 is conveniently defined for conditional information of a geometric object as

$$I(y/x) = S(y,x) - S(y/x) = \\ = S(x) + S(y/x) - S(y/x) = S(x)'$$

$$I(x/y) = S(y). \tag{14}$$

Self-similar value of information (I_1) is the minimal value of normalized one-dimensional entropy of two-dimensional object:

$$I_1 \le \widetilde{S}(x) < I_2, \quad \widetilde{S}(x) = S(x)/S(x,y). \tag{15}$$

Transition to chaos and to statistical regularities in one-dimensional case is characterized by the range

$$0 < \widetilde{S}(\delta) < I_1, \quad \widetilde{S}(\delta) = S(\delta)/\ln(1/\delta), \tag{16}$$

where $S(\delta)$ is normalized entropy of Shannon segmentation by the relative scale of measurement δ. It is known from the theory of multifractals [12] that $S(\delta)$ is also an information dimension of a set containing a measure. Therefore, we can use I_1 and I_2 as boundaries for separation of fractional parts of dimensions characterizing self-similar sets with

topological dimensions $d = 1$ ($[0,I_1)$), $d = 2$ ($[I_1,I_2)$), $d= 3$ ($[I_2,1)$).

Results and Discussion

It is necessary to verify validity of criteria of self-similarity for information I_1 and entropy I_2 in natural phenomena. Fractal objects and processes are characterized by a universal property of scale invariance. However, the main characteristic of such objects which is fractal dimension cannot be unambiguously defined from experimental data, because results of application of different methods (cellular, inner, etc. dimensions) are noticeably different. Therefore, in the beginning, we shall use models of 17 geometric fractals with known dimensions from 1.26 to 2.0 [12,13].

All studied prefractals (hierarchical generations) with number of iterations equal to n contained the same number of points $N = 2^{18}$ and inscribed in squares with the same dimensions. Information entropy of a prefractal was determined via probabilities of appearing of points in square cells with relative scale $\delta = 10^{-3}$.

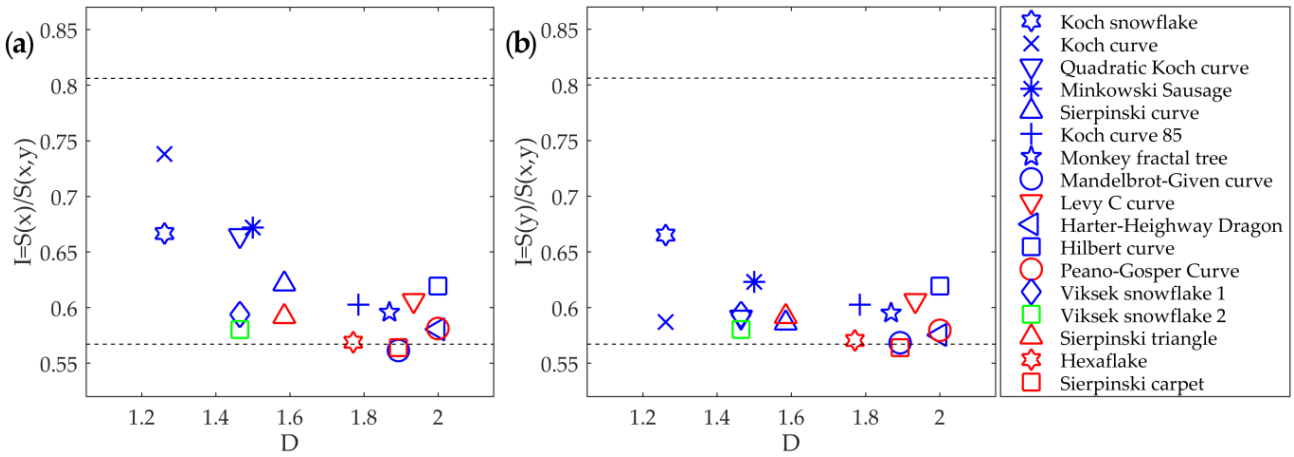

Figure 1 – Normalized information entropy (conditional information) $\widetilde{S}(x)$ (**a**) and $\widetilde{S}(y)$ (**b**) of fractals with dimensions D.

We have chosen $n = 6$, $\delta = 10^{-3}$ for all fractals for which the self-similar normalized values of entropy (12), (14), (15) can be considered independent on n, δ with an error less than one percent.

Figure 1 shows values of normalized information entropy of 17 fractals with indication of their abbreviated names corresponding to accepted in [12,13]. The normalized one-dimensional entropy (conditional information) for all fractals is less than I_2 and tends to the self-similar value I_1 with increasing dimension D_0. Choice of $S(x)$ or $S(y)$ corresponds to non-fractal ($n = 0$) length of x or y. Conditional information depends on two variables, so, the range $[I_1,I_2)$ corresponds to self-similarity of information.

To verify the existence of all self-similar entropy ranges (13), (15), (16), we use nonlinear maps with chaotic realizations. The one-dimensional logistic map and the two-dimensional Henon map are described by the Equations [14] as

$$y_{i+1} = ry_i(1 - y_i), \tag{17}$$

$$\begin{cases} x_{i+1} = 1 - ax_i^2 + y_i, \\ y_{i+1} = bx_i, \end{cases} \tag{18}$$

where r, a, b are parameters. Let us use a new three-dimensional mapping with parameters R, R_*,γ written as

$$\begin{cases} x_{i+1} = R\left(\left|1 - \dfrac{y_i}{R_*}\right|\right)^{-\gamma}, \\ y_{i+1} = R\left(\left|1 - \dfrac{z_i}{R_*}\right|\right)^{-\gamma}, \\ z_{i+1} = R\left(\left|1 - \dfrac{x_i}{R_*}\right|\right)^{-\gamma}. \end{cases} \quad (19)$$

Map (19) follows from requirement for nonlinearity of fractal measure with components x, y, z and $\gamma = D - d$, which is the difference between fractal and topological dimensions. Types of chaotic realizations of maps (17), (18) are known [14], therefore, Figure 2 shows only chaos of values of x, y, z according to system of Eq. (19).

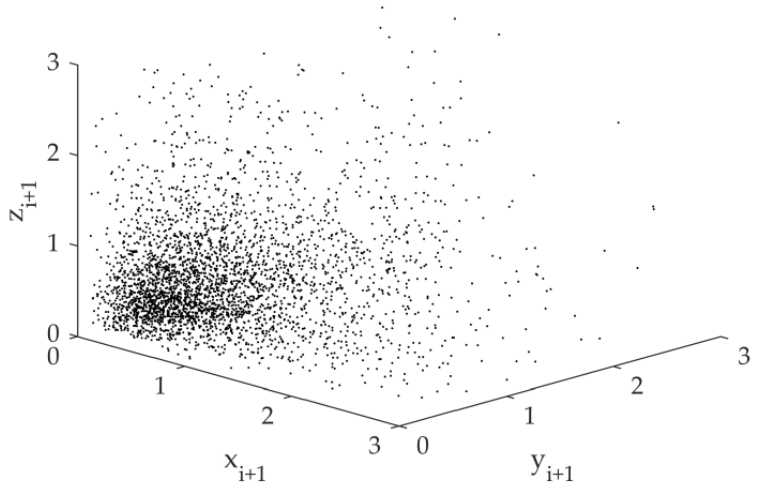

Figure 2 – Chaos of the three dimensional map (19) with parameters $R = 0.77$, $R_* = 1.1$, $\gamma = 0.2$ - 0.57, step equal to 10^{-2} and initial conditions are $x_1 = 1$, $y_1 = 1.1$, $z_1 = 0.9$. Number of samples is $N = 2^{18}$, number of iterations before attractor is $i_{max} = 10^3$.

Figure 3 presents normalized values of one-dimensional, two-dimensional, three-dimensional information entropies corresponding to Eq. (17), (18), (19). We have assumed the sum of variances of variables as a general order parameter leading to bifurcations:

$$\sigma^2 = \sum_{j=1}^{3} \sigma_j^2,$$

$$\sigma_j^2 = \left\langle x_j^2 \right\rangle - \left\langle x_j \right\rangle^2,$$

$$x_j = (x, y, z). \quad (20)$$

Depending on the map parameters, various signals can be referred as quasi-regular ($[0,I_1)$), chaotic ((I_1,I_2)), stochastic ($[I_2,1)$). Transitions between these modes are possible. This can be seen from the examples of bifurcation diagrams shown in Figure 4. Crowding of lines at small values of dispersion (transition to chaos) is more noticeable in three-dimensional case than in low-dimensional cases. Intermittency (alternation of order and chaos) is frequently observed in one-dimensional case than in two-dimensional and three-dimensional dynamical systems. Thus, Figures 1 and 3 clearly confirm validity of information criteria for self-similarity I_1, I_2.

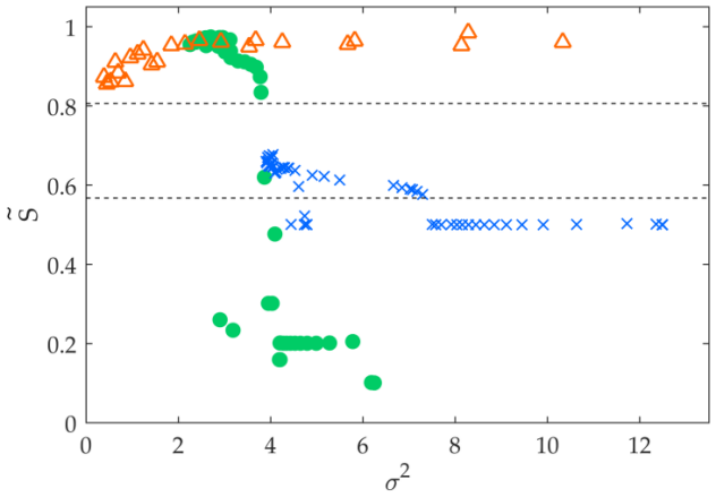

Figure 3 – Normalized information entropy of the maps (17) ● – $S(x)/\ln(1/\delta)$; (18) × – $S(x,y)/S((x)+S(y))$; (19) Δ – $S(x,y,z)/(S(x)+S(y)+S(z))$. Number of samples is $N = 2^{18}$, scale is $\delta = 10^{-3}$.

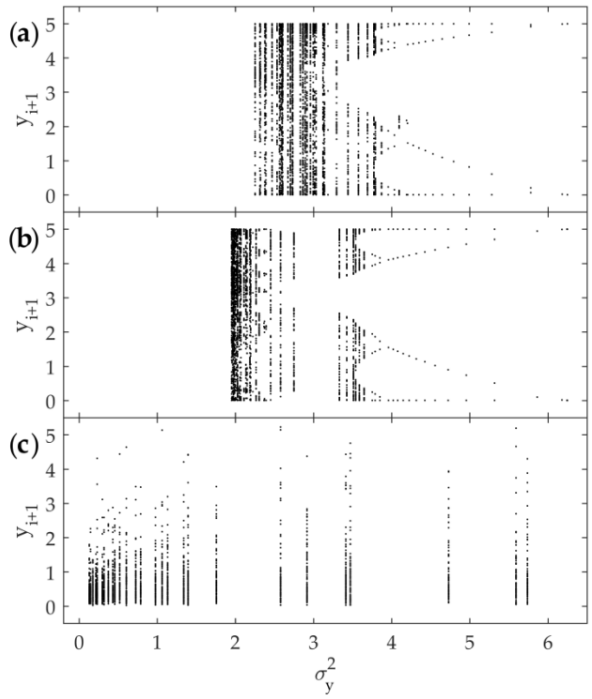

Figure 4 – Bifurcations diagrams of the maps.
(**a**) – (17), $r = 3.2$ - 4.0; (**b**) – (18), $b = 0.3$, $a = 0.5$ - 1.42; (**c**) – (19), $R = 0.77$, $R_* = 1.1$, $\gamma = 0.2$ - 0.57.
At all cases parameter step is 10^{-2}, initial value is $x_{y0} = 1$.
Total number of samples is $N = 2^{18}$, number of iterations before attractor is $i_{max} = 10^3$.

Conclusions

Informational and entropic criteria for self-similarity of fractals and chaotic signals can be applied to the quantitative analysis of phenomena with different nature. Information and entropy as measures of order and disorder have universal applicability both for natural and social phenomena. Attractors of dynamical systems, images of natural and nanotechnological objects can have a fractal structure. As usual, astrophysical, seismic, non-linear radio engineering, neural, nanoelectronic and other signals are chaotic signals. The entropic criteria established in the present work are associated with quasi-regular, chaotic, stochastic processes in considerably narrower ranges than in

case of applying other known characteristics of chaos, for example, in comparison with the unit interval of difference between fractal and topological dimensions.

Acknowledgments

This work was supported by the MES Republic of Kazakhstan [grant number ITT-2 «3084/GF4»].

References

1. Schroeder M.R. *Fractals, chaos, power laws: Minutes from an infinite paradise.* New York: Courier Corporation, 2009.

2. Grassberger P., Procaccia I. "Measuring the strangeness of strange attractors." In *The Theory of Chaotic Attractors,* New York: Springer, 2004. – 170-189 p.

3. Glansdorff P., Prigogine I. *Structure, stability and fluctuations.* New York: NY Interscience, 1971.

4. Klimontovich Y.L. "Information concerning the states of open systems." *Physica Scripta* 58 (1998): 549-555.

5. Prokopenko M., Gershenson C. "Entropy methods in guided self-organisation." *Entropy* 16 (2014): 5232-5241.

6. da Silva A.G., da Rocha R. "Information-entropic stability of Korteweg-de Vries solitons in the quark-gluon plasma." *Physics Letters B* 774 (2017): 98-102.

7. Bressan G., Barnaba C., Gentili S., Rossi G. "Information entropy of earthquake populations in northeastern Italy and western Slovenia." *Physics of the Earth and Planetary Interiors* 271 (2017): 29-46.

8. James R.G., Crutchfield J.P. "Multivariate dependence beyond Shannon information." *Entropy* 19 (2017): 531.

9. Zhanabaev Z.Zh., Kozhagulov Y.T., Khokhlov S.A. "Scale invariance criteria of dynamical chaos." *International Journal of Mathematics and Physics* 4 (2013): 29-37.

10. Nicolis J.S. *Dynamics of hierarchical systems: an evolutionary approach.* New York: Springer, 2012.

11. Zhanabaev Z.Zh. "Information properties of self-organizing systems." *Rep. Nat. Acad. Of Science RK* 5 (1996): 14-19.

12. Feder J. *Fractals*. New York: Springer, 2013.

13. Crownover R.M. *Introduction to fractals and chaos*. Boston: Jones & Bartlett Publishers, 1995.

14. Schuster H.G., Just W. *Deterministic chaos: an introduction*. 4th ed. New York: John Wiley & Sons, 2006.

IRSTI 44.35.31

*G. Kazakbay, D. Turalina

Faculty of Mechanics and Mathematics,
al-Farabi Kazakh National University, Almaty, Kazakhstan,
*e-mail: ggauharkb@gmail.com

Research with purpose of defining the lift and drag forces acting on hydro turbine blade with changing attack angle of flow

Abstract. In this paper the results of the research conducted to determine the effective version of hydro wheel blades of direct flow hydro turbine are presented. The aim of the research is to determine the optimal configurations of hydro turbine blades to improve the energy efficiency of the turbine. As a result of the study, a mathematical model of a hydro turbine was developed in the interactive COMSOL Multiphysics. Research was performed in the COMSOL Multiphysics application program with using Reynolds Averaged Navier Stokes method to Navier-Stokes equation for incompressible fluid. Direction of flow to blades with changing attack angle along blades was investigated. The change in velocity and pressure distribution of water through hydro turbine blades was considered. The optimal location of the blades was determined. Defined lift and drag forces acting along the blade. Based on the results of the research, it was determined the optimal configurations of the hydro wheel blades with high energy efficiency.
Key words. Hydro turbine, blade, COMSOL Multiphysics, lift force, drag force.

Introduction

Scientific research work is related to improving the energy efficiency of hydro turbine by changing the stream flow to hydro wheel. Hydropower plants use energy of water flow as the source of energy. Hydro turbine is the hydro engine that turn coming flow energy to mechanical energy.

Today, the whole world pays great attention to water flow energy as the effective source of energy. Investigated hydro turbine for small hydroelectric power station does not require a dam. Instead, it works in scheme as a part of the water given to head tube, after flowing through hydro turbine again dumped into the river. This direct flow hydro turbine size is small, so to construct it need less material accordingly it cost cheaper.

It is significant to correct choosing of the structure of the turbine, the size and location of the blades, the parameters of the guide vane, the head of water, the structure of the hydro wheels when installing a hydro turbine on a water stream to generating sufficient energy and effective working. Scientific research working is aimed to improving low head hydro turbine efficiency by changing the stream flow to hydro wheel. Research the optimal version of the attack angle of guide vane and hydro wheel blades with the purpose of improving efficiency of hydro turbine. Investigated low head hydro turbine can be used in the small and medium rivers of the Central Asian countries and Kazakhstan. This low head hydro turbine for small hydroelectric power station is for using for seasonal agriculture to farmers and for using in small settlements and remote villages [1, 2].

Computational experiment

The method of research is a numerical experiment. A theoretical study was carried out, a mathematical model of a hydro turbine blade was performed in the COMSOL Multiphysics application package. The COMSOL Multiphysics examines the distribution of velocity and pressure of water along the turbine blades [3]. Showed external construction of 3D model of hydro turbine in the interactive of COMSOL Multiphysics application package in Figure 1. Internal construction of the hydro turbine is showed in Figure 2.

 Printed in Kazakhstan

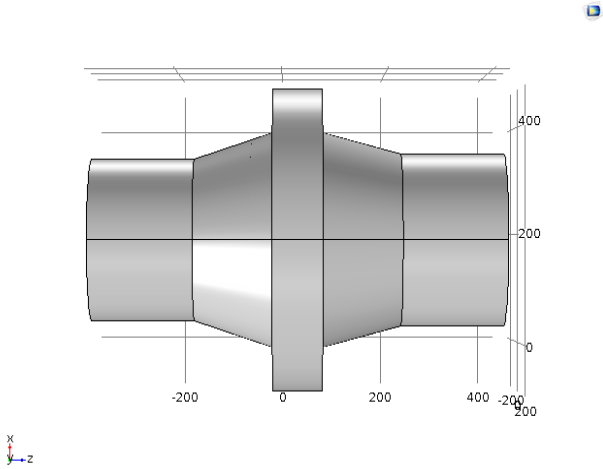

Figure 1 – Model of hydro turbine

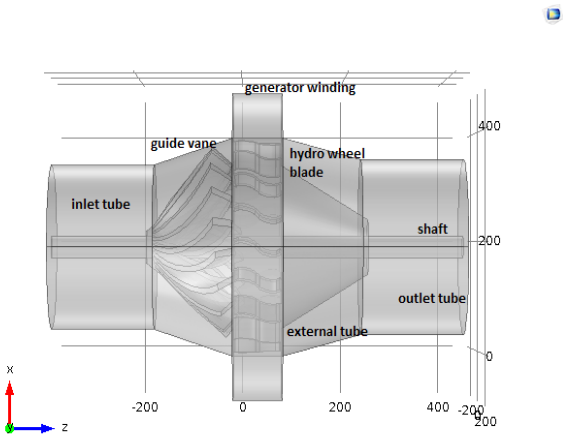

Figure 2 – Internal construction of the hydro turbine

Water enter through inlet tube, guide vane, rotating hydro wheel and pass through turbine then exit through outlet tube.

Guide vane and hydro wheel of the hydro turbine is showed in Figure 3. Front part as cone, blade located at as cylinder part.

To take as more energy is needed to turn as more the hydro wheel. Therefore, there is a guide vane with the aim to regulate impact and direction of water flow to the hydro wheel blades. When water flow through hydro turbine passing through guide vane and hit blades with pressure, and they rotate [4].

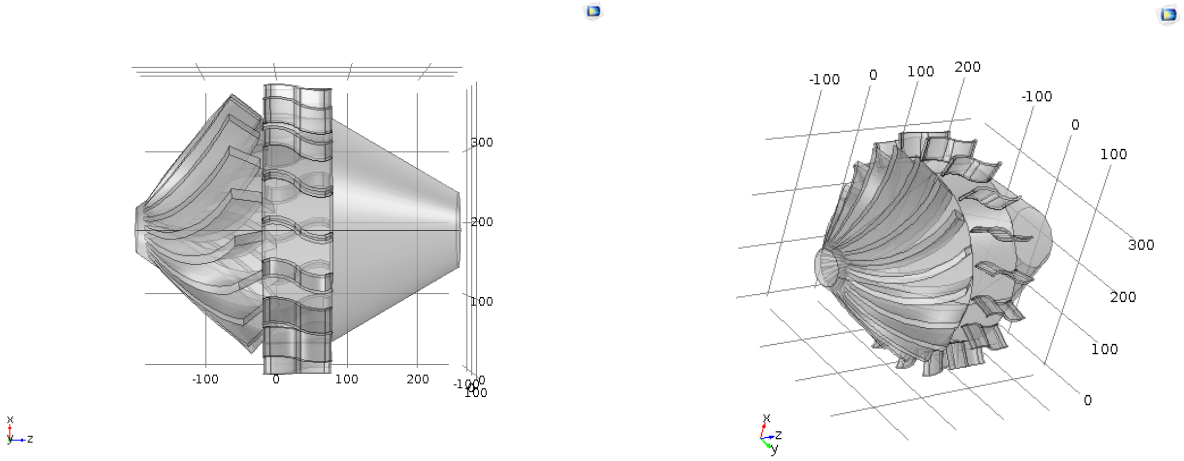

Figure 3 – Guide vane and hydro wheel

The energy efficiency of the hydro turbine is influenced by the number, shape, location, and attack angle of the guide vane and blades [5]. Therefore, the results of the research of the attack angle of the hydro wheel blades are presented. Attack angle is the angle between coming flow direction and chord line of the blade. Research was conducted with the purpose of improving the energy efficiency of hydro turbine.

Numerical calculation was performed by COMSOL Multiphysics application package. The results were obtained by changing the attack angle of blades of hydro wheel for shaping the two dimensions. Three different angles were obtained to show the improving in energy efficiency and to compare. Analyzed the distribution of velocity and pressure of water flow in COMSOL Multiphysics application package for 10 seconds, suggesting that the velocity at 1 m/sec [6].

Distribution of water flow velocity and pressure was calculated with using Reynolds Averaged Navier Stokes (RANS) method to Navier-Stokes equation for incompressible fluid.

For imcompressible fluid Navier-Stokes equations consists of motion and continuity equation [7]:

$$\rho\frac{\partial u}{\partial t}+\rho(u\cdot\nabla)u=\nabla\cdot[-pI+(\mu+\mu_T)(\nabla u+(\nabla u)^T)]+F \quad (1)$$
$$\rho\nabla\cdot(u)=0$$

Boundary conditions of the chosen blades in two dimension is showed in Figure 4.

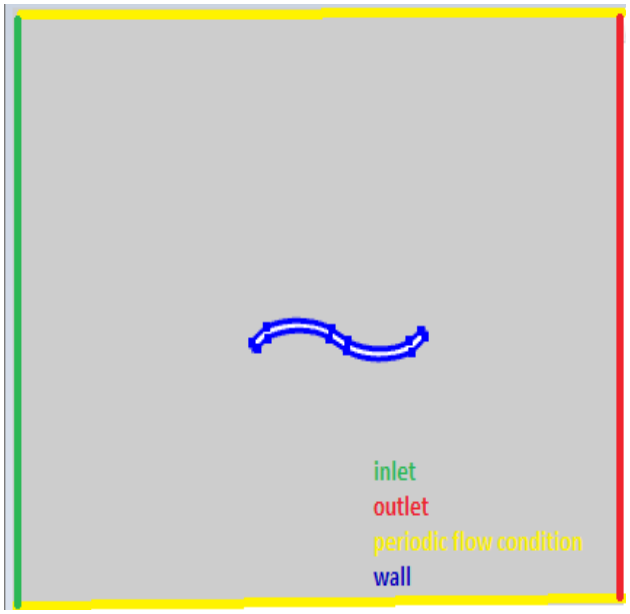

Figure 4 – Boundary conditions

Inlet:

$$U*\cos(\alpha*\pi/180),\ U*\sin(\alpha*\pi/180)$$

Outlet: Neumann boundary condition
Wall: No slip
Periodic flow condition:

$$u_{source}=u_{dest},\ p_{source}=p_{dest}$$

Periodic Flow Condition is used that take account that chosen blade is affected by the changes in the water velocity flowing along the under and upper blades.

Mesh allocation of model is showed in Figure 5.

Defining optimal attack angle of the blades

There are two ways to change the attack angle of the model. It is possible to turn the blade itself or to fixed blade but change the flow direction at the inlet. Second way is more simple to adjust the velocity field at the inlet boundary condition and there is no need to remesh the model for every attack angle.

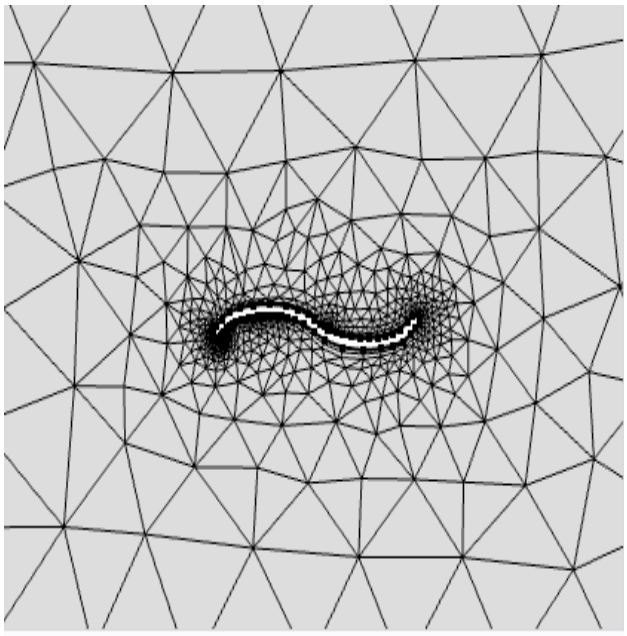

Figure 5 – Mesh allocation

Scheme of attack angle of the hydro wheel blade α illustrated in Figure 6.

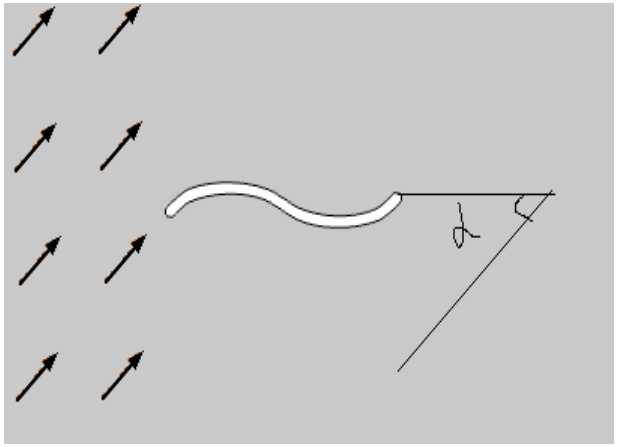

Figure 6 – Attack angle

Arrow is showed water flow direction. There α means attack angle. Attack angle is the angle between coming flow direction and chord line of the blade. The initial velocity of the water flow are determined as $U*\cos(\alpha*\pi/180)$ in x direction and as $U*\sin(\alpha*\pi/180)$ in y directon. Here $U=1$ m/s. Considered three various location of blades with changing attack angle. Values of attack angle α are 40°, 45°, 60°.

Results of velocity changing and pressure distribution along blade in 10 second, changing attack angle to 40º demonstrated in Figure 7.

Changing of colour from blue to red showed increasing of velocity and pressure. Arrow is showed water flow direction. In this case the maximum value of velocity reached to 1.32 m/s and pressure 565 Pa. Pressure increase in the bottom side of the blade as a result of the appearing lift force.

Results of velocity changing and pressure distribution along blade in 10 second, changing attack angle to 45º demonstrated in Figure 8.

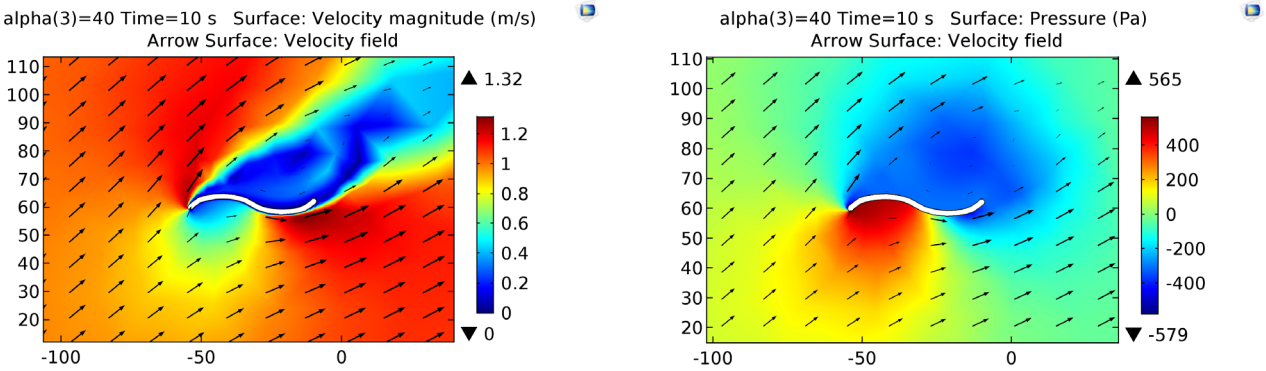

Figure 7 – Blade`s attack angle 40º

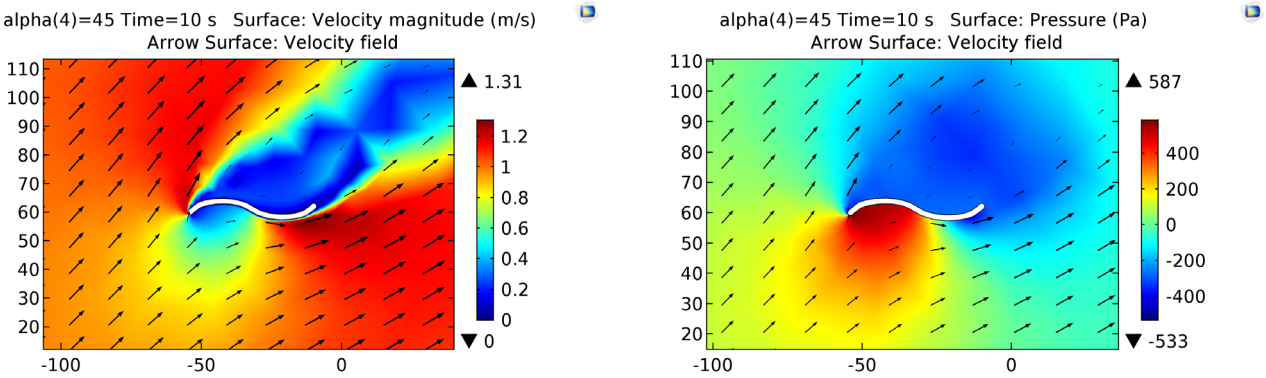

Figure 8 – Blade`s attack angle 45º

There maximum value of velocity reached to 1.31 m/s and maximum value of pressure reached 587 Pa. Comparing with previous results observed the much more efficiently. So we see that attack angle has affect.

Results of velocity changing and pressure distribution along blade in 10 second, changing attack angle to 60º demonstrated in Figure 9.

There maximum value of velocity reached to 1.26 m/s and pressure reached to 595 Pa. Changing attack angle affected to previous results.

Results of numerical experiment by COMSOL Multiphysics changing of velocity and pressure distribution of flow with changing attack angle of the blades are showed in Table 1.

Table 1 – Velocity and pressure changing with changing attack angle

Name	Attack angle of blades, °	Maximum value of velocity of flow, m/s	Maximum value of pressure of flow, Pa
1	40	1.32	565
2	45	1.31	587
3	60	1.26	595

In version when blade`s attack angle 40º maximum value of velocity is reached. Maximum value of pressure is reached when blade`s attack angle 60º.

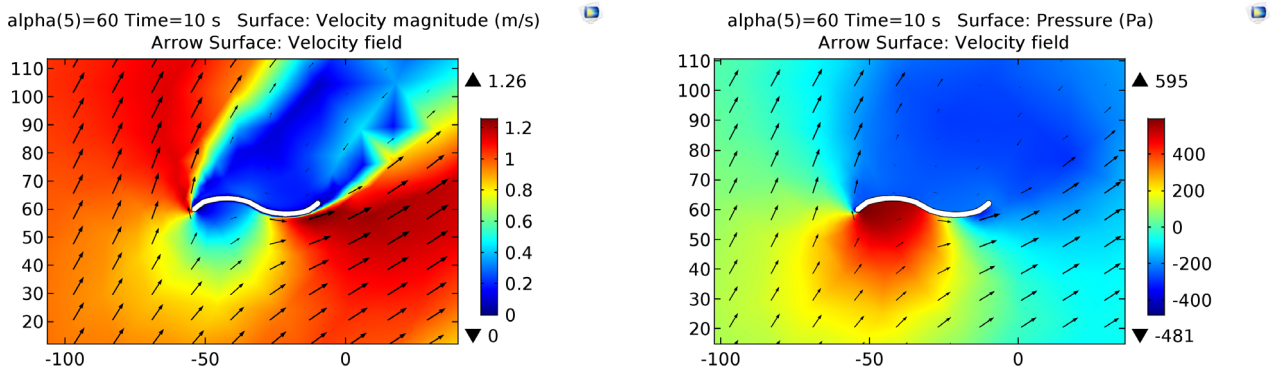

Figure 9 – Blade`s attack angle 60º

Defining lift and drag forces

When fluid flow passes a body, it exerts a force on the surface.The force component that perpendicular to the flow direction is called lift force F_L. The force component that parallel to the flow direction is called drag force F_D [8]. Scheme of the lift and drag forces acting on blade is illustrated in Figure 10.

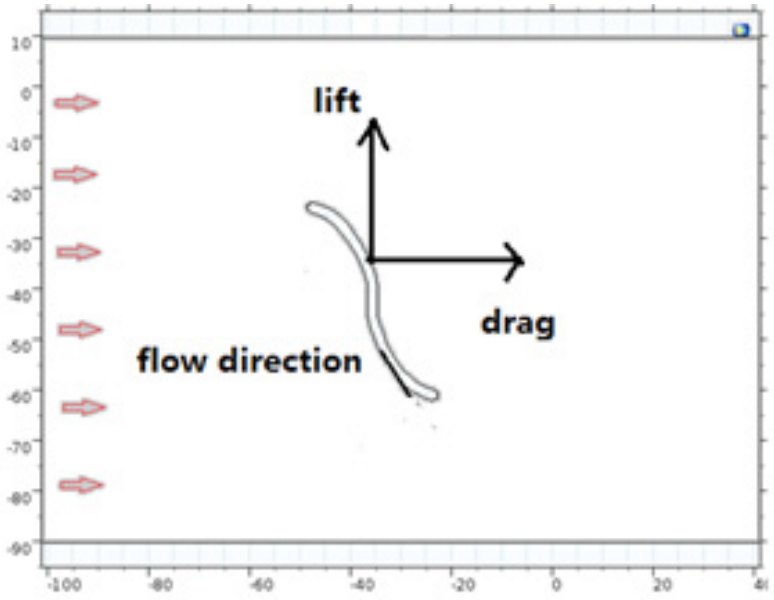

Figure 10 – Lift and drag force

There are two distinct contributors to lift and drag forces – pressure force and viscous force. The pressure force is the force appearing due to the pressure difference across the surface. The viscous force is the force deriving from friction that acts in the opposite direction of the flow [9].

Lift and drag forces at different angle attack of the blade at last time showed in Figure 11. Was chosen as various angle attack as 0º, 15º, 40º, 45º, 60º, 90º [10].

Last time is tenth second. Drag force increasing from 0 angle degree to 45 angle degree, then started to decreasing. Lift force increasing from 0 to 45 angle degree, then decreasing. So at 45 angle degree take maximum value of lift and drag force. At 60 angle degree take minimum value of drag force.

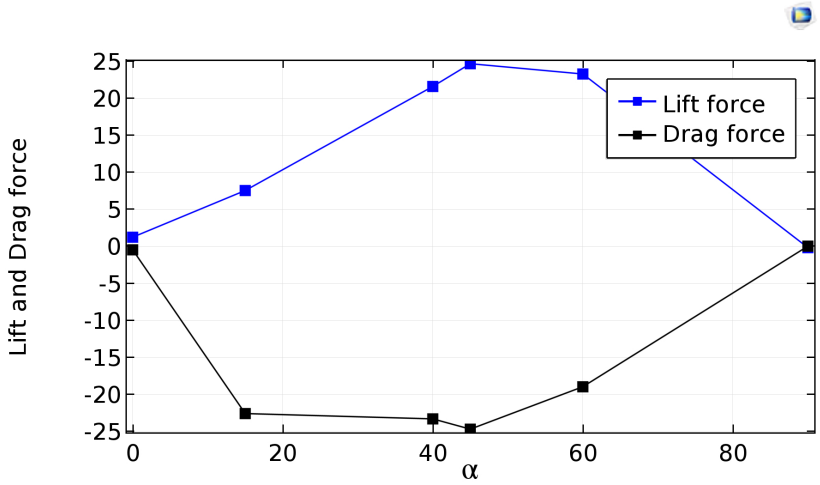

Figure 11 – Lift and drag force at last time

Conclusion

The effective version of hydro wheel blades of direct flow hydro turbine was determined. Research with the aim of improving efficiency of low head hydro turbine was performed. Three various location of the blades with changing attack angle investigated in the COMSOL Multiphysics application package. Based on the results of the research, it was determined the optimal configurations of the hydro wheel blades of the hydro turbine with effective efficiency. As optimal configuration was taken hydro wheel blade with attack angle 60º angle degree, where maximum value of velocity reached to 1.26 m/s and maximum value of pressure reached to 595 Pa. Defined lift and drag forces at different attack angle. Maximum value of lift force and minimum value of drag force defined at blade attack angle at 60 angle degree.

References

1. Koshumbayev M., Yerzhan A. "The innovative design of free-flow hydraulic turbine small hpp." *Materials of 2nd International conference on innovative trends in multidisplinary academic research*. Turkey. Istanbul, 2015.

2. Turalina D.E., Bossinov D.Zh. "Theoretical and experimental investigations to define optimal parameters of straight-flow turbine for non-dam hydro power station." *KazNU Bulletin (Mathematics, Mechanics, Computer Science Series)* 84 (2015): 124-131.

3. COMSOL Multiphysics User's Guide. 2012: P. 1292.

4. Stesina S.P. *Gidravlika, gidromashini i gidropnevmoprivod: ycheb. posobie dlya vyzov.* M.: Akademiya, 2007: 336 p.

5. Bashta T.M., Rydnev S.S., Nekrasov B.B. *Gidravlika, gidromashini i gidroprivodi: Ycheb. dlya vyzov.* M.: Alyans, 2010. 423 p.

6. Kazakbay G.B., Turalina D.E. "Research of the influence of lift force in accordance with the attack angle of water flow on the hydro wheel blades." *V International Farabi readings International scientific conference of students and young scientist*. Kazakhstan. Almaty, 2018.

7. Loytsyanskii L.G. *Mechanics of liquids and gases*. Oxford: Pergamon Press, 1966. 803 p.

8. Nakayama Y. *Introduction to Fluid Mechanics.* Oxford: Butterworth-Heinemann, 2000. 322 p.

9. Al-Shemmeri T.T. Engineering Fluid Mechanics // The ebook company: Bookboon. –2012. P. 147.

10. Lyu, Peter. "How Do I Compute Lift and Drag?" *COMSOL Blog*. http://www.comsol.com/blogs/how-do-i-compute-lift-and-drag.

CONTENTS